

DISSERTATION

UNDERSTANDING AND QUANTIFYING THE UNCERTAINTIES IN SATELLITE WARM  
RAIN RETRIEVALS

Submitted by

Richard Schulte

Department of Atmospheric Science

In partial fulfilment of the requirements

For the Degree of Doctor of Philosophy

Colorado State University

Fort Collins, Colorado

Spring 2022

Doctoral Committee:

Advisor: Christian D. Kummerow

Michael M. Bell

Sid Boukabara

Steven Reising

Peter Jan van Leeuwen

Copyright by Richard Schulte 2022

All Rights Reserved

## ABSTRACT

### UNDERSTANDING AND QUANTIFYING THE UNCERTAINTIES IN SATELLITE WARM RAIN RETRIEVALS

Satellite-based oceanic precipitation estimates, particularly those derived from the Global Precipitation Measurement (GPM) satellite and CloudSat, suffer from significant disagreement over regions of the globe where warm rain processes are dominant. Part of the uncertainty stems from differing assumptions about drop size distributions (DSDs). Satellite radar-based retrieval algorithms rely on DSD assumptions that may be overly simplistic, while radiometers further struggle to distinguish cloud water from rain. The aim of this study is to quantify uncertainties related to DSD assumptions in satellite precipitation retrievals, contextualize these uncertainties by comparing them to the uncertainty caused by other important factors like nonuniform beam filling, surface clutter, and vertical variability, and to see if GPM and CloudSat warm rainfall estimates can be partially reconciled if a consistent DSD model is assumed.

Surface disdrometer data are used to examine the impact of DSD variability on the ability of three satellite architectures to accurately estimate warm rainfall rates. Two architectures are similar to existing instrument combinations on the GPM Core Observatory and CloudSat, while the third is a theoretical triple frequency radar/radiometer architecture. An optimal estimation algorithm is developed to retrieve rain rates from synthetic satellite measurements, and it is found that the assumed DSD shape can have a large impact on retrieved rain rate, with biases on the order of 100% in some cases. To compare these uncertainties against the effects of horizontal and vertical inhomogeneity, satellite measurements are also simulated using output from a high-

resolution cloud resolving model. Finally, the optimal estimation algorithm is used to retrieve rain rates from near-coincident observations made by GPM and CloudSat. The algorithm retrieves more rain from the CloudSat observations than from the GPM observations, due in large part to GPM's insensitivity to light rain. However, the results also suggest an important role for DSD assumptions in explaining the discrepancy. When DSD assumptions are made consistent between the two retrievals, the gap in total accumulation between GPM and CloudSat is reduced by about 25%.

## ACKNOWLEDGEMENTS

I'd like to express my deep gratitude to my advisor, Dr. Kummerow, for guiding me through my Master's and Doctorate degree programs at CSU. You've given me the freedom and independence to make mistakes and grow into my own self as a scientist while also making sure I stayed on track for graduation and beyond. The whole Kummerow research group has been a great source of both scholastic and social support over these last 6 years and I'm so glad to call myself a member of the Kumraderie. Thanks also to my committee members for their time and support. Many scientists helped with the research presented in this dissertation, including Wes Berg, Brenda Dolan, Christian Klepp, Jay Mace, and Steve Saleeby. This work was supported by NASA FINESST grant 80NSSC19K1325.

To my wife, Allie, I cannot emphasize enough how much it has meant to me to have you by my side as I wrote my dissertation. I am so humbled by your willingness to move to Colorado and start a new life with me, and I'll always be grateful for the bravery you showed in Washington DC. To my family, thank you for all of the laughs, meals, breweries, vacations, and outdoor adventures we have shared. Especially once COVID hit, I felt incredibly lucky to have you all so close. And to all of my Fort Collins friends, especially the IM Squad, thank you for making the last six and a half years the happiest years of my life. I am so happy that I chose to attend CSU for graduate school.

## TABLE OF CONTENTS

ABSTRACT.....	ii
ACKNOWLEDGEMENTS.....	iv
1. CHAPTER 1: INTRODUCTION.....	1
1.1 Motivation.....	1
1.2 Limitations of satellite precipitation estimates .....	2
1.3 Outline .....	3
2. CHAPTER 2: HOW ACCURATELY CAN WARM RAIN REALISTICALLY BE RETRIEVED WITH SATELLITE SENSORS? PART I: DSD UNCERTAINTIES .....	5
2.1 Introduction.....	5
2.2 Data sources and models.....	9
2.2.1 OceanRAIN.....	9
2.2.2 ARM Eastern North Atlantic disdrometer data .....	11
2.2.3 Radiative transfer models .....	12
2.2.4 Ancillary assumptions.....	13
2.3 Methods.....	13
2.3.1 Simulation of satellite measurements .....	13
2.3.2 Optimal estimation retrieval algorithm.....	17
2.3.3 Error covariance matrices .....	19
2.4 Base case uncertainties .....	20
2.4.1 Uncertainties due to sensor noise, detection limits, and nonlinearities .....	20
2.4.2 Ancillary assumption uncertainties.....	23
2.5 DSD-related uncertainties.....	25
2.5.1 Experiments with binned DSDs.....	25
2.5.2 Impacts of assuming alternative DSD models.....	27
2.6 Conclusions.....	34
3. CHAPTER 3: HOW ACCURATELY CAN WARM RAIN REALISTICALLY BE RETRIEVED WITH SATELLITE SENSORS? PART 2: HORIZONTAL AND VERTICAL HETEROGENEITIES .....	37
3.1 Introduction.....	37
3.2 Data and methods.....	41
3.2.1 RAMS simulations.....	41
3.2.2 Simulation of satellite observations.....	43
3.2.3 Optimal estimation.....	44
3.3 Uncertainties due to nonuniform beam filling.....	47
3.3.1 Base case uncertainties .....	48
3.3.2 Effects of sensor footprint size .....	50
3.4 Uncertainties due to vertical variability.....	52
3.4.1 Assumptions about vertical structure.....	52
3.4.2 Vertical NUBF .....	54
3.5 Uncertainties due to surface clutter.....	55
3.6 Combined uncertainties for an AOS-like satellite .....	57

3.7 Discussion and conclusions .....	59
4. CHAPTER 4: CAN DSD ASSUMPTIONS EXPLAIN THE DIFFERENCES IN SATELLITE ESTIMATES OF WARM RAIN? .....	62
4.1 Introduction.....	62
4.2 Data.....	65
4.3 Methods.....	67
4.3.1 State and observation vectors.....	68
4.3.2 Forward model.....	70
4.3.3 DSD models.....	71
4.3.4 Covariance matrices.....	74
4.4 Results.....	76
4.4.1 Comparison between operational products.....	76
4.4.2 CloudSat-only and GPM-only retrievals .....	80
4.4.3 GPM retrievals with adjusted DSD assumptions.....	82
4.4.4 Combined retrievals.....	83
4.5 Discussion and Conclusions .....	86
5. CHAPTER 5: CONCLUSIONS .....	89
REFERENCES .....	93

## CHAPTER 1: INTRODUCTION

### 1.1 Motivation

Accurate global estimates of precipitation are crucial for properly understanding the Earth's water and energy cycles and how the hydrologic cycle might respond to energy imbalances in the future (Andrews et al. 2009; Stephens et al. 2012; Rodell et al. 2015). While ground-based radar and gauge networks can provide good estimates over densely populated land areas, satellite estimates are necessary over the oceans (Kidd et al. 2017). Satellite missions such as the Tropical Rainfall Measurement Mission (TRMM; Kummerow et al. 2000), the Global Precipitation Measurement (GPM) mission (Skofronick-Jackson et al. 2017), and CloudSat (Stephens et al. 2002) have greatly improved our understanding of the nature and distribution of global precipitation, but challenges remain. The uncertainty in the global mean oceanic precipitation rate is on the order of 10% (Stephens et al. 2012), but the uncertainty is larger in areas of the world where light, warm rain is common (Berg et al. 2010; Andersson et al. 2011; Behrangi and Song 2020). This is especially true over the high latitude oceans, as can be seen in Figure 1.1. This figure plots zonally averaged oceanic precipitation for one year of data from the GPM Ku-band Precipitation Radar (PR), the CloudSat W-band Cloud Profiling Radar (CPR), two reanalysis products (ERA-Interim and MERRA2), the Global Precipitation Climatology Project dataset (GPCP; Adler et al. 2003), and the Climate Prediction Center Merged Analysis of Precipitation (CMAP; Xie and Arkin 1997). Estimates from GPM are much lower over the Southern Ocean than the other estimates, and even among the other sources there are large disagreements.

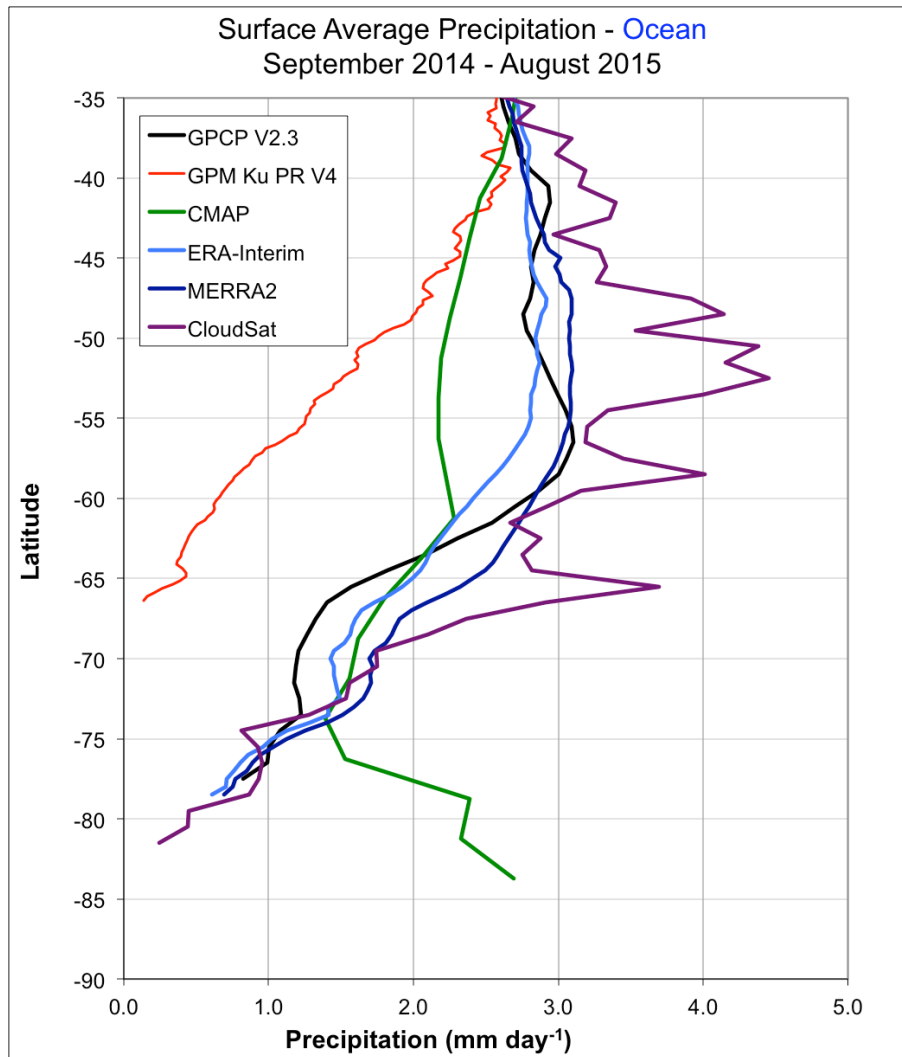


FIG. 1.1. Zonally-averaged mean oceanic surface precipitation rate for the period Sept. 2014 – Aug. 2015 for southern latitudes exceeding 35° South. Estimates come from the GPCP v2.3 satellite-gauge merged product (black), the GPM Ku precipitation radar (red), the CMAP merged product (green), the European Center for Medium-Range Weather Forecasts (ECMWF) ERA-Interim reanalysis product (light blue), the Modern-Era Retrospective analysis for Research and Applications v2 (MERRA-2; dark blue), and CloudSat (purple).

## 1.2 Limitations of Satellite Precipitation Estimates

There are a multitude of factors that contribute to satellite-based precipitation retrieval uncertainties, and thus play a role in the wide range of estimates seen in Figure 1.1. All atmospheric instruments have some measurement uncertainty, although this is far from the most important source of retrieval uncertainty when it comes to warm rain. Ground clutter effects can

cause spaceborne radars such as GPM's DPR and CloudSat's CPR to miss near-surface precipitation (Tanelli et al. 2008; Kidd et al. 2021), and GPM's reflectivity threshold means that it cannot detect precipitation with intensities less than about 0.2 mm/h (Hou et al. 2014). Meanwhile, passive microwave (PMW) based approaches struggle to distinguish cloud water from rain water (Elsaesser et al. 2017; Greenwald et al. 2018). Radiometers also offer little in the way of vertical information and tend to have coarser horizontal resolution than active sensors.

There are also several sources of uncertainty that are common to both active (i.e., radar) and PMW retrievals. Both active and passive measurements are affected by nonuniform beam filling (NUBF) (eg., Nakamura 1991; Graves 1993; Durden et al. 1998). In addition, retrieval algorithms must make assumptions about the rain drop size distribution (DSD) that can have large effects on retrieved rainfall rates (Lebsock and L'Ecuyer 2011; Liao et al. 2014; Protat et al. 2019b). Even dual frequency approaches struggle when drops are small and in the Rayleigh regime (e.g., Seto et al. 2021). DSD shapes are far from the only thing that must be assumed in a precipitation retrieval algorithm, which is a notoriously under-constrained problem (e.g., Stephens and Kummerow 2007). Assumptions must also be made about the vertical structure of hydrometeors, cloud droplets, atmospheric temperature and water vapor profiles, surface characteristics, and more.

### **1.3 Outline**

This dissertation represents an attempt to quantify the effect of the different sources of retrieval uncertainty listed above, and to investigate their competing effects on different types of satellite measurements. This is done with an eye towards reconciling the divergent estimates of warm rain rates from current satellites. Understanding which combinations of satellite

measurements are most susceptible to these uncertainties is also important in designing future satellite precipitation missions. The dissertation consists of three papers that are either submitted or in preparation. Chapter 2 has a specific focus on DSD-related uncertainties. Disdrometer data collected from ships around the globe as well as an island site in the Azores are used to investigate how DSD assumptions contribute to retrieval uncertainties for three different theoretical satellite architectures. Chapter 3 continues this examination but makes use of cloud resolving model data to consider other important sources of uncertainty such as NUBF, ground clutter, and assumptions about vertical structure. Finally, in Chapter 4 coincident observations from GPM and CloudSat are studied. Retrievals are performed on observations from both satellites using a consistent algorithm in order to test whether differences in rain rates from operational algorithms can be reconciled.

## CHAPTER 2: HOW ACCURATELY CAN WARM RAIN REALISTICALLY BE RETRIEVED WITH SATELLITE SENSORS? PART I: DSD UNCERTAINTIES

### 2.1 Introduction

Warm rain processes are an important part of the hydrologic cycle, especially over the oceans where aerosol concentrations tend to be low (Kubar et al. 2009). Observations from the CloudSat W-band satellite radar (Stephens et al. 2002) indicate that any given oceanic point may be beneath warm clouds between 10 and 50% of the time, with 20 to 40% of these clouds containing rain or drizzle at the lowest CloudSat range bin (Nuijens et al. 2017). The probability of precipitation is lower than this, due to evaporation below cloud base. For example, Yang et al. (2018) found drizzle in over 80% of marine stratocumulus cloud profiles at Graciosa Island, but precipitation reached the surface in only about 30% of the profiles. Nuijens et al. (2017) find that the greatest warm cloud fractions occur on the east side of the ocean basins as well as to a lesser extent over the Southern Ocean. Uncertainties in how the prevalence of low, warm clouds will change as the climate warms is one of the largest sources of uncertainty in global climate projections (e.g. Zelinka et al. 2020; Mülmenstädt et al. 2021), and several studies (Trenberth and Fasullo 2010; Bodas-Salcedo et al. 2014; Kay et al. 2016; Hyder et al. 2018) have noted that the Southern Ocean energy balance is poorly represented in global climate models. In this context, accurate present-day estimates of precipitation, cloud water, and cloud fraction from satellites are very important for evaluating and constraining weather and climate models.

While the overall uncertainty in the global mean precipitation rate is on the order of 10% (Haynes et al. 2009; Stephens et al. 2012), the uncertainty is even greater near the poles (Adler et al. 2003; Andersson et al. 2011; Behrangi et al. 2016). One factor that likely contributes is

uncertain and simplistic assumptions about drop size distributions (DSDs) for rainfall retrieval methods. Many radar-based precipitation retrieval algorithms assume a fixed DSD parameterization with only one free parameter (e.g. Haynes et al. 2009), or else merely choose between two sets of fixed parameters based on whether the precipitation is judged to be convective or stratiform (Lebsock and L'Ecuyer 2011; Duncan et al. 2018). The GPM combined algorithm is more flexible, with two free parameters, but still prescribes a constant shape parameter (Grecu et al. 2016). In reality, drop sizes do not conform to arbitrary categories but rather exist on a spectrum. Meanwhile, radiometers are much more sensitive to the total water mass in the atmospheric column than the size of the drops, so cloud/rain partitioning is a major challenge (Elsaesser et al. 2017; Greenwald et al. 2018).

Historically, the relationships prescribed in satellite precipitation algorithms have often been based on precipitation observations made over continents or in tropical locations. However, recent field campaigns have provided insightful observations at more diverse locations, including regions where warm rain processes are very important. The ObseRvations of Aerosols above Clouds and their intEractionS project (ORACLES; Redemann et al. 2021) involved many aircraft flights observing cloud structure and precipitation characteristics over the southeast Atlantic Ocean (Dzambo et al. 2019). Retrievals combining W-band radar reflectivities with polarimeter measurements were performed to jointly estimate cloud water path and rain water path, with cloud water path uncertainty on the order of 30% but with rain water path uncertainties frequently over 100% (Dzambo et al. 2021). The Cloud System and Evolution in the Trades campaign (CSET; Albrecht et al. 2019) included the deployment of a W-band airborne radar and a lidar to retrieve shallow cumulus cloud structures and precipitation. Sarkar et al. (2020) reported that rain drop distributions in CSET tended to shift towards larger drops sizes as the

boundary layer deepened, and Sarkar et al. (2021) found that cumulus rain rates retrieved from the combined radar/lidar observations tended to be lower than in-situ cloud probe measurements, in large part because the assumed raindrop size distribution was too narrow. In the Southern Ocean, a series of coordinated projects between 2016-2018 measured precipitation properties using in situ probes, radar, lidar, and other instruments (McFarquhar et al. 2021).

There has also been much work to validate and improve the DSD relationships assumed in satellite precipitation algorithms. The version 06A GPM precipitation algorithms are documented extensively in Seto et al. (2021). An important difference compared to earlier algorithm versions is the use of a DSD constraint that relates the rain rate to the mean drop diameter (R- $D_m$  relation). Liao et al. (2020) examined DSD data from several NASA field campaigns and arrived at a slightly different R- $D_m$  relation. They found that deviation from the R- $D_m$  relation was explained primarily by differences in the normalized intercept gamma parameter ( $N_w$ ). Shipboard observations from the Ocean Rainfall and Ice-phase Precipitation Measurement Network (OceanRAIN; Klepp et al. 2018) demonstrate significant latitudinal variability in oceanic rainfall properties, including the R- $D_m$  relation (Protat et al. 2019a).

Several studies have explored how DSD assumptions affect rain rates retrieved from ground-based radars (e.g. Lee and Zawadzki 2005, Adirosi et al. 2014, van de Beek et al. 2016). Fewer authors, however, have quantified the uncertainty in satellite precipitation products resulting from their assumptions about DSDs. Lebsock and L'Ecuyer (2011) showed that the assumption of a Marshall-Palmer DSD as opposed to a drizzle DSD increased the mean retrieved rain rate in the CloudSat 2C-RAIN-PROFILE algorithm by a factor of two, but tested no other DSD parameterizations. For the Global Precipitation Measurement Dual Precipitation Radar (GPM DPR), Liao et al. (2014) found that using a dual-wavelength technique is able to generally

keep estimates of retrieved rain rate within 10% of the true value, but only for rain rates greater than about 5 mm/h. More recent studies have reported mixed results. Protat et al. (2019b) speculate that high latitude rain rate retrievals from GPM could be significantly biased because of erroneous DSD assumptions, while Bringi et al. (2021) conclude that the current DSD assumptions “are not a major source of uncertainty” in the GPM combined algorithm.

Our study is distinct from earlier efforts in that it comprehensively and quantitatively estimates the impact of DSD assumptions in satellite precipitation retrieval algorithms. In addition, rather than focus on one particular instrument, we study how the DSD-related retrieval uncertainties change for different theoretical satellite architectures. This is important, as future satellite precipitation missions will have to make choices about what types of instruments to include. We construct simulated satellite observations based on surface disdrometer measurements and develop an optimal estimation retrieval algorithm to retrieve DSD parameters using various combinations of satellite measurements (Section 2.3). We then investigate how retrieval errors are affected by sensor uncertainties and detection limits (Section 2.4.1), ancillary assumptions about the atmospheric profile (Section 2.4.2), and the limitations of mathematical models to adequately capture the variability seen in real-world DSDs (Section 2.5). These experiments offer insight into which assumptions made in precipitation retrieval algorithms are most consequential, what types of observations are the most important for reducing uncertainty, and how future satellite missions could be constructed to reduce uncertainties in the estimation of warm rain.

## 2.2 Data Sources and Models

### 2.2.1 OceanRAIN

The OceanRAIN project seeks to mitigate some of the challenges historically faced by *in situ* measurements of oceanic precipitation with the use of high-quality ODM470 optical disdrometers (Grossklaus et al. 1998) placed onboard research vessels operating in remote areas. The disdrometers are manufactured by Eigenbrodt GmbH & Co. KG in Königsmoor, Germany, and measure precipitation occurrence, intensity, accumulation, phase, DSD, and ancillary meteorological data at 1-minute intervals. The ODM470 is able to quickly and automatically adjust to changing wind conditions to keep the measuring volume perpendicular to the instantaneous wind direction. A detailed description of the instrument can be found in Klepp (2015). Disdrometer calibration is performed before and after shipboard operations and comparisons against a reference rain gauge (ANS410) in light wind conditions yield accumulation differences on the order of 2% (Klepp 2015). The ODM470 has been used in several studies to evaluate satellite data and reanalysis products (Klepp et al. 2010; Bumke et al. 2016; Burdanowitz et al. 2018; Protat et al. 2019a).

We utilize OceanRAIN-M V1.0 data in this study. Raw drop counts from a 1-minute collection period are converted into number concentrations, and particles are grouped into 128 logarithmically-spaced bins ranging in size from 0.0375 mm to 22 mm. Bins 1-12 (up to 0.36 mm) are set to number concentrations of zero in the OceanRAIN-M V1.0 files because these bins can be contaminated by vibrations from the ship (Klepp et al., 2018). We found that a significant number of observations (20-70%) also had zero values in size bins 13-17 (up to 0.54 mm), suggesting that the data from these bins is not fully reliable. Thus, we disregard these bins as well and only rain drops 0.55 mm in size or larger are included. Drizzle drops can be much

smaller than this size (Wood 2005), which is why we also run experiments on data from a 2DVD disdrometer that is more sensitive to small drops (see Section 2.2.2). For calculating base-case uncertainties where DSD representation errors are disregarded, we assume that the DSD can be perfectly described by a 3-parameter normalized gamma (NG) distribution of the following form (Testud et al., 2001):

$$N_D = N_w f(\mu) \left(\frac{D}{D_m}\right)^\mu \exp\left[-(4 + \mu) \frac{D}{D_m}\right], \quad (2.1)$$

where

$$f(\mu) = \frac{6(4+\mu)^{4+\mu}}{4^4 \Gamma(4+\mu)}. \quad (2.2)$$

$N_D$  is the number concentration in  $\text{m}^{-3} \text{mm}^{-1}$  for drops of diameter  $D$ ,  $N_w$  is the normalized intercept parameter,  $\mu$  is the “shape parameter,”  $D_m$  is the mass spectrum mean diameter, and  $\Gamma()$  is the gamma function. The OceanRAIN-M V1.0 files contain values for  $D_m$ ,  $N_w$ , and  $\mu$  for each raining DSD. These parameters are fitted to the binned observations using the technique outlined in Testud et al. (2001) and Bringi et al. (2002). To calculate the rain rate from a given DSD, one must assume a relationship between drop size and fall speed. The OceanRAIN dataset does this according to the parameterization given by Atlas and Ulbrich (1974). For consistency, we use this same parameterization to calculate all rain rates considered in this study.

We use only observations marked as rain definite according to the OceanRAIN precipitation phase distinction algorithm (Burdanowitz et al. 2016), a regression method based on Koistinen and Saltikoff (1998) with the predictors of temperature, relative humidity, and 99<sup>th</sup> percentile of particle size distribution. We also screen to only include observations with 50 or more drops spread across at least 10 size bins. This results in a total of 69,677 raining minutes of data. Figure 2.1 shows the spatial distribution of the observations, indicating that many of the

observations occurred in previously under sampled areas including the Southern and Arctic Oceans.

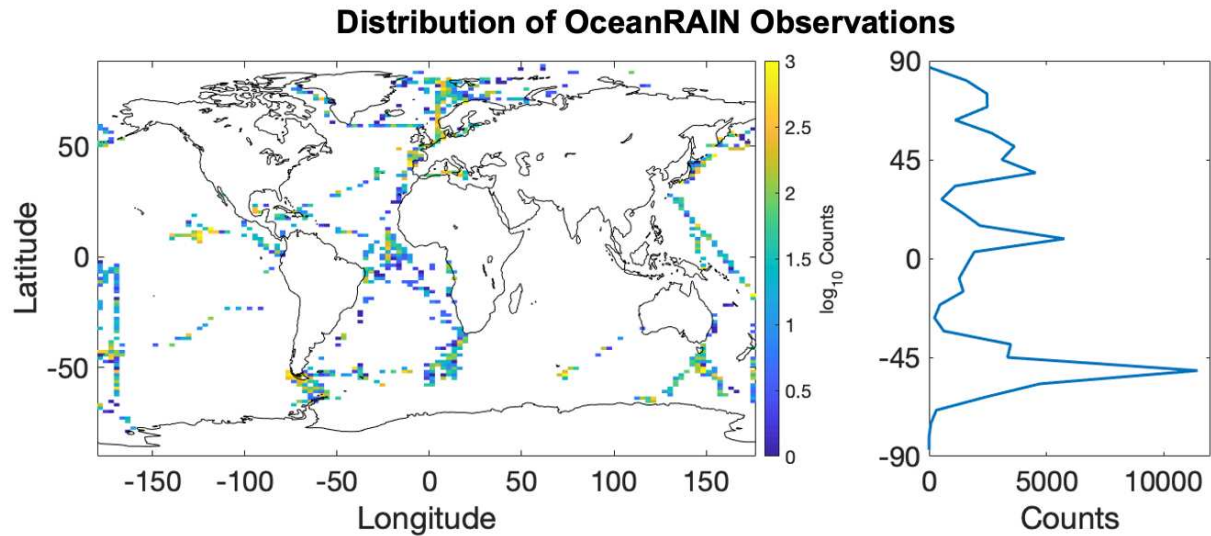


FIG. 2.1. Distribution of OceanRAIN DSD observations used in this study. On the left is the spatial distribution, gridded on a 3 degrees (longitude) by 1.5 degree (latitude) grid and colored according to the  $\log_{10}$  of the number of 1-minute observations within each grid box. On the right is a 1-dimensional histogram with observations summed across each latitude band in 6 degree increments.

### 2.2.2 ARM Eastern North Atlantic Disdrometer Data

Because of the unreliable OceanRAIN data for drops smaller than 0.55 mm, we also make use of DSDs observed at the Atmospheric Radiation Measurement (ARM) Eastern North Atlantic (ENA) atmospheric observatory located on Graciosa Island in the Azores. Because the ENA site is located far from continental landmasses, we expect the observed DSDs to be characteristic of the oceanic DSDs that are of interest to this study. In addition, this region of the world is characterized by marine stratocumulus clouds, which are significant producers of warm rain (Mülmenstädt et al. 2015; Nuijens et al. 2017; Nelson and L'Ecuyer 2018). We use 1 year (Jan. 1 – Dec. 31, 2019) of data from the 2-dimensional video disdrometer (2DVD) located at the site, covering drop sizes ranging from 0.1 mm to 10 mm in diameter (Bartholomew 2020).

Giangrande et al. (2019) examined data from the same site and found that the 2DVD was better than the collocated PARS disdrometer for measuring light rain. As with the OceanRAIN data, the DSDs are averaged over a 1-minute observation window and we only use rain definite observations with more than 50 individual drops measured.

### *2.2.3 Radiative Transfer Models*

In our experiments, we simulate passive microwave (PMW) brightness temperatures ( $T_B$ ), radar reflectivities ( $Z$ ), and radar two-way path-integrated attenuation (PIA). Simulated  $T_B$  are computed using the MonoRTM radiative transfer model (Clough et al., 2005) in combination with the FASTEM6 sea surface emissivity model (Kazumori and English, 2015). For calculating the absorption and scattering of upwelling microwave radiation due to hydrometeors, spherical cloud and rain drops are assumed and Mie theory (Mie 1908) is used. Simulated  $Z$  and PIA come from the QuickBeam radar simulator (Haynes et al., 2007). For simplicity, and because of our focus on light rain rates, multiple scattering is ignored. Another important source of error in satellite retrievals is partial beam filling (eg. Graves 1993). This potential source of retrieval bias is ignored in our experiments, but has been studied by several other authors (eg. Durden et al. 1998; Zhang et al. 2004; Hilburn and Wentz 2008; Tokay and Bashor 2010). An additional real-world complication that is not addressed in this study is radar surface clutter. GPM radar returns below about 1000-1500 m (depending on swath position) have too much noise to accurately detect precipitation (Kidd et al. 2021), while CloudSat is blind to precipitation below about 750 m above the surface (Tanelli et al. 2008). We have ignored these important sources of retrieval error in order to focus on DSD-related uncertainties. However, many of them will be addressed in Chapter 3 of this dissertation.

#### *2.2.4 Ancillary Assumptions*

It is necessary to make many assumptions about the atmospheric column when simulating observations from the various satellite architectures. The atmospheric profiles of temperature, water vapor, and pressure are interpolated from the US Standard Atmosphere (Minzner 1977). We nominally choose a wind speed of 10.0 m/s, a sea surface salinity of 35 parts per thousand, and a sea surface temperature (SST) of 285 K. Our experiments are not especially sensitive to the choice of these profiles and surface values (assuming that corresponding changes are made to the assumptions in the retrieval algorithm). In real life, surface wind speeds and profiles of temperature and water vapor can be obtained from nearby or even coincident satellite soundings. We chose to use the same atmospheric profiles for each disdrometer observation in order to simplify the experimental methods and data sourcing required. We do, however, estimate the impact that uncertainties in these ancillary assumptions will have on final retrieved rain rates (see Section 2.4.2). We do this by perturbing the variables of temperature, water vapor mixing ratio, SST, surface wind speed, and cloud droplet column-averaged effective radius when simulating satellite observations. In creating the perturbations we sample from a normal distribution centered at zero with a standard deviation of 1.0 K for temperature (including SST), 3.0 m/s for surface wind speed, 2.0  $\mu\text{m}$  for cloud droplet effective radius, and 10% of the US Standard Atmosphere value at each vertical level for water vapor mixing ratio.

### **2.3 Methods**

#### *2.3.1 Simulation of Satellite Measurements*

We consider 3 different theoretical satellite architectures in our experiments. The first (Satellite A) is similar to CloudSat, with a 94 GHz nadir-viewing radar that directly gives Z at

each range gate, and from which a PIA and a (noisy)  $T_B$  can be derived (Lebsock and Suzuki 2016; Mace et al. 2016). The second (Satellite B) is similar to the GPM core satellite, with a dual-frequency radar operating at 13.6 and 35.5 GHz (Ku and Ka-band, respectively) and a PMW radiometer operating at the same frequencies as the GPM Microwave Imager (GMI; Hou et al. 2014). We consider the radar and the radiometer to have the same footprint and to make simultaneous observations of the same spot, in order to compare the architectures on the basis of the information content that each type of measurement can provide, without introducing footprint differences. Finally, the third satellite, Satellite C, has a triple-frequency radar which combines the W-band frequency of Satellite A with the Ka and Ku-band frequencies of Satellite C. We assume that  $T_B$  can also be estimated at each of these frequencies at the same footprint of the radar, with reduced noise compared to Satellite A. We also assume a heightened detection sensitivity of the radar compared to Satellites A and B. Satellite C is meant to represent what might be possible with the next generation of precipitation satellites, such as that proposed by NASA's Aerosol, Cloud, Convection, and Precipitation (ACCP) study (NASEM 2018). See Tables 2.1 and 2.2 for a breakdown of the type of measurements simulated for each theoretical satellite architecture along with the assumed measurement uncertainties and sensitivities. For all radars, we assume a vertical resolution of 250 m, as this is the same vertical resolution obtained from GPM for matched Ku- and Ka-band footprints, and is very close to the Cloudsat vertical resolution of 240 m.

TABLE 2.1. Selected radar specifications for the 3 theoretical satellite architectures considered in this study. \*The reflectivity uncertainty is just a minimum value as the true value also depends on the difference between the measured Z and the Z threshold (T), the radar integration time (I), and the radar pulse repetition frequency (F; 4.3/ms for all 3 satellites). The equation for the

reflectivity uncertainty U is then given by  $U = \sqrt{N^2 + \left\{ \frac{4.343}{\sqrt{I \cdot F}} [1.0 + 10^{0.1(T-Z)}] \right\}^2}$ .

	<b>Radar Frequency (GHz)</b>	<b>PIA Uncertainty (dBZ)</b>	<b>Z Baseline Uncertainty* (dBZ)</b>	<b>Z Threshold (dBZ)</b>	<b>Radar Integration Time (ms)</b>
<b>Satellite A</b> (Similar to CloudSat)	94.0	1.25	1.0	-30.0	160.0
<b>Satellite B</b> (Similar to GPM)	13.6	1.25	1.0	12.0	29.0
	35.5	1.25	1.0	12.0	42.0
<b>Satellite C</b> (Triple-Frequency)	13.6	1.25	1.0	0.0	29.0
	35.5	1.25	1.0	0.0	42.0
	94.0	1.25	1.0	-50.0	160.0

TABLE 2.2. Passive microwave frequencies and measurement uncertainties for the 3 theoretical satellite architectures considered in this study.

	<b>T<sub>B</sub> Frequencies (GHz)</b>	<b>NEDT (K)</b>
<b>Satellite A</b>	94.0	4.0
<b>Satellite B</b>	10.6, 18.7, 23, 37, 89, 166, 183±3, 183±7	0.77, 0.6, 0.51, 0.41, 0.31, 0.65, 0.56, 0.47
<b>Satellite C</b>	13.6, 35.5, 94.0	1.0, 1.0, 1.0

Since the DSD measurements contain information only at the surface it is necessary to artificially create vertical structure above. We assume that the raining column extends uniformly from the surface to a height of 1 km, and that cloud water is present from 500 m to 2000 m. The amount of cloud water in each vertical level is assumed to increase linearly, as would be expected if the cloud droplets were growing adiabatically as they ascended through a layer of saturated air (e.g. Miller et al. 2016). For the size of the cloud droplets, we assume an inverse exponential size distribution at each level:

$$n(d) = n_0 e^{-\lambda d}. \quad (2.3)$$

Here  $n_0$  is the intercept parameter and  $\lambda$  is the slope parameter, which can be related to the effective radius  $r_e$  by

$$\lambda = \frac{3}{2r_e}. \quad (2.4)$$

We construct the cloud water distribution such that  $n_0$  stays the same throughout the cloud, but that  $r_e$  increases toward cloud top, with the additional constraint that the average  $r_e$  for the whole cloud is  $11 \mu\text{m}$ . A coordinated intercomparison of satellite cloud data records (Stubenrauch et al. 2013) found a consistent peak in cloud droplet effective radius at this value, and it is also broadly in line with other studies such as Witte et al. (2018) and Sinclair et al. (2021). Figure 2.2 shows qualitatively what the vertical profile of cloud and rain looks like. The scenario is highly idealized but serves our purposes of evaluating DSD-related retrieval uncertainties.

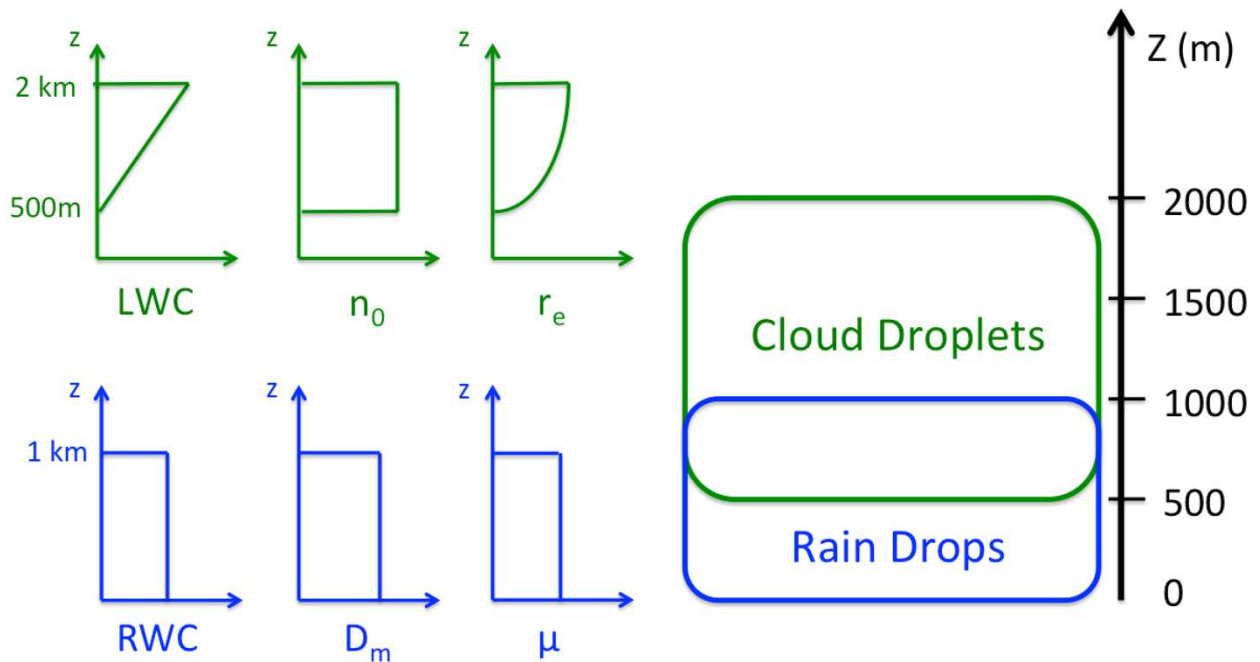


FIG. 2.2. Schematic of the cloud and rain profiles used in our experiments. The axes of the left qualitatively show the vertical profiles of relevant cloud DSD parameters (top; green) and rain DSD parameters (bottom; blue).

### 2.3.2 Optimal Estimation Retrieval Algorithm

From the simulated satellite observations, we use an optimal estimation (OE) retrieval algorithm to try to retrieve the cloud liquid water path and the DSD parameters necessary to calculate the cloud base rain rate (RR). The method is based on Bayes' Theorem,

$$P(\mathbf{x}|\mathbf{y}) = \frac{P(\mathbf{y}|\mathbf{x})P(\mathbf{x})}{P(\mathbf{y})}, \quad (2.5)$$

where  $\mathbf{y}$  is the measurement vector containing all of the observations being considered and  $\mathbf{x}$  is the state vector consisting of the hydrometeor properties being retrieved.

According to Equation 2.5, in order to find the value of  $\mathbf{x}$  for which the posterior probability  $P(\mathbf{x}|\mathbf{y})$  is maximized, one should search for the state vector that maximizes the product of the a priori probability of that state,  $P(\mathbf{x})$ , with the probability of measuring the set of observations  $\mathbf{y}$  if  $\mathbf{x}$  was indeed the proper state vector,  $P(\mathbf{y}|\mathbf{x})$ . As demonstrated by Rodgers (2000), if one assumes Gaussian errors, maximizing  $P(\mathbf{x}|\mathbf{y})$  is equivalent to minimizing the following cost function,  $\Phi$ :

$$\Phi = (\mathbf{x} - \mathbf{x}_a)^T \mathbf{S}_a^{-1} (\mathbf{x} - \mathbf{x}_a) + [\mathbf{y} - \mathbf{f}(\mathbf{x}, \mathbf{b})]^T \mathbf{S}_y^{-1} [\mathbf{y} - \mathbf{f}(\mathbf{x}, \mathbf{b})]. \quad (2.6)$$

Here  $\mathbf{f}$  is a forward model based on radiative transfer theory that is able to simulate all of the observations that make up the observation vector. The vector  $\mathbf{b}$  contains additional ancillary information, besides those parameters that make up  $\mathbf{x}$  and are directly solved for, that is required by the forward model to simulate the full observation vector.

The first term of the cost function weights departures of a potential state vector  $\mathbf{x}$  from the a priori state vector  $\mathbf{x}_a$  by the assumed errors in the a priori state, as described by the a priori covariance matrix  $\mathbf{S}_a$ . Similarly, the second term weights the difference between observations  $\mathbf{y}$  and forward model output  $\mathbf{f}(\mathbf{x}, \mathbf{b})$  by a second error covariance matrix, the  $\mathbf{S}_y$  matrix, which describes the uncertainties in both the observations and the forward model. Using the Gauss-

Newton method, we iteratively solve for the value of  $\mathbf{x}$  at which the gradient of the cost function,  $\nabla_{\mathbf{x}}\Phi$ , is equal to zero. For more background on the OE algorithm, see Schulte and Kummerow (2019) and Schulte et al. (2020), as the algorithm is based on the same mathematical and radiative transfer backbone as the PMW inversion algorithm (CSU 1DVAR) used in those studies. This algorithm differs from the CSU 1DVAR in that it retrieves a different set of parameters and is built to incorporate radar observations (both Z and PIA) into the observation vector in addition to  $T_B$ .

The state vector contains 4 parameters: the vertically integrated cloud liquid water path (CLWP), the rain water content (RWC) of the DSD, the mass-weighted mean diameter ( $D_m$ ) of the DSD, and the normalized gamma shape parameter ( $\mu$ ) of the DSD. CLWP, RWC, and  $D_m$  are retrieved in logarithmic space because their underlying distributions are not normally distributed, but are much closer to a lognormal distribution. RWC,  $D_m$ , and  $\mu$  are all functions of height in reality, but we assume that they are constant throughout the raining column and so can be thought of as column averages. The size of the observation vector depends on the satellite architecture used as well as the atmospheric profile being considered. It is equal to the number of PMW channels in the architecture, plus the number of PIA frequencies, plus the number of valid radar observations. A valid radar observation, for these purposes, is one for which the reflectivity exceeds the minimum detectable signal for that satellite and radar frequency.

The forward model  $\mathbf{f}(\mathbf{x}, \mathbf{b})$  uses the same radiative transfer models (i.e., QuickBeam and MonoRTM, introduced in Section 2.2.3) that are used for creating simulated satellite observations. Because the OE forward model is based on the same code, note that the forward model errors are underestimated compared to what would be expected in real-world retrievals.

Eliminating this forward model error allows us to isolate other sources of error, such as DSD representation error, that are the focus of our study.

### 2.3.3 Error Covariance Matrices

The  $\mathbf{S}_a$  and  $\mathbf{S}_y$  matrices are constructed based on the statistics of the related error distributions. For example, when using the OceanRAIN disdrometer data, the  $\mathbf{S}_a$  matrix contains the variance of  $\log_{10}(\text{LWP})$ ,  $\log_{10}(\text{RWC})$ ,  $\log_{10}(\text{D}_m)$ , and  $\mu$  found in the OceanRAIN dataset on the diagonal, and the covariances between the OceanRAIN parameters make up the off-diagonal elements. The  $\mathbf{S}_y$  matrix is meant to account for both forward model and sensor uncertainties, though in most cases the forward model uncertainty dominates. The forward model uncertainties are estimated by comparing the simulated observations produced by the simplified forward model against simulations where the various assumptions of the forward model are relaxed (in the real world, one could compare against true observations). Then the sensor uncertainties are added to create the full  $\mathbf{S}_y$  matrix. See Schulte and Kummerow (2019) for more details about the construction of covariance matrices.

One disadvantage of an OE algorithm is that, even if there were no observation or forward model uncertainties, the algorithm would only be guaranteed to converge to the proper solution if the problem were linear. Precipitation retrievals are known to be not entirely linear (e.g. Stephens and Kummerow 2007). Other retrieval techniques exist that are less subject to nonlinearities, such as neural network based algorithms (Beusch et al. 2018; Tang et al. 2018; Chen et al. 2019) or Markov Chain Monte Carlo (MCMC) approaches (Posselt et al., 2017; Xu et al. 2019). Still, the OE approach provides several benefits. The algorithm is based on physical radiative transfer models rather than statistical correlations, retrieval performance can be compared across different satellite architectures in a consistent and simple fashion, and the

method provides *a posteriori* error estimates that can be traced directly to the underlying uncertainties and the physics of the problem. In most cases, as explored further in Section 2.4, the fundamental uncertainties due to the nonlinearities of rainfall retrieval are much smaller than the retrieval errors that result from the other sources of uncertainty that we consider.

## 2.4 Base Case Uncertainties

### 2.4.1 Uncertainties Due to Sensor Noise, Detection Limits, and Nonlinearities

In this first experiment, we quantify how sensor limitations affect retrieval errors and uncertainties. We use the OceanRAIN NG-fitted DSDs to create simulated satellite observations. Because the disdrometer observations do not tell us anything about how much cloud water is in the column, we nominally set the column-integrated CLWP so that it is equal to twice the column-integrated rain water path (note that the OE algorithm is unaware of this assumed relationship and is free to converge to any CLWP value regardless of RWP). Random Gaussian noise is added to the synthetic observations to simulate the physical limitations of the satellite instruments, using the measurement uncertainty values given in Tables 2.1 and 2.2. Then, after adding the measurement noise, if a certain radar measurement has a value below the detection limits given in Table 2.1, the measurement is set to have no radar echo. This has the effect of getting rid of about 6% of cloud-only radar observations for Satellite A, all of the cloud-only and about 8% of the rain observations for Satellite B, and reducing Satellite C to only a single (W-band) frequency for cloud-only observations. The algorithm then retrieves the four elements of the state vector, from which the RR is calculated.

Figures 2.3-2.5 shows the results of this experiment. Starting with Satellite A, we see that even with only W-band observations, the CLWP is well constrained. The retrieval error is quite

close to 0% throughout the whole range of CLWP, with an overall retrieval bias (defined as the median retrieval error) of 1.2% and an interquartile range (IQR) of errors of 18.2%. The IQR is the difference between the 25<sup>th</sup> percentile and 75<sup>th</sup> percentile errors. On the other hand, the rain water path (RWP) is biased low (-11.0%) and the column-averaged RR also biased slightly low (-1.6%), although the RR bias mostly comes from the higher rain rate cases. Both parameters show considerable spread. Unsurprisingly, given that it has only a single radar frequency, Satellite A shows little skill in retrieving  $D_m$ . The retrieved  $D_m$  values are clustered quite closely around the a priori value (represented by the red dotted line), resulting in overestimation at low  $D_m$  and underestimation at high  $D_m$ .

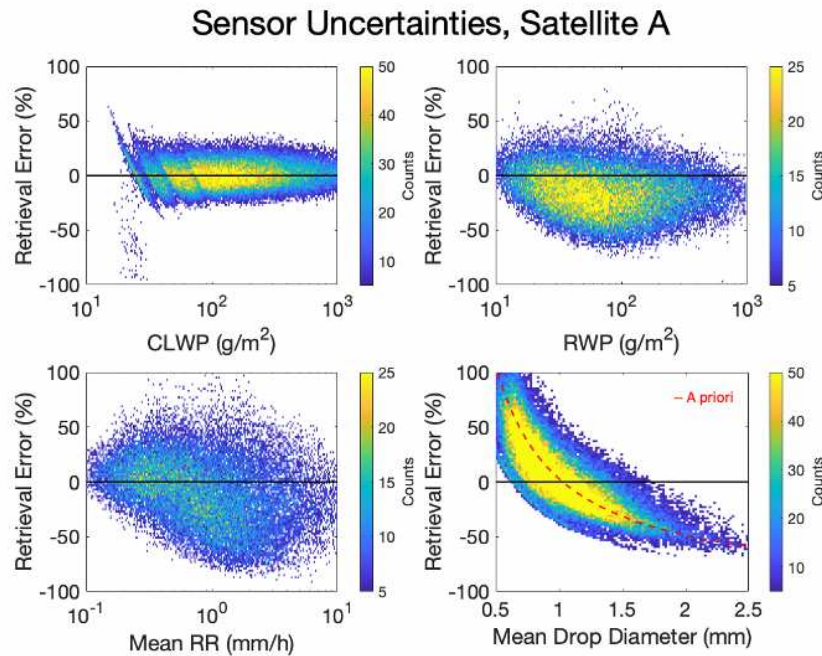


FIG. 2.3. Density plots of retrieved error in CLWP, RWP, column-averaged RR, and column-averaged  $D_m$  compared to the true value that was used to make the underlying simulated satellite observations, for Satellite Architecture A. This experiment considers only sensor noise and detection limits as a source of uncertainty. The red dashed line shows the error in  $D_m$  that would be incurred if the a priori assumption was used.

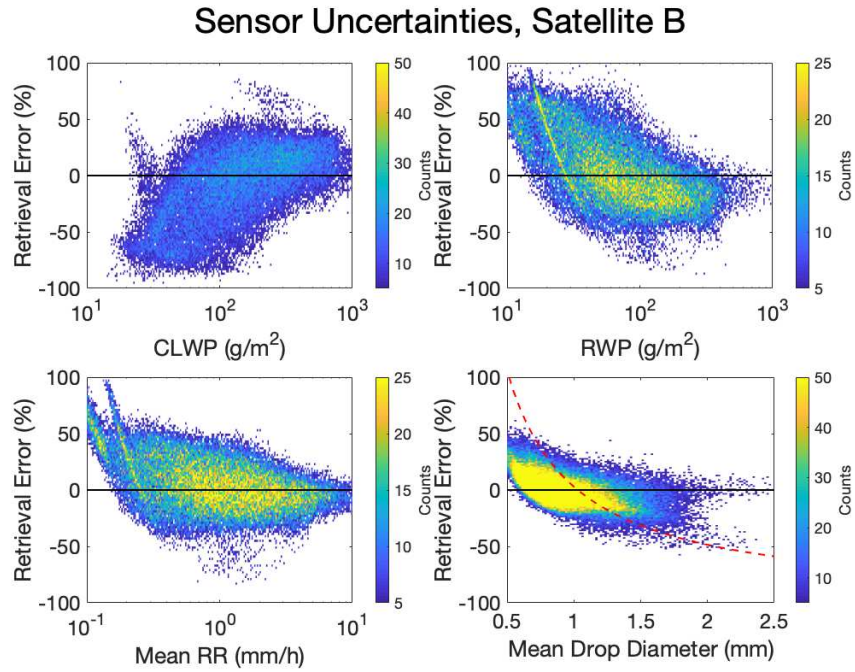


FIG. 2.4. As in Figure 2.3, but for Satellite B.

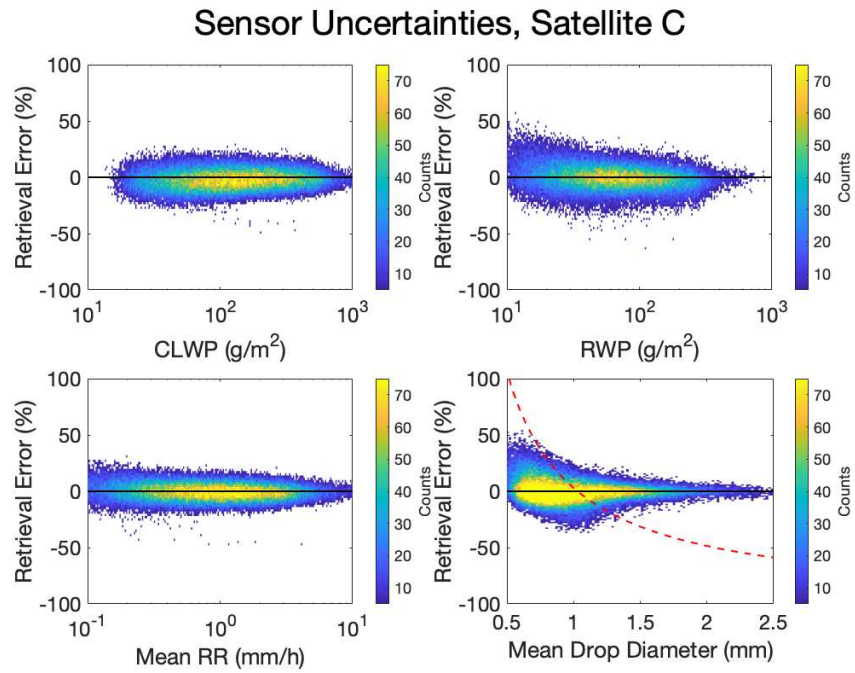


FIG. 2.5. As in Figure 2.3, but for Satellite C.

Satellite B demonstrates more skill at retrieving  $D_m$ , and to a lesser extent RWP and RR. However, CLWP is not well constrained, with a bias of -4.8% and an IQR of 53.2%. Since cloud drops as well as small rain drops fall below the radar detection limits, the architecture struggles to differentiate cloud drops from drizzle drops. This underscores the importance of the W-band radar for cloud/rain partitioning. Satellite C, on the other hand, does a remarkably good job of constraining all of the retrieved quantities of interest. There is less bias in the retrieved CLWC, RWP, and RR, and the IQRs are relatively small at 13.2%, 16.6%, and 11.2%, respectively.

We also ran an experiment in which we input simulated satellite observations directly into the retrieval algorithm, without adding sensor noise or detection limits. Thus the only limitations faced by the retrieval in this case were the fundamental nonlinearities of the inversion problem. The IQRs from these experiments can be seen in Figure 2.6. From these results it is clear that the nonlinearities of the problem should not be a major concern, except perhaps for the case of retrieving RR and RWP from Satellite A, for which there is a slight negative bias in the retrieved values.

#### *2.4.2 Ancillary Assumption Uncertainties*

In another experiment, we add random noise (see Section 2.2.4 for details) to the atmospheric profiles before simulating satellite observations, in order to estimate the uncertainty that is introduced into real-world satellite precipitation retrievals by ancillary assumptions. Once the satellite observations have been simulated, we add measurement noise, eliminate observations below detection limits, and run the OE algorithm with our original assumptions about the atmospheric profile intact. The main effect of introducing these uncertainties is, as expected, an increase in the IQR of retrieval errors for all satellite architectures. This increase is perhaps most pronounced for the retrieval of CLWP from Satellite B, for which the IQR

increases from 53.2% to 80.2%. Most of this architecture's CLWP information comes from  $T_B$ , so errors in the assumed temperature and water vapor profiles cause  $T_B$  differences that translate into increased retrieved CLWP errors. Otherwise, the error biases in this experiment stay close to zero, but with a modestly larger spread for most parameters of interest.

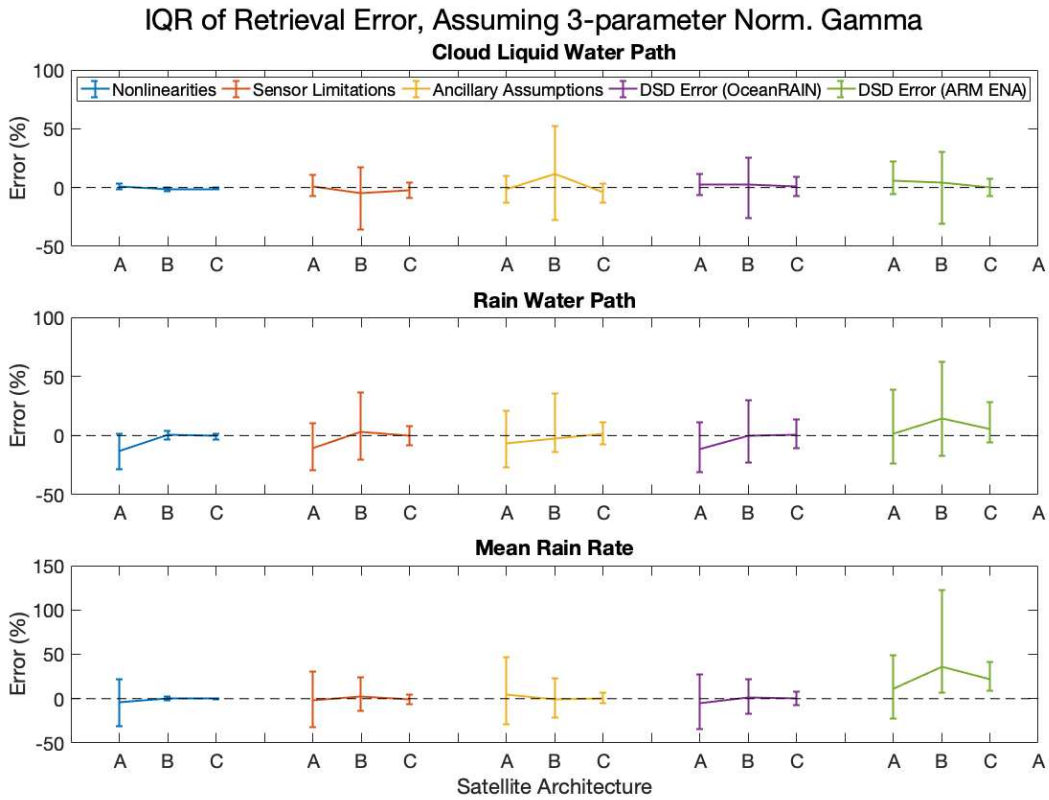


FIG. 2.6. Each bar shows the interquartile range, i.e. the 25<sup>th</sup>, 50<sup>th</sup>, and 75<sup>th</sup> percentile of retrieval errors, in either CLWP (top), RWP (middle), or column-averaged RR (bottom), for a given experiment and satellite architecture. The satellite is indicated by the letter on the x-axis. The experiment being considered is indicated by the color of the bars. The blue bars are for fundamental nonlinearities only, the red bars add sensor uncertainties and detection limits, and the yellow bars add uncertainties in the ancillary assumptions. The purple bars are for the experiments with binned OceanRAIN DSDs and the green bars the experiments with binned ARM DSDs.

## 2.5 DSD-related Uncertainties

### 2.5.1 Experiments with Binned DSDs

In these next series of experiments, we explore how DSD assumptions affect retrieval uncertainties and biases. First, we simulate satellite observations using the raw drop concentrations for each size bin, instead of using the fitted NG DSD parameters from OceanRAIN. As discussed in the Data section, we use only rain drops larger than 0.55 mm in diameter. As in the base case, we add sensor noise and eliminate observations below detection limits, and then use these simulated satellite observations to retrieve the cloud and rain parameters, assuming a 3-parameter NG rain DSD. To be consistent, we adjust the forward model in the OE algorithm so that it also ignores rain drops smaller than 0.55 mm in size. The resulting spread of retrieval errors can be seen in Figure 2.6. Compared to the base case, the spread is slightly larger but not by much. This indicates that the NG model can capture the real-world variability of drop spectra (at least on the larger end of the size range) and is appropriate for use in retrieval algorithms, confirming the findings of previous studies (e.g., Testud et al. 2001, Bringi et al. 2002, Adirosi et al. 2014). Most of the biases are near-zero, with the exception being a slight underestimation of RWP and RR for Satellite A, which is also present in the base case experiment. Since Satellite A only has W-band observations, and W-band Z tend to saturate at moderate rain rates, it would make sense that this architecture could underestimate rain in heavier precipitation.

To investigate the effect of including smaller drops from 0.1-0.55 mm, we repeat the same experiment but use binned DSDs from the ARM ENA site instead of OceanRAIN observations. These observations differ from the OceanRAIN observations not only because of their inclusion of small drops but also because the frequency of occurrence of very light rain and

drizzle is much larger in this dataset compared to the OceanRAIN dataset, as can be seen in Figure 2.7. This is consistent with the findings of Giangrande et al. (2019) that the ENA site receives a significant portion of its precipitation from marine low clouds and that median raindrop sizes at the site are smaller than what is typically seen at other locations around the globe. The resulting retrieval errors are larger using the ARM DSDs than the OceanRAIN DSDs, especially for RWP and RR (refer again to Figure 2.6). There is also a bit of a retrieval bias. While the retrieved RWP is biased only moderately high, the retrieved RR is biased 11.6% to 36.3% high, depending on the satellite. Thus, while the assumption of a NG DSD works well for the retrieval of light to moderate rain from OceanRAIN, it might not be as appropriate for the retrieval of drizzle rates. Others have found that the generalized gamma model (Thurai et al. 2018), which includes a second shape parameter, can more accurately represent the drizzle mode of the DSD, although retrieval gains would only be realized if satellite measurements were able to accurately detect changes to this parameter.

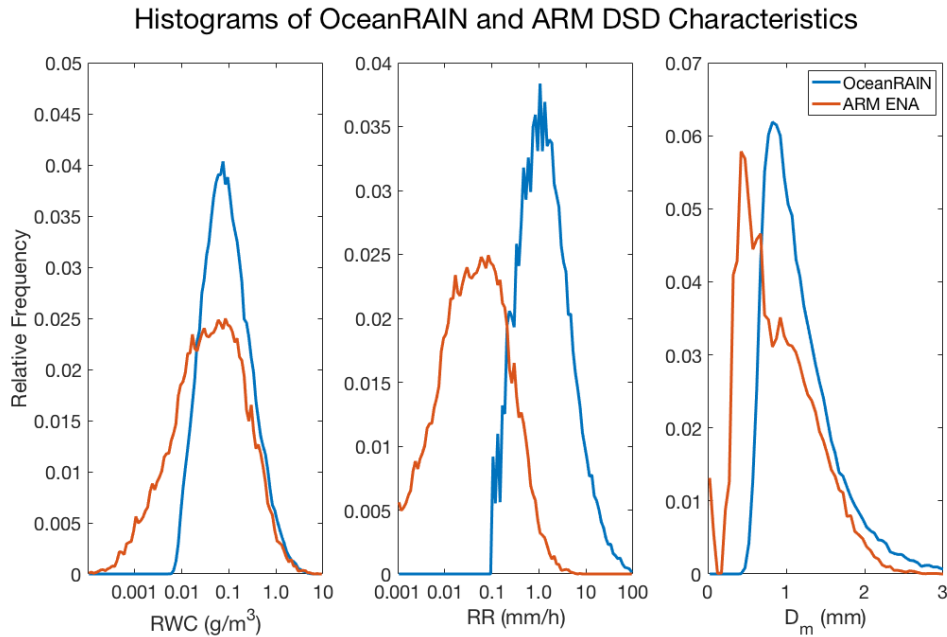


FIG. 7. Histograms showing the RWC, RR, and D<sub>m</sub> distributions for the OceanRAIN and ARM East North Atlantic disdrometer datasets.

### 2.5.2 Impacts of Assuming Alternative DSD models

The three free parameters of the normalized gamma DSD model allow for most realistic DSDs to be reasonably fit by a NG distribution. Most precipitation retrieval algorithms, however, do not retrieve 3 DSD parameters. If only one or two radar frequencies are employed, there is a reasonable argument to be made that one should only retrieve one or two DSD parameters, as otherwise the inversion could be under constrained. Still, using a DSD with fewer free parameters will make it harder for the forward model used in the retrieval to mimic the true underlying DSD, leading to greater uncertainty in retrieved rain rates. In this section we attempt to quantify the uncertainties and biases resulting from assuming 3 alternative DSD models in our OE algorithm instead of a 3-parameter NG.

The first model we test is a 2-parameter NG model, where we retrieve column-averaged RWC and  $D_m$  as before but the shape parameter  $\mu$  is constrained to always be equal to 3, as in the GPM dual-frequency radar precipitation retrieval (Seto and Iguchi 2015). We also test two single-parameter models, where we only retrieve column-averaged RWC. The assumptions made in the models are then enough to uniquely determine the full drop size spectrum. The first model is that of Marshall and Palmer (1948), which was based on raindrop records on dyed filter papers from Ottawa, Canada. We use this model as a reference because it is well-known and was used in early formulations of the CloudSat 2C-RAIN-PROFILE algorithm (Lebsock and L'Ecuyer 2011). We also test the model of Abel and Boutle (2012), which is currently used by the 2C-RAIN-PROFILE algorithm (Lebsock 2018). Both the Marshall-Palmer (MP) and Abel and Boutle (AB) models are based on inverse exponential distributions, but differ in how the shape of the distribution is related to the overall RWC of the DSD. In the AB model, the intercept parameter is related to the slope parameter by the equation

$$N_0 = x_1 \lambda^{x_2}, \quad (2.7)$$

where  $x_1$  is set to 0.22 and  $x_2 = 2.2$ . The slope parameter  $\lambda$  is determined from the rain mass mixing ratio  $q_R$  by the equation

$$\lambda = \left( \frac{\pi \rho_w x_1}{\rho_{air} q_R} \right)^{\frac{1}{4-x_2}}, \quad (2.8)$$

where  $\rho_w$  and  $\rho_{air}$  are the densities of water and the air parcels, respectively. In the AB model, DSDs with a high RWC have a lower intercept parameter (fewer very small drops) than those with low RWCs, making up this difference with even more large drops. Under MP assumptions, all DSDs have the same intercept parameter (i.e., similar numbers of very small drops), but those with a larger RWC have more large drops.

We repeat the OceanRAIN binned DSD experiment, but this time assuming these different DSDs models in the OE forward model. Figure 2.8 shows the effect that assuming each of these simplified DSDs has on retrieval errors. Compared to the control run assuming a 3-parameter NG, holding  $\mu$  fixed doesn't increase the retrieval uncertainties very much. There is, however, a slight tendency to substitute cloud water for rain water, with a high bias in retrieved CLWP and a low bias in retrieved RWP (for Satellites A and B). The retrieved rain rate, on the other hand, doesn't show much of a bias for any of the satellite architectures. Both single-parameter DSD models (in the yellow and purple) yield considerably more retrieval uncertainty than the 2 or 3-parameter NG models. In addition, they also lead to a positive bias in retrieved RWP and RR, no matter which satellite architecture is considered. This is especially true for the AB model, for which the retrieved RWP is biased high by between 17-47% (depending on satellite architecture), and the retrieved RR biased high by between 16-33%. Figures 2.9 and 2.10 show the full retrieval error densities for Satellite C assuming either the 3-parameter NG model (Fig. 2.9) or the AB model (Fig. 2.10). Comparing the two figures, it is even more evident that

the AB model assumption results in an overestimation of retrieved RWP and RR, especially at rain rates less than about 5 mm/h. Meanwhile, the CLWP is consistently biased high and  $D_m$  consistently biased low.

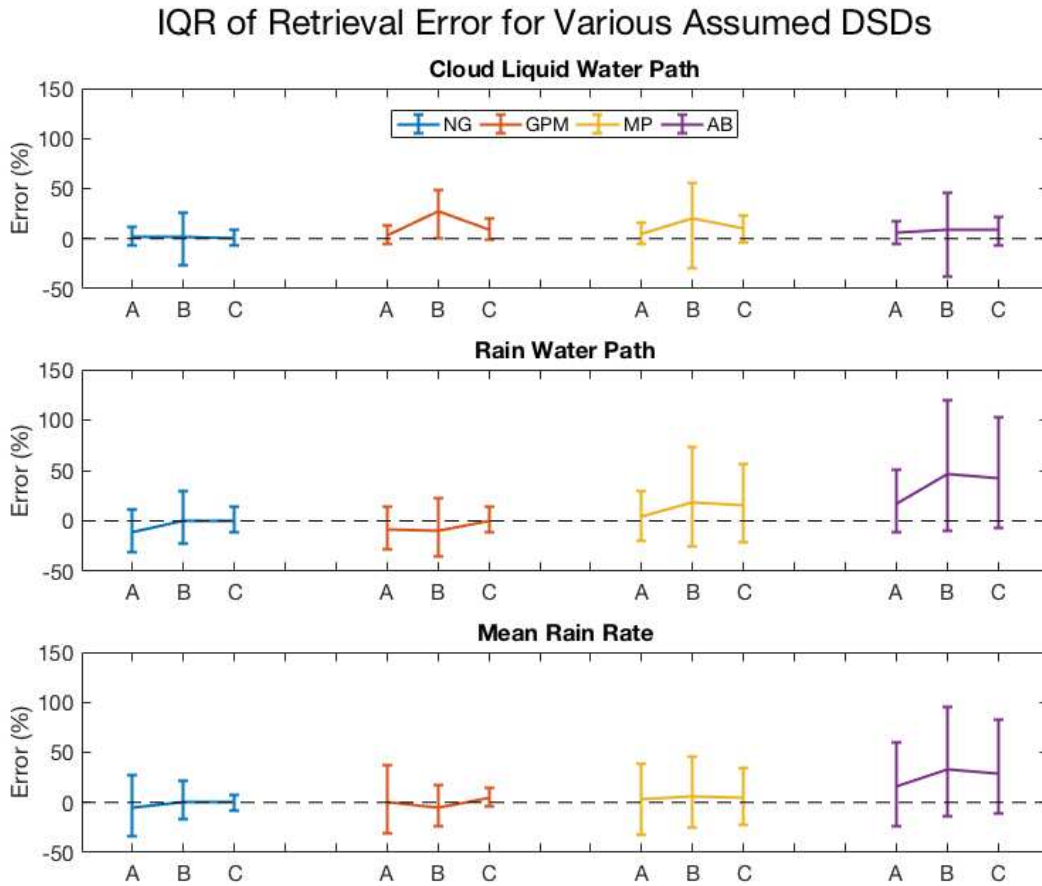


FIG. 2.8. IQR of retrieval errors for a given satellite architecture, using a forward model in the OE algorithm that assumes either a 3-parameter NG DSD (blue), a 2-parameter NG distribution (red), a Marshall-Palmer distribution (yellow), or an Abel & Boutle distribution (purple).

### Satellite C Retrieval Errors Assuming Normalized Gamma DSD

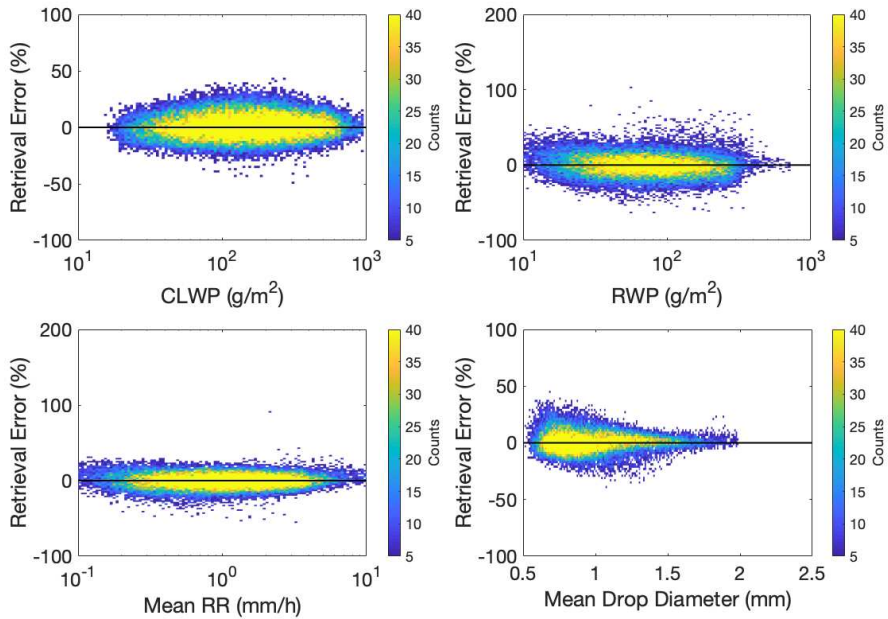


FIG. 2.9. As in Figure 2.5, but using OceanRAIN binned DSDs to simulate observations and assuming a 3-parameter normalized gamma DSD model in the OE.

### Satellite C Retrieval Errors Assuming Abel & Boutle DSD

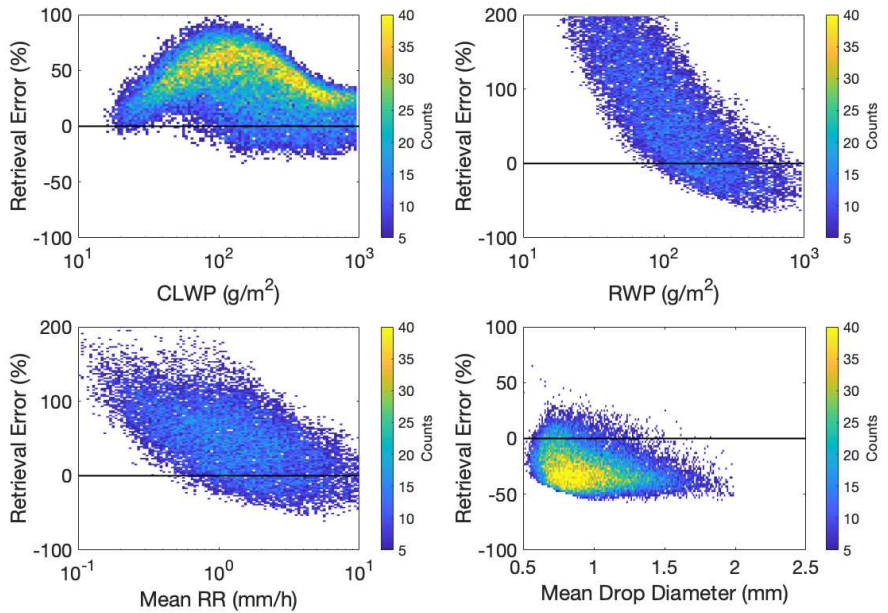


FIG. 2.10. As in Figure 2.5, but using OceanRAIN binned DSDs to simulate observations and assuming the 1-parameter normalized DSD model of Abel and Boutle (2012) in the OE algorithm.

To test the robustness of these results, we performed the same set of experiments using the ENA binned DSDs to simulate satellite observations. In this case the errors seen in the OceanRAIN experiment are magnified even more, as shown in Figure 2.11. RR biases are around 50% for MP and close to 100% for AB. From these results, it is clear that the DSD assumed in a retrieval algorithm can have a very large impact on retrieved RR. Notably, the AB DSD doesn't seem very appropriate for cases of light rain, which dominate the ARM ENA dataset. This could partially explain why CloudSat tends to retrieve more rain over the high latitudes than GPM (Behrangi and Song 2020). In both the OceanRAIN and ENA experiments, we find that assuming the AB (CloudSat) DSD compared to the 2-parameter NG (GPM) DSD leads to retrieved RRs that are about 25-50% higher.

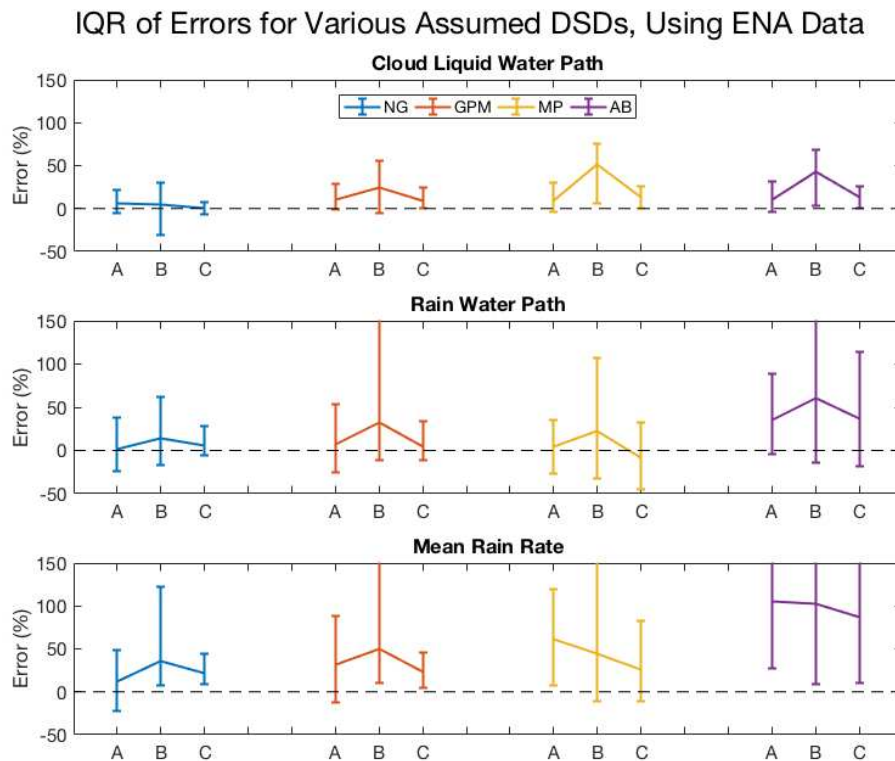


FIG 2.11. As in Figure 2.8, but using ARM ENA disdrometer data for the underlying rain drop distributions instead of OceanRAIN.

We believe this overestimation from the AB and MP models stems in part from the fact that the MP and AB models assume size spectrums that are too heavily concentrated towards small drops. Figure 2.12 plots the relationship between RR and  $D_m$  in the OceanRAIN and ARM datasets, along with the curves that result from the AB and MP models. For reference, we also include RR- $D_m$  curves reported by Protat et al. (2019a), Liao et al. (2020), and Seto et al. (2021). Both the AB and MP models predict a much higher RR for a given  $D_m$  than what is observed in either disdrometer dataset or predicted by the other models, indicating a higher overall RWC. Z values are most strongly affected by the largest drops in a given rain volume, because in the Rayleigh regime reflectivity scales as  $D^6$ . If the OE algorithm is assuming one of these models, the implication is that, in order to create forward modeled reflectivities that match what has been observed (i.e. have a similar  $D_m$ ), the OE must assume a much higher overall RWC. This effect is so large that it translates into a higher RR, despite the partially compensating effect that small drops fall more slowly than large ones.

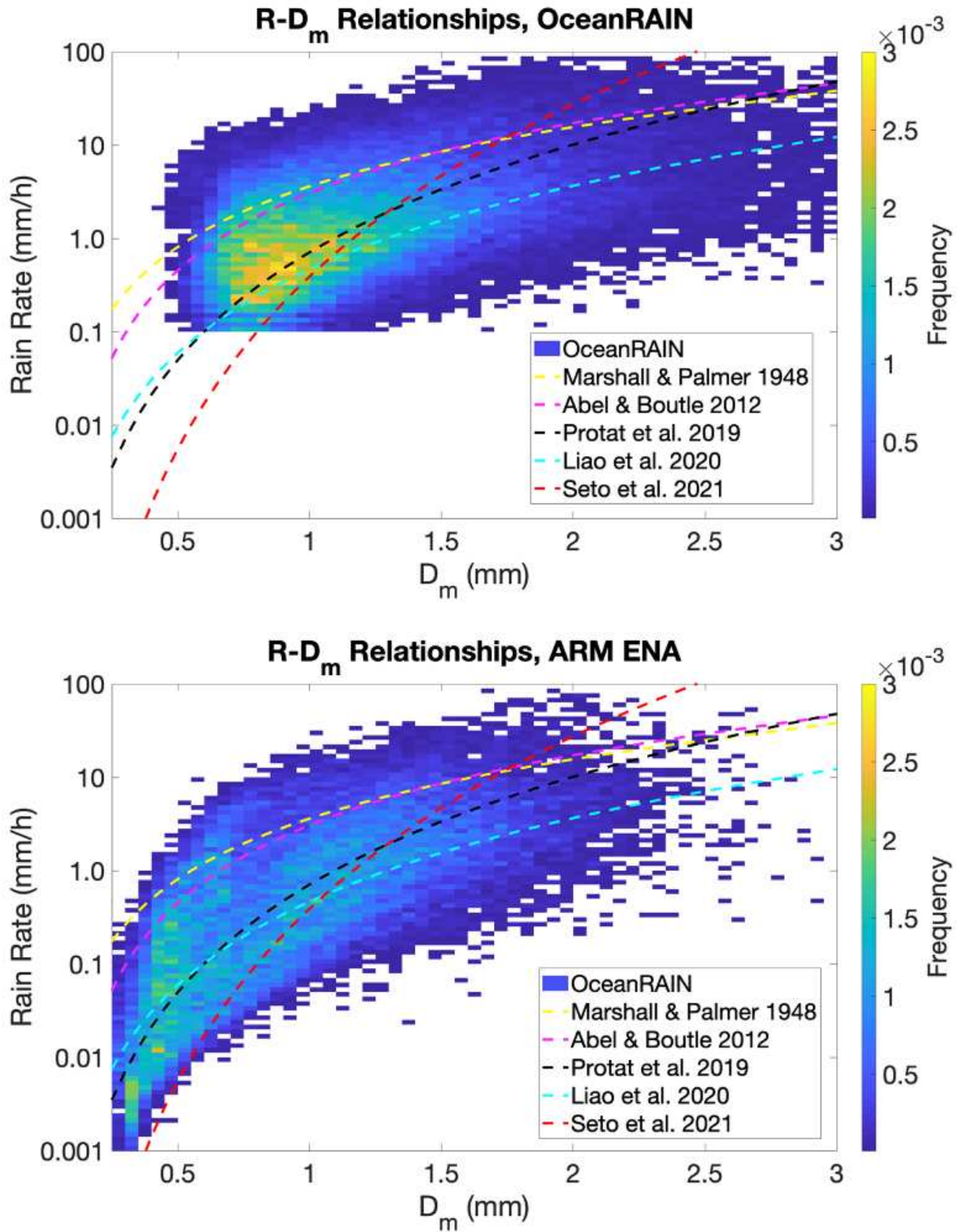


FIG. 2.12. Frequency distributions of OceanRAIN (top) and ARM (bottom) DSD observations according to their rain rate (y-axis) and mass-weighted mean drop diameter (x-axis). The dotted curves show the R-D<sub>m</sub> relationships reported by several different studies (cited in the text).

## 2.6 Conclusions

There are clearly many challenges and uncertainties to deal with in retrieving precipitation from a satellite platform, including important ones that we have not dealt with in this study, such as surface clutter, frozen hydrometeors, field of view heterogeneities, and vertical structures that can differ substantially from the idealized scenario assumed in this study. Many of these uncertainties will be quantified in Chapter 3 of this dissertation. It is also likely that our use of a priori data biases the retrieval results towards the correct answer, so the uncertainties we calculate should be thought of as very much best-case values. Our results nevertheless offer important insight into the significance of DSD uncertainty when it comes to retrieving rain.

One common thread running through all of our experiments is the importance of W-band observations for differentiating cloud water from rain water. For satellite architectures A and C, both of which include 94 GHz radars, CLWP is generally the easiest of the retrieved variables to constrain, but CLWP uncertainties increase greatly for satellite B, which has a tendency to substitute rain water for cloud water and vice versa. This is because both cloud droplets and drizzle drops tend to have reflectivities below the Ka/Ku detection limit of 12 dBZ. It is thus very important that future satellite missions include W-band radar observations. Of the other retrieved variables, the DSD shape parameter  $\mu$  is the hardest to retrieve accurately, followed by the volume weighted mean diameter  $D_m$ . For the purposes of deriving rain rate,  $D_m$  is much more consequential.

Fundamental nonlinearities set a lower limit on the retrieval uncertainties one can expect from an optimal estimation based retrieval. For satellites B and C, these pale in comparison to the other uncertainties considered in this study, while for satellite A, which only has one radar

frequency, the nonlinear nature of the inversion problem presents more of a challenge. Adding sensor noise and detection limits increases the retrieval uncertainty but does not lead to a retrieval bias. We see a similar affect when we consider uncertainties in the ancillary assumptions about the surface and atmospheric profile that the retrieval must make in order to simulate satellite observations.

Our assumption of a 3-parameter NG DSD works well for the OceanRAIN disdrometer data. However, DSDs from the ARM ENA disdrometer are not as well represented, and the NG assumption leads to a positive bias in retrieved rain rate as the retrieval algorithm tends to assume the drops are larger than they actually are. Even larger biases result when single moment DSD parameterizations are assumed in the retrieval algorithm, including positive biases near 100% for retrieving rain rate from the ENA disdrometer data. Compared to the two parameter NG DSD (used by some GPM algorithms), the single parameter AB model (used by the CloudSat 2C-RAIN-PROFILE algorithm) retrieves rain rates that are 25-50% higher, depending on satellite architecture. Even between the two simple DSD models we consider, large differences in retrieval biases exist. These experiments clearly show that DSD assumptions have a large impact on satellite precipitation retrievals.

Our results are focused on warm rain uncertainties, in that our simulated satellite observations include only liquid hydrometeors. We would expect retrieval uncertainties for more complicated precipitation types to be larger due to additional nonlinearities and the difficulty in accurately modeling ice particle shapes in a forward model. An important caveat is that we cannot guarantee that the OceanRAIN and ARM surface observations used in this study resulted from warm-rain-only precipitation processes. While ARM ENA observations come predominantly from low marine clouds (Giangrande et al. 2019), we have not attempted to

exclude DSDs from deep clouds in our analysis. We also caution that we have used surface DSD observations, when in reality satellite radars cannot sense below 750 m above the surface (at best) due to surface clutter. Given these limitations, we would stop short of saying that any of the DSD models considered in this study are definitively “best” for retrieving warm rain. It is possible, for instance, that if one were looking at only warm rain processes at 1000 m above the surface (where less evaporation of small drops has taken place), the AB model would be more appropriate. In this hypothetical, DSD assumptions would still be an important source of retrieval bias, since the operational CloudSat and GPM algorithms assume very different  $R$ - $D_m$  relationships (see Fig. 2.12). Regardless of which one is more correct, the fact that they are so different likely explains part of why rain rates retrieved from GPM are lower than those from CloudSat in light rain regimes (Behrangi and Song 2020).

Our findings offer a cautionary tale for all satellite retrieval algorithms. Careful attention needs to be paid to DSD assumptions when interpreting and comparing retrieved rain rates. Simple DSD parameterizations may not be appropriate, especially for remote, high-latitude oceanic regimes. Our work shows that, when multiple radar frequencies are available (such as for architecture C in this study), retrieving two or three moments of the DSD can be greatly helpful in narrowing retrieval uncertainties because a greater variety of DSD shapes can be described by such a model. This should be an important consideration when designing the next generation of satellite precipitation missions and algorithms. For missions such as CloudSat, where the limited information content of a single frequency radar makes it harder for multiple DSD moments to be retrieved, more research is needed into how DSD shapes are regime dependent and whether these dependencies could be usefully incorporated into a retrieval algorithm.

# CHAPTER 3: HOW ACCURATELY CAN WARM RAIN REALISTICALLY BE RETRIEVED WITH SATELLITE SENSORS? PART 2: HORIZONTAL AND VERTICAL HETEROGENEITIES

## 3.1 Introduction

Warm rain processes are quite common over the open oceans and have important effects on large-scale circulations and on Earth's radiative energy balance (Kubar et al. 2009; Nuijens et al. 2017; Jing and Suzuki 2018; Nelson and L'Ecuyer 2018). However, many warm rain dominated regions of the globe feature large discrepancies between satellite rainfall retrievals (Berg et al. 2010; Andersson et al. 2011; Behrangi et al. 2016; Behrangi and Song 2020). This chapter is the second of a two-part study designed to better understand what the most important sources of uncertainty are for the retrieval of warm rain and drizzle, and how the inclusion of different satellite measurements affects retrieval uncertainty. This work is particularly relevant as NASA plans its next major precipitation measurement mission, tentatively given the name Atmosphere Observing System (AOS; Stavros et al. 2021). This mission comes out of NASA's last decadal survey and the desire to design a mission to link the study of aerosols, clouds, convection, and precipitation (NASEM 2018).

In the first part of this study (Chapter 2), we studied several different types of retrieval uncertainty using surface disdrometer data from the Ocean Rainfall and Ice-phase Precipitation Measurement Network (OceanRAIN; Klepp et al. 2018) and the Atmospheric Radiation Measurement (ARM) Eastern North Atlantic (ENA) atmospheric observatory (Giangrande et al. 2019). We developed an optimal estimation (OE) retrieval algorithm and applied it to synthetic observations generated for three different satellite architectures: one similar to the Global

Precipitation Measurement (GPM) core observatory (Skofronick-Jackson et al. 2017), one similar to CloudSat (Stephens et al. 2002), and one similar to the type of architecture envisioned for AOS. We quantified retrieval uncertainties stemming from instrument noise and detection limits, uncertainties coming from ancillary assumptions about the atmospheric profile, such as the assumed temperature and water vapor profiles, and uncertainties based on the inability of assumed drop size distribution (DSD) models to accurately represent the DSD variability seen in disdrometer observations. We found that the uncertainties due to DSD assumptions were quite significant, with biases in retrieved rain rate approaching 100% for some simple DSD models.

Disdrometer measurements are valuable because of their ability to accurately measure DSD shapes at a particular point. However, other retrieval uncertainties result from the vertical structure of the raining column, which is not measurable from a disdrometer alone, or from inhomogeneity within the satellite field of view, which likewise is hard to determine from a point measurement. These other uncertainties are the focus of this chapter, and for that reason we rely upon simulations from a state-of-the-art cloud resolving model, the Colorado State University (CSU) Regional Atmospheric Modeling System (RAMS; Cotton et al. 2003; Saleeby and van den Heever 2013). We use synthetic satellite observations generated from these simulations to study three additional sources of retrieval uncertainty: nonuniform beam filling (NUBF), vertical variability in the rain and cloud profiles, and the inability to obtain radar reflectivities close to the surface due to surface clutter.

The fact that NUBF can affect the accuracy of precipitation retrievals has been recognized for decades. Graves (1993) found that passive microwave (PMW) instruments will generally underestimate rain rates due to NUBF. This follows from the fact that the relationship between liquid water path and PMW brightness temperatures ( $T_B$ ) tends to be concave down;

i.e., increasing the liquid water path from zero by a certain amount  $x$  will change the  $T_B$  by more than if  $x$  is increased to  $2x$ . On the other hand, the relationship between rain rate and radar reflectivity ( $Z$ ) is concave up (in the Rayleigh regime). Consequently, as demonstrated by Nakamura (1991), a rain retrieval algorithm that converts measured radar reflectivities (neglecting attenuation) to rain rates will overestimate the rain rate due to NUBF. Meanwhile an attenuation-only based method such as the surface reference technique (SRT; Meneghini et al. 2000) will always underestimate the rain rate, for similar reasons as in the PMW case. The underestimation increases as the attenuation increases, due to either heavier rain or a deeper raining column. Combining these effects, Durden et al. (1998) found that NUBF overall negatively biased rain rate estimates from the Tropical Rainfall Measuring Mission (TRMM) precipitation radar, but that this bias came mostly from convection and other high rain rate cases where attenuation was significant. Many methods for correcting NUBF effects in satellite precipitation retrievals have been proposed or adopted (Zhang et al. 2004; Takahashi et al. 2006; Hilburn and Wentz 2008; Short et al. 2015; Grecu et al. 2016), but validating and improving NUBF correction algorithms remains a challenge (Iguchi et al. 2009; Leinonen et al. 2015). In this chapter, we focus specifically on how NUBF affects the retrieval of light, warm rain, and explore how the competing NUBF effects from active and passive measurements behave in combination for the three satellite architectures from Chapter 2.

Additional retrieval complications not dealt with in Chapter 2 include the many simplifying assumptions made about the vertical structure of the cloud and rain water. Identifying the cloud top height, or especially the cloud bottom height, from a satellite radar or radiometer can be challenging. Within the cloud, assumptions must be made about the way the cloud water is distributed vertically and the size distribution of the cloud drops, unless these

things are explicitly solved for. Perhaps most significantly, Chapter 2 assumed a uniform rain DSD. In reality, rain water tends to increase towards cloud base, as falling drops collect smaller drops, and then decrease due to evaporation below cloud base, with smaller drops preferentially evaporating first (e.g., Comstock et al. 2004; Rapp et al. 2013; Kalmus and Lebsock 2017; Ojo et al. 2021). However, retrieving multiple moments of the DSD at each vertical level in a raining column may not be feasible due to information content limitations. For this reason, many satellite radar retrieval algorithms assume some sort of relationship between DSD parameters in order to reduce the number of free variables that must be retrieved. For example, the CloudSat 2C-RAIN-PROFILE algorithm (Lebsock and L'Ecuyer 2011) assumes an inverse exponential DSD, but the intercept and slope parameters are constrained to follow a strict relationship as defined in Abel and Boutle (2012), hereafter AB12. This relationship can equivalently be expressed in the form of a relationship between rain rate and mass weighted mean diameter (an R- $D_m$  relationship) or between rain water content and  $D_m$  (RWC- $D_m$  relationship). Many alternative DSD relationships meant to reduce the dimensionality of the DSD retrieval problem have been proposed in the literature (e.g., Protat et al. 2019a; Liao et al. 2020; Seto et al. 2021).

Surface clutter is an issue that affects all spaceborne radars. The ocean surface is typically two to five orders of magnitude more reflective than hydrometeors (Marchand et al. 2008). This large signal means that reflection from outside of the nominal radar resolution volume can bleed into the radar range bins above the surface, masking precipitation (Durden et al. 2001; Marchand et al. 2008; Kubota et al. 2016). For the CloudSat CPR, precipitation below about 750 m in height is missed (Tanelli et al. 2008). Surface clutter is even more of a factor for GPM, with the lowest reliable range bin around 1000 m at nadir and rising to 1500 m near the edge of swath (Kidd et al. 2021). Surface clutter could cause a spaceborne radar to miss shallow

precipitation altogether. Even if the top of the raining column is high enough to be detected, assumptions must be made about collision-coalescence processes (e.g., Poracchia et al. 2019) and/or evaporation (Kalmus and Lebsock 2017) if one wants to estimate the surface rain rate.

After first describing the RAMS simulations and the OE retrieval that we used (Section 3.2), we will investigate each of these sources of uncertainty individually. Horizontal NUBF is covered in Section 3.3. Vertical inhomogeneity issues, including algorithm assumptions about the vertical structure as well as vertical NUBF effects, are addressed in Section 3.4. Section 3.5 looks at the effects of surface clutter, and in Section 3.6 we combine all of the sources uncertainty together and quantify how they would affect retrieval uncertainties for a theoretical AOS satellite. Finally, in Section 3.7 we offer conclusions and discuss implications for current and future satellite precipitation algorithms.

## **3.2 Data and Methods**

### *3.2.1 RAMS Simulations*

RAMS version 6.0 (Cotton et al. 2003) is a versatile model designed for simulating meteorological phenomena at the mesoscale and microscale. For our experiments, it was run on a 20km X 20km X 4km model domain with a horizontal resolution of 100 m and a vertical resolution of 50 m. The simulation was initialized horizontally homogeneously from a composite average atmospheric sounding from the Atlantic Trade Wind Experiment (ATEX) (Augstein et al. 1973, 1974; Brümmer et al. 1974) with a sea surface temperature of 298 K (Stevens et al. 2001). ATEX simulations have been used in the past to study warm phase cloud processes (eg., Stevens et al. 2001; Xue et al. 2008; Saleeby et al. 2015). Small near-surface potential temperature perturbations were applied to break the initial homogeneity. The simulation used

doubly periodic horizontal boundary conditions, a turbulent diffusion scheme (Smagorinsky 1963), the LEAF surface flux model (Walko et al. 2000), and the two-stream Harrington (1997) radiation scheme. The simulation was similar to those described in Saleeby et al. (2015), with the main difference being the increased horizontal and vertical resolution.

The RAMS simulation was performed using two-moment microphysics (Meyers et al. 1997; Saleeby and Cotton 2004; Saleeby and van den Heever 2013), with the model predicting mass mixing ratio and number concentration for each of the hydrometeor categories included in the model. Since the simulation lies entirely below the freezing level, the two relevant hydrometeor categories are cloud/drizzle droplets and rain drops. Each species is represented by a gamma distribution of the form

$$N(D) = \frac{N_t}{\Gamma(\nu)} \left(\frac{D}{D_n}\right)^{\nu-1} \frac{1}{D_n} \exp\left(-\frac{D}{D_n}\right). \quad (3.1)$$

$N(D)$  is the number concentration of particles of diameter  $D$ ,  $N_t$  is the total number concentration,  $D_n$  is the gamma distribution characteristic diameter, and  $\nu$  is the gamma distribution shape parameter.  $\nu$  is set equal to 4 for cloud droplets and 2 for rain drops. To calculate the rain rate, we assumed the relationship between drop size and fall speed parameterized by Atlas and Ulbrich (1974). This same method is used to calculate all rain rates considered in this study.

As examined in Chapter 2, it should be expected that this double moment microphysical model will not perfectly recreate the full range of DSD variability seen in warm rain, especially given the limited nature of the ATEX simulation in space and time. However, RAMS has proven successful at simulating a wide range of atmospheric phenomena in the past (e.g., Stevens et al. 2001; Jiang and Feingold 2006; van den Heever et al. 2006; Saleeby et al. 2009; Igel et al. 2013). Based on this track record, we believe the simulation can be trusted to give a general sense of

how much parameters like the rain rate (RR) and rain water content (RWC), which are targets of satellite retrievals, can realistically vary in the horizontal and vertical dimensions for shallow oceanic convection. Thus we used surface disdrometer data in Chapter 2 to study DSD-related retrieval uncertainties, and in this chapter utilize the very high resolution RAMS simulation to study the uncertainties introduced by spatial heterogeneity.

### *3.2.2 Simulation of Satellite Observations*

We simulate satellite observations for the same 3 architectures, coined A, B, and C, as in Chapter 2. For each satellite, the vertical resolution is assumed to be 250 m, similar to the resolution of GPM and CloudSat. We assume all of the instruments share the same footprint. This is not realistic but allows us to separate the effects of different measurement information content from resolution differences. We do investigate the result of changing the footprint size for each architecture in Section 3.3. The Satellite A measurements are assumed to come from a W-band (94 GHz) radar and include  $T_B$ , path integrated attenuation (PIA), and Z at each range gate. Satellite B measurements are made up of  $T_B$  at each of the 13 channels of the GPM Microwave Imager (GMI; Hou et al. 2014) and Z and PIA at Ku- and Ka-band (13.6 GHz and 35.5 GHz, respectively). Satellite C combines the W-band radar measurements of Satellite A with the Ku- and Ka-band measurements of Satellite B, with a heightened detection sensitivity. Refer back to Tables 2.1 and 2.2 to see the measurements simulated for each architecture and their assumed uncertainties and detection thresholds.

From the RAMS model output, synthetic observations are generated for each satellite architecture at 15-minute time steps across a total of 8 hours (after the model spin-up period). We use the MonoRTM radiative transfer model (Clough et al. 2005), the FASTEM6 sea surface emissivity model (Kazumori and English, 2015), and the QuickBeam radar simulator (Haynes et

al., 2007). We assume spherical hydrometeors and calculate their absorption and scattering properties using Mie theory (Mie 1908). See Chapter 2 for more details on the satellite simulation forward model.

### 3.2.3 Optimal Estimation

The simulated satellite observations are used as input to the optimal estimation (OE) retrieval algorithm that was developed in Chapter 2. Given  $\mathbf{y}$ , the measurement vector containing all of the observations ( $T_B$ , PIA, and  $Z$ ) for a given satellite architecture, the goal is to find the state vector  $\mathbf{x}$  that maximizes the conditional probability  $P(\mathbf{x}|\mathbf{y})$ :

$$P(\mathbf{x}|\mathbf{y}) = \frac{P(\mathbf{y}|\mathbf{x})P(\mathbf{x})}{P(\mathbf{y})}. \quad (3.2)$$

$\mathbf{x}$  consists of the vertically integrated cloud liquid water path (CLWP) and the vertical profile of the 2 DSD parameters: RWC and the mass weighted mean rain drop diameter,  $D_m$ . Chapter 2 we also retrieved the normalized gamma shape parameter  $\mu$ . It was found that this parameter was hard to retrieve accurately, but also that fixing  $\mu$  to a particular value did not have a large effect on retrieved rain rate errors, so in this study we set  $\mu = 1$  (this corresponds to the  $\nu = 2$ ) assumption in RAMS. Also in Chapter 2, we assumed that RWC and  $D_m$  were constant throughout the raining column. We maintain that assumption in Section 3.3, when we examine horizontal heterogeneity, but relax that assumption in other sections and retrieve a profile of RWC and/or  $D_m$ . CLWP, RWC, and  $D_m$  are all retrieved in logarithmic space instead of linear space because their distributions are closer to lognormal than to normal.

The OE framework also makes use of an a priori state vector,  $\mathbf{x}_a$ . If one assumes that a priori errors, measurement errors, and forward model errors are all Gaussian, then as Rodgers (2000) demonstrates, the optimal  $\mathbf{x}$  is found by minimizing the cost function  $\Phi$ :

$$\Phi = (\mathbf{x} - \mathbf{x}_a)^T \mathbf{S}_a^{-1} (\mathbf{x} - \mathbf{x}_a) + [\mathbf{y} - \mathbf{f}(\mathbf{x}, \mathbf{b})]^T \mathbf{S}_y^{-1} [\mathbf{y} - \mathbf{f}(\mathbf{x}, \mathbf{b})]. \quad (3.3)$$

Here  $\mathbf{f}(\mathbf{x}, \mathbf{b})$  represents the forward modeled measurements that are simulated by the retrieval algorithm using the state vector  $\mathbf{x}$  and ancillary information  $\mathbf{b}$  for comparison against the actual satellite measurements  $\mathbf{y}$ . The assumed errors in  $\mathbf{x}_a$ , and their covariances, are specified by the  $\mathbf{S}_a$  matrix, while the  $\mathbf{S}_y$  matrix describes the assumed errors in the matchup between the true observations and the forward modeled observations. The solution state is thus constrained both by the satellite observations and by the a priori assumptions, weighted by  $\mathbf{S}_a$  and  $\mathbf{S}_y$ . The Gauss-Newton method is used to solve for atmospheric state at which the gradient of the cost function,  $\nabla_{\mathbf{x}}\Phi$ , is equal to zero.

The OE forward model is built upon the same radiative transfer models (i.e., QuickBeam, MonoRTM, and FASTEM6) that are used to generate synthetic satellite observations. As noted in Chapter 2, this means that forward model errors will be less than should be expected in real life. We also assume that the elements of  $\mathbf{b}$  – the temperature and water vapor profiles, plus the sea surface temperature and wind speed – are known perfectly by the OE algorithm. These come directly from the RAMS model output (in Chapter 2 we show that there is only a modest impact to retrieval uncertainties when realistic ancillary assumption errors are taken into account). Still, there are some simplifications made in the forward model compared to the satellite simulator, which will contribute to the errors in  $\mathbf{S}_y$ . The most important of these simplifications is the handling of cloud water. Because satellites cannot easily detect cloud base, a constant cloud base of 500 m is assumed. The cloud water content is assumed to increase linearly up to 2000 m (for the Section 3.3 experiments) or to the level at which the W-band reflectivity crosses the -30 dBZ threshold (for Section 3.4-3.6 experiments). As in Chapter 2, we assume an inverse exponential

size distribution of cloud droplets with an average effective radius ( $r_e$ ) for the whole cloud of 11  $\mu\text{m}$ , consistent with the peak in  $r_e$  found at this value by Stubenrauch et al. (2013).

The assumed a priori state  $\mathbf{x}_a$  and its covariance matrix  $\mathbf{S}_a$  are based mostly upon the ARM ENA disdrometer data examined in Chapter 2. The ARM dataset was chosen instead of the OceanRAIN dataset because the precipitation measured by ARM comes mostly from warm shallow systems (Giangrande et al. 2019) of the same type being simulated by RAMS. In theory, the a priori assumptions could also be based on the RAMS statistics themselves but we avoid doing this so as not to bias the retrieval algorithm toward the correct answer. We take the mean values of RWC and  $D_m$  from the ARM dataset and use them as the a priori guesses for RWC and  $D_m$  in the OE algorithm. The a priori CLWP assumption is nominally set to 100  $\text{g/m}^2$ , because the disdrometer data alone cannot generate CLWP statistics. In testing, we varied this value from 50-200  $\text{g/m}^2$  without much of an effect on retrievals. The diagonal values of  $\mathbf{S}_a$  are made up of the variances of RWC and  $D_m$  found in the ARM data, with off-diagonal elements corresponding to the covariance between the two. We then multiply all of the ARM variances and covariances by 2, to crudely account for the additional uncertainty inherent in the fact that observational statistics from a single disdrometer are being used to retrieve modeled DSDs from a different setting. Table 3.1 lists the values of the  $\mathbf{x}_a$  state variables, along with their assumed variances.

The  $\mathbf{S}_y$  covariances come from a combination of two sources. Measurement uncertainties are generally well-known (see Tables 2.1 and 2.2), but forward model uncertainties are also included in  $\mathbf{S}_y$  and are both larger and harder to define. This is especially true for a study such as this one, where the forward model errors change from one experiment to another as different sources of errors are independently considered. For consistency's sake, we use the same  $\mathbf{S}_y$  matrix for each new experiment, at the risk of overestimating forward model uncertainties for

some of the more constrained experiments (the matrix does differ from one satellite architecture to another, because they include different instruments). The  $\mathbf{S}_y$  values are estimated by comparing the full resolution synthetic satellite observations for each architecture to simulated observations created based on the highly idealized representation of the cloud and rain profiles assumed in the OE forward model, in a manner similar to Duncan and Kummerow (2016).

Table 3.1 Values used in the a priori state vector  $\mathbf{x}_a$ , along with their assumed uncertainties included in the  $\mathbf{S}_a$  matrix.

State Variable	A priori Value	Std. Deviation $\sigma$ ( $\mathbf{S}_a$ uses $\sigma^2$ )	Comments
$\log_{10}(\text{CLWP})$	2.0 (100 g/m <sup>2</sup> )	0.25	Nominally chosen such that roughly 95% of RAMS profiles with surface RR > 0.1 mm/h are within 2 $\sigma$
$\log_{10}(\text{RWC})$	-1.43 (0.037 g/m <sup>3</sup> )	1.1	From ARM ENA disdrometer observations; the a priori value applies throughout the raining column, if applicable
$\log_{10}(\text{D}_m)$	-0.13 (0.74 mm)	0.45	From ARM ENA disdrometer observations; the a priori value applies throughout the raining column, if applicable

### 3.3 Uncertainties due to Nonuniform Beam Filling

In our first set of experiments, we examine specifically the retrieval uncertainties that arise due to horizontal sensor resolution. To create synthetic satellite observations, we take the rain DSD from the lowest 50-m level of the RAMS simulations and assume this DSD extends uniformly up to a height of 1 km. Then the CLWP is specified according to RAMS column, but the profile of cloud water is re-calculated so as to match perfectly with the assumptions of the OE algorithm; that is, linearly increasing from 500 m to 2 km, with a cloud drop effective radius,  $r_e$ , that increases from cloud base to cloud top and a total cloud-average  $r_e$  of 11  $\mu\text{m}$ . Figure 2.2 from the previous chapter illustrates the cloud and rain columns assumed. We could of course use the exact profiles of cloud and rain DSDs from RAMS to simulate satellite observations (and we do this in later sections), but for this first case we focus on the same idealized retrieval

framework that was used in Chapter 2. We do this to make comparisons to Chapter 2 easier and in order to isolate NUBF errors that have strictly to do with horizontal sensor resolution instead of vertical structure or forward model representation errors.

### *3.3.1 Base Case Uncertainties*

As a baseline measure of retrieval uncertainties, and for comparison to Chapter 2, we first simulate satellite observations at the native 100-m horizontal resolution of RAMS. Sensor noise is added, and Z values that fall below detection thresholds eliminated, according to Tables 2.1 and 2.2. Then we use the OE algorithm to attempt to retrieve back the CLWP, RWC, and  $D_m$  for each RAMS profile from each satellite architecture. Because the forward model of the OE should in theory be able to perfectly recreate the cloud and rain profiles used to make the synthetic observations, all retrieval errors must come from one of three sources: sensor noise, fundamental nonlinearities, or insufficient information content in the satellite measurements. Fundamental nonlinearities in the retrieval problem could cause the algorithm to converge to a local minimum of  $\Phi$  instead of the absolute minimum, while insufficient information content (for example the inability of the radars to detect small drops with reflectivities below their respective thresholds) will lead the algorithm to converge towards a priori assumptions.

Figure 3.1 plots the baseline pixel uncertainties in retrieved CLWP, RWP, RR, and  $D_m$  for Satellite C, the most capable of the satellite architectures considered. The uncertainties are generally similar to what was seen for the base case in Chapter 2, when the underlying DSDs came from disdrometer observations instead of a model. However, the spread in results is a bit larger, and for the lightest rain rates there is a tendency to overestimate CLWP while underestimating RWP (i.e., substitute cloud water for rain water). This leads to a small underestimation of RR. This tendency is due to the influence of a priori assumptions about

CLWP and  $D_m$ . Overall (in terms of medians), retrieved CLWP is biased high by 10.8%, RWP biased low by 13.7%, RR biased low by 9.1%, and  $D_m$  biased high by 5.4%. The interquartile range (IQR) for retrieval errors for each of these parameters is between 11-24%.

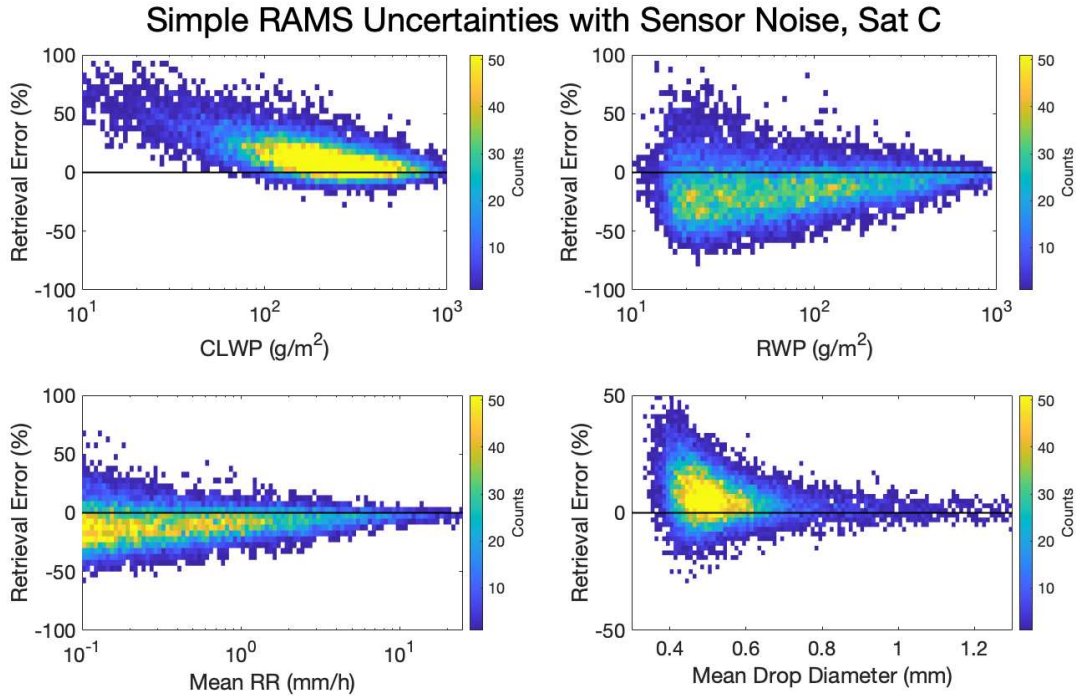


FIG. 3.1. Density plots of retrieved error in CLWP, RWP, column-averaged RR, and column-averaged  $D_m$  compared to the true value that was used to make the underlying simulated satellite observations, for Satellite Architecture C. This experiment considers only sensor noise and detection limits as sources of uncertainty.

The other two satellite architectures have larger retrieval errors (their IQRs can be seen in Figure 3.2). The behavior of Satellite A is similar to Satellite C, with CLWP and  $D_m$  biased high while RWP and RR are biased low. The biases are slightly larger in magnitude than for Satellite C, and the spread in retrieval errors is also larger. Satellite B has a distribution of retrieval errors that is unlike the other two architectures. In addition to having a much larger spread of errors, retrieved CLWP and  $D_m$  are biased low while RWP and RR are biased quite high (40.3% and 34.1%, respectively). This is due in part to the fact that many of the RAMS DSDs do not generate Ku- or Ka- band Z that are above the 12 dBZ reflectivity threshold of the satellite. In

fact, only 56% of pixels generate valid Satellite B radar reflectivities. In the remainder of cases, Satellite B has only PMW observations available to it and struggles to distinguish between cloud water and rain water. The fact that it has a tendency to choose rain water over cloud water is probably explained by the fact that CLWP has slightly tighter a priori bounds, so the retrieval is more likely to increase rain water than cloud water in response to a  $T_B$  signal of water in the column. For the subset of pixels for which Satellite B does have valid  $Z$ , the retrieved RR is still biased high but at a more modest 22.8%.

### *3.3.2 Effects of Sensor Footprint Size*

Next we ran a series of experiments designed to quantify how changing the sensor footprint size changes retrieval uncertainty. The 100-m horizontal resolution maps of  $T_B$ , PIA, and  $Z$  from the base case were averaged together using a boxcar filter at new resolutions of 500 m, 1 km, 2 km, and 5 km. These new synthetic satellite observations were run through the OE algorithm, and the retrieved CLWP, RWP, and RR compared to corresponding values from RAMS at each resolution. Figure 3.2 shows that there is a clear trend towards a greater underestimation of RWP and RR at lower horizontal sensor resolution. Putting this in the context of previous studies such as Durden et al. (1998), this result suggests that for all 3 satellite architectures the NUBF effects on radar attenuation and  $T_B$ , which act to cause underestimation of rainfall, outweigh the slightly positive NUBF effect on unattenuated  $Z$ . The effect is largest for Satellite B, which makes sense given that for many of the pixels it is operating in PMW-only mode because the  $Z$  are below its detection limit. Compared to averaging retrieved RRs from the native resolution retrieval, at 5-km resolution (roughly the resolution of GPM DPR), retrieved RRs from Satellite B are about 50% lower, while Satellites A and C are about 40% lower. At 500-m resolution (equal to the sampling spacing planned for the upcoming EarthCARE satellite;

Illingworth et al. 2015), the NUBF effect is much smaller. Retrieved RRs are biased 7% lower than native resolution for architectures B and C but only about 1% lower than native resolution for Satellite A. The horizontal NUBF effect does not seem to have a large effect on the overall spread of retrieval errors; if anything, the IQR of retrieval error actually tends to shrink as the footprint grows larger. This is likely due to the fact that averaging reduces variability.

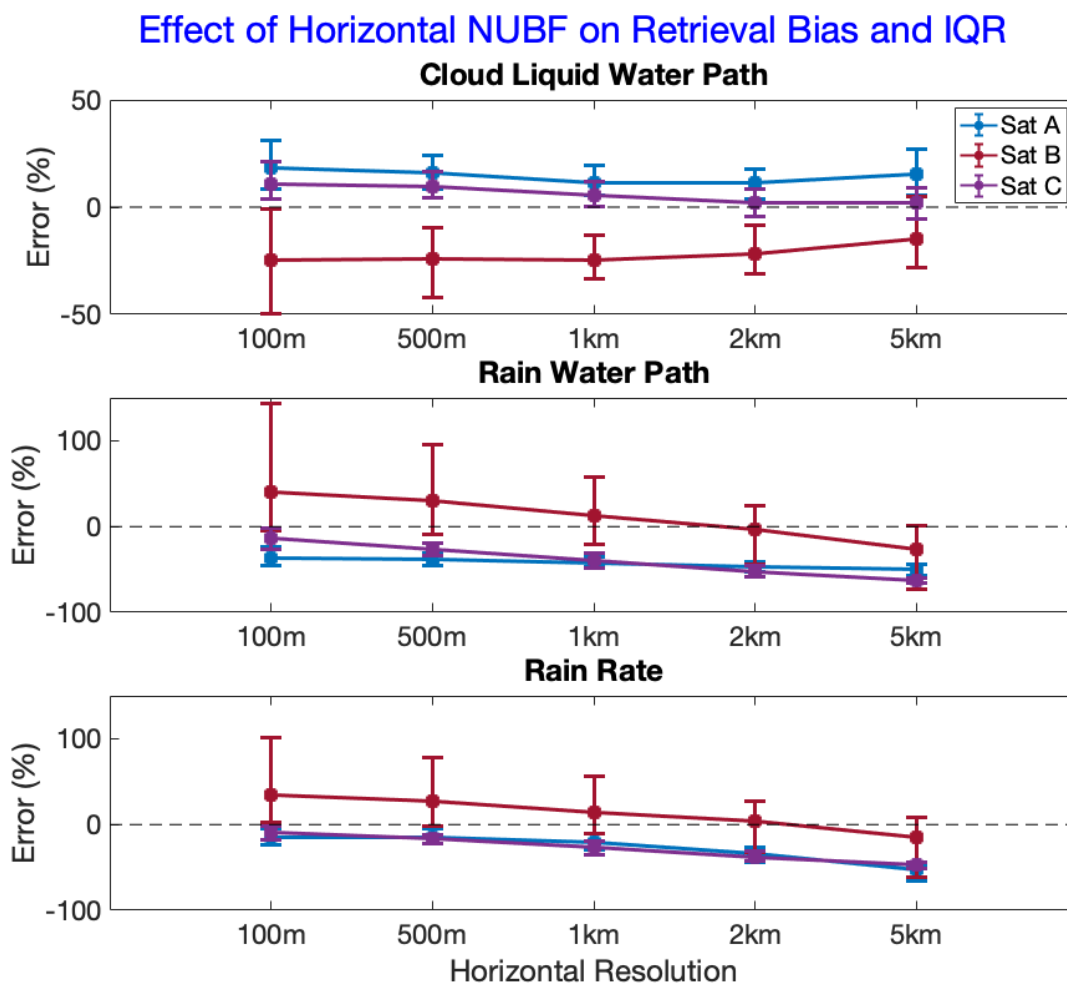


FIG. 3.2. Retrieval errors as a function of horizontal resolution, for each satellite architecture. The bars show the interquartile range of the pixel-level retrieval error in either CLWP (top), RWP (middle), or RR (bottom). The satellite is indicated by the color of the lines and markers.

### 3.4 Uncertainties due to Vertical Variability

#### 3.4.1 Assumptions About Vertical Structure

In the next set of experiments, actual hydrometeor profiles from RAMS were used to simulate satellite observations, instead of assuming the simplified vertical structure of Chapter 2 and Section 3.3. To isolate the effect of assumptions about vertical structure, without the effect of NUBF, we first used RAMS profiles at their native horizontal resolution. All pixels with a surface RR greater than or equal to 0.1 mm/h were included (over 10,000 pixels total), and the columns were sampled every 250 m in the vertical to match the vertical resolution of the satellite radars. As before, random measurement noise was added to the simulated measurements before trying to retrieve back the true CLWP, RWP, and profiles of RR and  $D_m$  using each satellite architecture.

First, we let the retrieval algorithm assume the same simplistic scenario assumed in Section 3.3; that is, a uniform raining column. The column was assumed to extend from the surface up to the point at which the W-band reflectivity first exceeded -10 dBZ (even for Satellite B, which does not actually include a W-band radar). The OE algorithm then retrieved a single RWC and a single  $D_m$  value for the entire column (in other words, the column average). As can be seen in Figure 3.3, these assumptions led to a retrieval algorithm that performed quite poorly for all satellite architectures. All of the retrieved values tracked in the figure were strongly negatively biased (with the one exception of CLWP for Satellite C), and the variability was also large. On the other hand, we also tested a version of the retrieval algorithm that attempted to retrieve RWC and  $D_m$  at every level of the raining column. This version performed slightly better; however, estimates of the surface RR were biased low by between 35-45% for all 3 satellites, and the IQR of retrieval errors was still rather large. This result indicates that assuming

a more complex vertical structure isn't always wise. If there is not enough independent information in the measurements to constrain what one is trying to retrieve (as appears to be the case here, even for Satellite C), the ill-posed nature of the inversion problem will lead to sub-optimal results. One possible approach to reduce errors due to vertical variability would be to add correlations between vertical levels to the  $S_a$  covariance matrix.

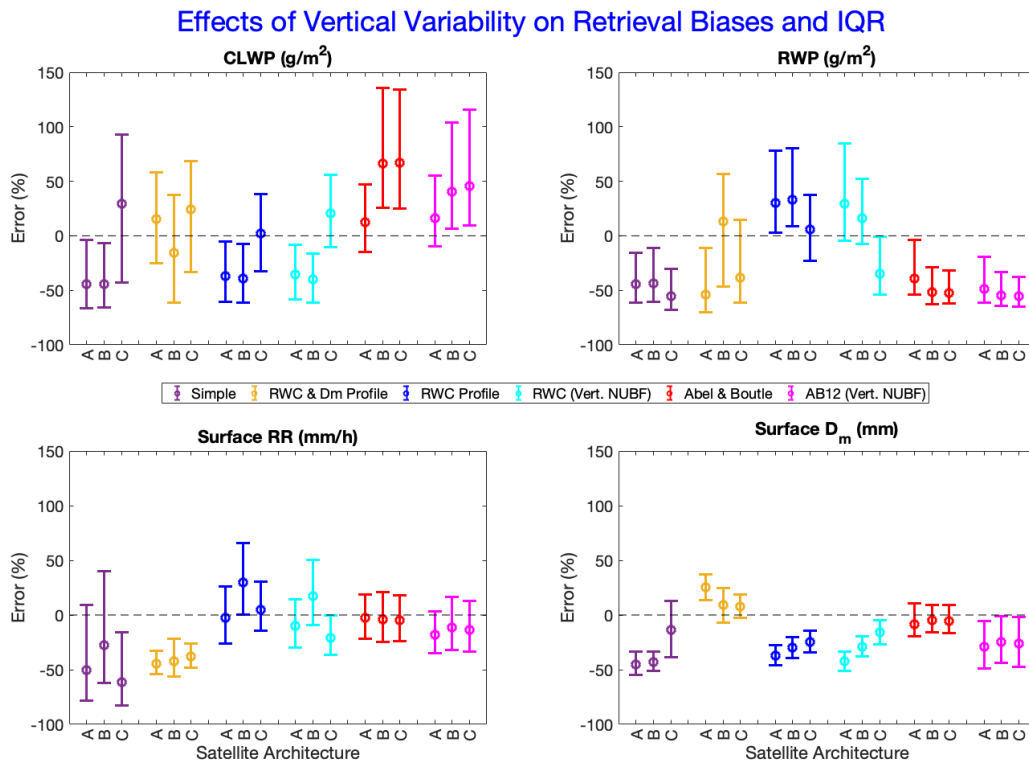


FIG. 3.3. Each bar shows the IQR in either CLWP, RWP, surface RR, or surface  $D_m$ , for a given experiment and satellite architecture. The satellite is indicated by the letter on the x-axis. The experiment being considered is indicated by the color of the bars. In the purple experiment only a column-average RWC and  $D_m$  are retrieved, while in the gold experiment RWC and  $D_m$  are retrieved at each valid radar range gate. Blue and red show the results when a profile of RWC is retrieved and  $D_m$  is either retrieved as a column average (blue) or prescribed according to Abel and Boutle 2012 (red). The cyan and magenta experiments use the same retrieval setup as blue and red (respectively) but are run on synthetic satellite observations that account for vertical nonuniform beam filling.

Next we conducted two experiments in which a full profile of RWC was retrieved, but  $D_m$  was constrained. In the first (blue lines in Figure 3.3), as compromise between the two experiments above,  $D_m$  was retrieved as a single column-averaged value. For the triple-frequency Satellite C, this led to good results, with the bias in retrieved CLWP, RWP, and surface RR all being close to zero. For the other two satellites, there was a tendency to overestimate rain water at the expense of cloud water. All three satellites tended to underestimate the surface  $D_m$ , which makes sense given that  $D_m$  at the surface is usually larger than the column average. In the other experiment (red lines in Figure 3.3), the RWC profile was retrieved and the profile of  $D_m$  calculated based on the AB12 relationship. For the surface RR metric, this set of experiments had the lowest biases and IQR values. However, the retrieval had a tendency to substitute cloud water for rain water higher up in the column. An examination of the RAMS profiles revealed that the AB12 RWC- $D_m$  relationship was especially inappropriate for the RAMS profiles at these heights. In Figure 3.5, for instance, it can be seen that RWC tends to be higher at 1000 m than at the surface, while  $D_m$  tends to be much lower, contradicting the AB12 RWC- $D_m$  relationship.

### 3.4.2 Vertical NUBF

For the same reasons that horizontal inhomogeneity can lead to biases in radar retrievals of rain, vertical inhomogeneity also increases retrieval uncertainty (it is much less of a concern for observables that lack vertical resolution, like  $T_B$  or PIA). To quantify the effect of vertical NUBF, we repeated the exercise of Section 3.4.1 but, instead of sampling the RAMS profiles at every 250 m, we simulated radar reflectivities at the 50-m resolution of the RAMS model and then averaged the Z to the 250-m resolution of the radars. We performed retrievals using either the variable RWC / constant  $D_m$  approach or assuming the AB12 RWC- $D_m$  relation. These two methods were chosen because they gave the smallest biases in retrieved values of the four

methods tested in Section 3.4.1. The error distributions from these experiments are also shown in Figure 3.3 (in the cyan and magenta). Including vertical NUBF effects had the tendency to reduce retrieved RWP and RR across all satellite architectures, with Satellites B and C affected a little bit more strongly. These patterns are consistent with the effects of horizontal NUBF that were seen in Section 3.3.

### **3.5 Uncertainties due to Surface Clutter**

The experiments of Section 3.4.1 were repeated, except that radar observations from the lowest levels of the column were omitted. The simulated surface clutter extended up to either 500 m, 1 km, or 1500 m. For the purposes of calculating  $T_B$  and PIA, the OE algorithm assumed that the profiles of RWC and  $D_m$  were constant from the lowest observable radar range bin down to the surface. We ran two sets of experiments, either with a constant  $D_m$  assumed throughout the column (but RWC retrieved as a profile above the surface clutter), or with the AB12 RWC- $D_m$  relation. The IQR of the retrieved RR error at the top of the surface clutter, for each surface clutter height, is plotted in Figure 3.4. While the spread in retrieval uncertainty does not necessarily increase as the surface clutter depth increases, there is a tendency for the RR to be underestimated above the surface. At 1 km in height, the retrieved RR is biased low by between 20 and 50%. The underestimation effect is slightly lower for Satellite A.

Of course, even if a RR retrieval is unbiased at 1 km above the surface, retrieval of the surface RR will be subject to additional uncertainties because the RR can change between the surface and the top of the surface clutter. This could be due to evaporation, collision/coalescence, or both. Retrieval algorithms may or may not try to model these processes to give a more

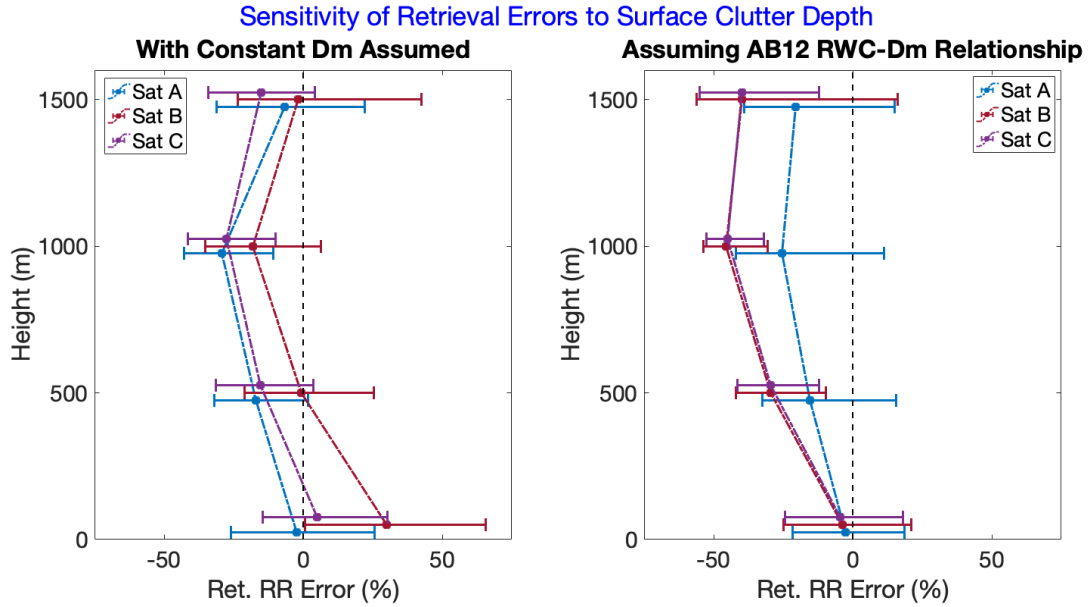


FIG. 3.4. Median and IQR of retrieved RR error, if surface clutter is assumed to extend up to various heights. The different satellite architectures are represented by the different colors. The heights considered are 0 m, 500 m, 1 km, and 1500 m for all architectures; the error bars are slightly offset from these heights to make the differences between the satellites easier to see. The experiments on the left were run with the OE algorithm assuming a constant  $D_m$  profile, while the experiments on the right prescribed a RWC- $D_m$  relationship according to Abel and Boutle (2012).

accurate surface rain rate, but even if they do their microphysical models will not perfectly represent reality. Rather than test specific microphysical models (since the microphysical models used by RAMS are already known), we examine the difference between the rain characteristics in RAMS at each of these heights compared to the rain characteristics at the surface, in order to give a worst-case scenario of the types of the errors that could be expected in a warm rain retrieval algorithm due to surface clutter.

Figure 3.5 panels a-c show the RAMS distributions of RWC,  $D_m$ , and RR at the surface, 500 m, 1 km, and 1.5 km. RWC and RR tends to be highest at 1 km, probably due to evaporation that occurs below this level. The distribution of  $D_m$ , on the other hand, broadens and shifts towards higher values as one approaches the surface. As seen in panel d, most pixels

feature a small difference in RR between the top of the surface clutter and the surface, but there is a long positive tail. About 30% of profiles have a difference between the 1-km RR and the surface RR that is larger than 0.2 mm/h.

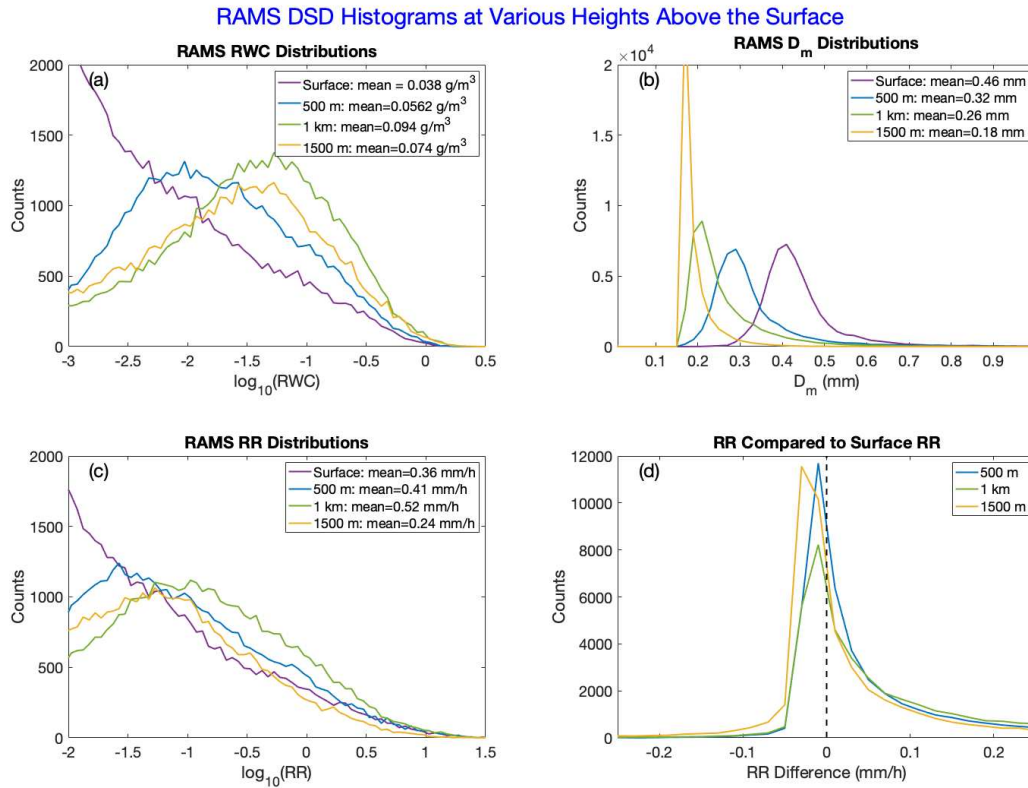


FIG. 3.5. Histograms of various DSD characteristics from the RAMS simulations, colored by height. (a) Rain water content (b) Mass weighted mean diameter (c) Rain rate (d) Difference between RR at a given height and the RR at the surface underneath.

### 3.6 Combined Uncertainties for an AOS-like Satellite

In our last experiment, we performed retrievals combining all of the sources of uncertainty previously considered: sensor noise and detection thresholds, nonuniform beam filling, algorithm assumptions about the cloud and rain structure, and surface clutter. We simulated observations for an AOS-like satellite based on the “minimum desired capabilities”

specified in Revision E of NASA’s Science and Applications Traceability Matrix (SATM) for the AOS mission (available at [https://science.nasa.gov/science-pink/s3fs-public/atoms/files/ACCP\\_SATM\\_Rel\\_E\\_TAGGED.pdf](https://science.nasa.gov/science-pink/s3fs-public/atoms/files/ACCP_SATM_Rel_E_TAGGED.pdf)). The SATM specifies W-band (Ka-band) radar observations with a minimum detectable radar reflectivity of -25 dBZ (5 dBZ), horizontal resolution of 2 km, vertical resolution of 250 m, and measurements extending down to 500 m. Note that these Z thresholds are slightly higher than the ones used for Satellite C in previous experiments, and that the satellite lacks a Ku-band radar (lower thresholds and a Ku-band are included under “desired enhanced capabilities” in the SATM).

Synthetic observations were first generated at the native resolution of RAMS, and then averaged to the horizontal and vertical resolutions of the AOS-like satellite. Radar observations below 500 m were eliminated. CLWP and the RWC profile were retrieved for each 2-km by 2-km synthetic satellite pixel (sampled from the RAMS grid at every 500 m) using the AB12 DSD assumptions. Figure 3.6 shows the surface RR from RAMS (at 2-km resolution), plotted against the RR at 500 m retrieved by the OE algorithm, which is assumed to be the same as the surface RR. There is a tendency to underestimate the RR, especially for heavier precipitation, which is perhaps to be expected given the effects of NUBF. The overall negative bias is -18.6%, with an IQR of 55.4% that is considerably larger than the base-case IQR for Satellite C of 15.7% calculated in Section 3.3 and seen in Fig. 3.1. The SATM also specifies a desired uncertainty for the precipitation rate profile of 100%. Taking this to mean a 100% positive bias or a 50% negative bias, relative to RAMS, 81.4% of synthetic AOS-like retrievals fall within these bounds. The desired uncertainty range is shown by the dashed red lines in Figure 3.6.

We tested adding a Ku-band radar with a minimum detectable reflectivity of 10 dBZ to the theoretical AOS satellite (not shown), but there was little improvement in retrieved RR. This

suggests that there is not much extra information in the Ku-band if one already has the Ka-band, at least for the very light rain considered in this study.

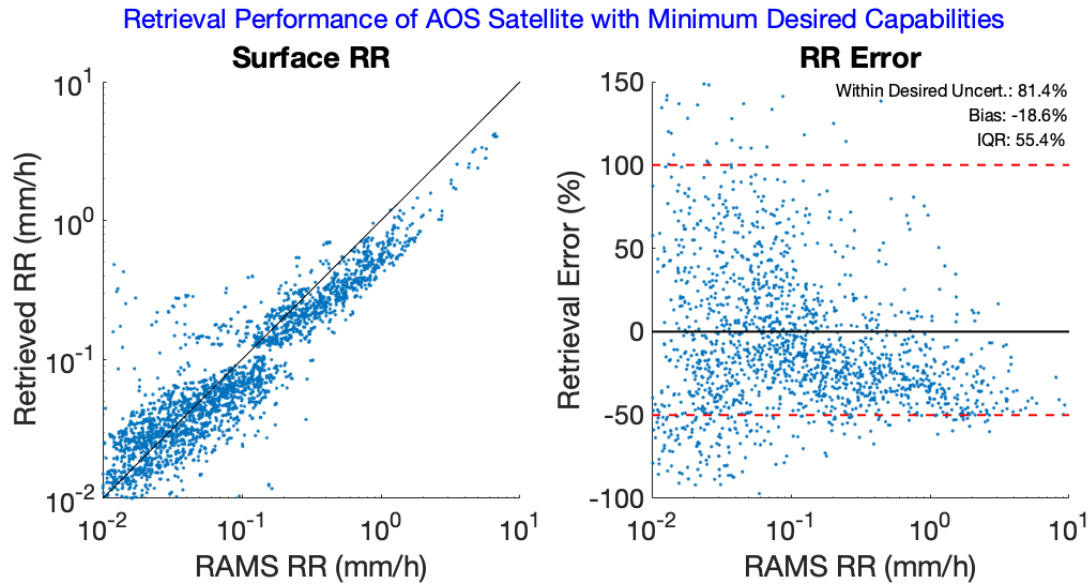


FIG. 3.6. RAMS surface RR, at 2-km resolution, plotted against retrieved RR (left) or retrieved RR percentage error (right) from an AOS-like satellite as described in the text. The red dashed lines represent the desired uncertainty limits specified in NASA Science and Applications Traceability Matrix (SATM).

### 3.7 Discussion and Conclusions

Our analysis reiterates previous findings that NUBF is an important source of error in satellite precipitation estimates. We found that, even for shallow warm rain, NUBF effects led to a 40-50% negative bias in retrieved RR at the coarsest resolution tested (5 km). One possible explanation is that, at the very light RRs of the RAMS simulation, Ku- and Ka- band reflectivities do not exceed detection thresholds, but W-band Z still experience attenuation. The result is that  $T_B$  and attenuation affects dominate the NUBF response and underestimation of rain occurs. Retrieval biases were much more modest (less than 10%) at 500-m horizontal resolution. This seems like a good if ambitious target for future satellite radars, particularly those operating at higher frequencies for which smaller footprints are more feasible.

Vertical NUBF errors were found to be smaller, though they still tended to lead to the underestimation of RR. More important when it comes to vertical inhomogeneities are the assumptions made about the profile of rain water. Assuming a uniform profile of rain led to severe negative biases; however, trying to retrieve both RWC and  $D_m$  at each level also led to poor retrieval performance due to insufficient information content. The optimal solution seems to land somewhere in the middle; i.e., retrieving a profile of RWC but making simplifying assumptions about the profile of  $D_m$ .

When it comes to surface clutter, we found that, for this RAMS simulation at least, RRs tend to be lower at the surface than slightly above the surface, at 500-1000 m. This is due to evaporation below cloud base. The surface RR was at least 0.2 mm/h lower than the rain rate above in about 30% of cases, meaning that surface clutter could potentially cause significant biases for light rain if one's target variable is surface rain intensity or frequency. This finding is consistent with prior studies (e.g., Rapp et al. 2013). We also found, however, that our retrieval tended to underestimate the RR at the top of the surface clutter, a partially compensating error. It is not immediately clear whether other precipitation retrieval algorithms should be expected to be subject to this sort of effect.

Putting it all together, we tested the performance of an AOS-like satellite using NASA's minimum desired capabilities and found that the combined uncertainty would be sufficiently low to make the theoretical instrument useful for advancing the study of warm rain. The retrieval error fell within the desired uncertainty range over 80% of the time. Still, retrieved RR was biased low by almost 20% with a large spread in retrieval errors, particularly at the lightest RRs. The overall negative bias should probably not be a surprise, since even in the baseline (Section 3.3) there was a bias, and because most of the individual sources of uncertainty that we studied

individually tended to reduce the retrieved RR. In practice, this bias could hopefully be greatly reduced. While it is beyond the scope of this study, a NUBF correction model such as that proposed by Short et al. (2015) would improve retrieval accuracy. It would be important to train such a model using a globally representative collection of statistics, rather than just a single case study. The effects of surface clutter can be mitigated either by radar technological advances that reduce surface interference, incorporating better evaporation models, or both. Retrieval performance could also likely be improved by making more careful assumptions about the cloud drops in the column.

In contrast to the simulations from Chapter 2, in which assuming the AB12 DSD relationship led to large positive biases in retrieved RR, in this study we found that this assumption performed reasonably well. This could be due to the fact that this study was based on modeled rain drops, whereas Chapter 2 was based on actually measured drops that tended to be larger. Another possible explanation is that the positive AB12 bias found in Chapter 2 was counteracted by the large negative bias of NUBF, leading to decent performance overall. More work is needed to determine whether the RWC- $D_m$  relationship from AB12 is actually appropriate for warm rain.

This leads to a larger point, which is that the results from this study should not be taken to definitely characterize the errors that affect any current or future precipitation-measuring satellite. We've made several simplifying assumptions, and a thorough error analysis would rely on additional model simulations from varying meteorological regimes. Still, we believe that by examining the *relative* impact of different types of uncertainties on three different satellite architectures, we can better understand why current satellite precipitation estimates disagree, and better plan for future missions.

## CHAPTER 4: CAN DSD ASSUMPTIONS EXPLAIN THE DIFFERENCES IN SATELLITE ESTIMATES OF WARM RAIN?

### 4.1 Introduction

Satellites play an important role in measuring, predicting, and understanding precipitation across the globe. Current precipitation missions such as the Global Precipitation Measurement (GPM) mission (Hou et al. 2014; Skofronick-Jackson et al. 2017) and CloudSat (Stephens et al. 2002) are crucial for monitoring the global hydrologic cycle and constraining climate models, especially over the open oceans where rain gauges, disdrometers, and ground-based radar observations are rarely available. Satellite observations inform many types of precipitation estimates. These include direct estimates from CloudSat (Haynes et al. 2008; Lebsock and L'Ecuyer 2011) and GPM (Greco et al. 2016; Seto et al. 2021) along with the earlier Tropical Rainfall Measuring Mission (TRMM; Kummerow et al. 2000), estimates from a constellation of passive microwave radiometers (GPROF; Kummerow et al. 2015), and estimates that combine observations from a variety of different satellite techniques such as the Global Precipitation Climatology Project (GPCP; Alder et al. 2018) and the Climate Prediction Center Merged Analysis of Precipitation (CMAP; Xie and Arkin 1997). Over some regions of the globe, there is reasonable agreement between seasonally averaged precipitation as estimated from these various satellite products, especially when GPM-based and CloudSat-based estimates are combined in ways that take advantage of the fact that GPM/TRMM is more sensitive to moderate and heavy precipitation while CloudSat is more sensitive to light precipitation (Behrangi et al. 2014, Hayden and Liu 2018). However, over the higher latitudes, as well as over stratocumulus dominated regimes, larger discrepancies exist (Berg et al. 2010; Andersson et al. 2011; Behrangi

et al. 2016; Behrangi and Song 2020). In particular, north or south of about 40 degrees in latitude there are large differences between zonally averaged oceanic precipitation estimates from the GPM combined radar/radiometer algorithm GPM\_2BCMB (Greco et al. 2016) and the CloudSat 2C-RAIN-PROFILE algorithm (Lebsock and L'Ecuyer 2011). Behrangi and Song (2020) find that the GPM estimates can be up to 60-70% (~2 mm/d) lower than the CloudSat estimates at these high latitudes.

There are undoubtedly many factors contributing to the disagreement among satellite precipitation estimates. For example, many light precipitation events do not generate high enough Ku- or Ka-band reflectivities ( $Z$ ) to be detected by the Dual-frequency Precipitation Radar (DPR) on the GPM Core Satellite. DPR has a minimum detectable  $Z$  of 15.46 dBZ for Ku-band, 19.18 dBZ for Ka-band matched beam, and 13.71 dBZ for the Ka-band high sensitivity beam (Masaki et al. 2021). In terms of rain rates, this corresponds to a nominal threshold of 0.5 mm/h for Ku-only retrievals and 0.2 mm/h for Ku/Ka retrievals (Kidd et al. 2021). However, Lin and Hou (2012) found that, over the continental United States, 43.1% of precipitation occurs below 0.5 mm/h and 11.3 % occurs below 0.2 mm/h, with those occurrences accounting for 7% and 0.8% of total rain volume, respectively. Over stratocumulus areas and at the high latitudes, where drizzle is common, those values are even higher, with as much as 70% of precipitation by frequency (or around 25% by volume) occurring at rain rates below 0.5 mm/h (Kidd et al. 2007; Giangrande et al. 2019). CloudSat's Cloud Profiling Radar (CPR), on the other hand, struggles with heavy precipitation. The higher frequency W-band radar is more easily attenuated by water vapor, cloud water, and rain water, and multiple scattering is also more of a concern. These factors make CPR precipitation estimates at high rain rates unreliable (e.g. Battaglia et al. 2008, Berg et al. 2010). The insensitivity of DPR to light precipitation and the attenuation challenges

CPR faces in heavy precipitation together form a natural (if only partial) explanation of the widely reported result that GPM/TRMM retrievals underestimate light rain rates while CloudSat retrievals underestimate heavy rain rates (e.g. Berg et al. 2010, Behrangi et al. 2012, Hayden and Liu 2018).

Another important consideration is surface clutter. DPR radar returns below about 1000m above the surface have too much noise to accurately detect precipitation, rising to up to 1500m near the edge of swath or over rough terrain (Kidd et al. 2021). For CloudSat, the lowest range bin that can be accurately sensed is around 750m (Tanelli et al. 2008). Thus, each of these radars misses some shallow precipitation altogether. For example, Kidd et al. (2021) found that only slightly more than 60% of radar profiles over the United Kingdom had rain rates greater than 0.2 mm/h at 1000m above the surface. Even when the radar can detect the presence of precipitation, assumptions must be made to translate the near-surface precipitation rate to the actual precipitation rate at the surface. In some cases, collision-coalescence processes act to enhance the surface rain rate (Porcaccia et al. 2019), while in drier environments all of the rain detected at 750m might evaporate before it hits the ground (Rapp et al. 2013).

With different sensitivities to light, near-surface, and frozen (or mixed phase) precipitation, it is not surprising that there is some discrepancy between GPM and CloudSat estimates of precipitation. Still, there are many other factors, such as algorithm assumptions, that could be contributing to the underestimation of high latitude precipitation by GPM compared to CloudSat. In this chapter we focus on one potential source of uncertainty, the drop size distribution (DSD) model assumed by retrieval algorithms, and one particular type of precipitation, warm rain. We make use of the CloudSat-GPM coincidence dataset (Turk et al. 2021) and, using a consistent optimal estimation (OE) framework (thus eliminating many

potential sources of discrepancy), we retrieve warm rainfall rates from the CloudSat and GPM observations separately. As expected, the GPM retrievals return less overall rain than the CloudSat retrievals, but we find that most of the difference disappears when we account for surface clutter, radar detection thresholds, and DSD assumptions. We also perform combined retrievals that incorporate observations from both GPM and CloudSat. These experiments strengthen the argument that DSD assumptions account for part of the GPM/CloudSat rain warm discrepancy and offer insight into the kind of retrievals that may be possible with future satellite radars.

## **4.2 Data**

The CloudSat-GPM coincidence dataset, version 1C (Turk et al. 2021), is a compilation of products for each near-coincident (within 15 minutes) overpass between CloudSat and GPM from March 18, 2014 to September 30, 2016. This time period covers 6502 instances when the two satellites, due to their unique orbital geometries, sampled the same scene. Each CPR pixel is matched to the pixel contained in the DPR swath whose center is closest in space to the center of the CPR pixel. Because the instruments' footprints are not the same size, this means that many of the GPM observations are associated with multiple CloudSat pixels. There is also a slight mismatch in vertical resolution for the radars: the DPR vertical resolution is 250 m for matched Ku- and Ka-band footprints, while the CPR vertical resolution is 240 m. When matching radar bins between CPR and DPR, the matched DPR bin is the bin whose top lies just above a given CloudSat bin top.

Each CloudSat-GPM coincident file contains several individual datasets. GPM products are Version 4 (V4) and CloudSat products are Release-5 (R05). We use the CPR profile of radar

reflectivity as reported in the 2B-GEOPROF dataset, along with an estimate of two-way 94 GHz path integrated attenuation (PIA) due to hydrometeors, which comes from 2C-PRECIP-COLUMN (Haynes et al. 2009). For GPM, we use the “matched scan” (MS) profiles of Ku- and Ka-band reflectivity, along with corresponding PIA values, from 2B.GPM.DPRGMI.CORRA (Greco et al. 2016), while GPM Microwave Imager (GMI) brightness temperatures come from 1C.GPM.GMI. Auxiliary information used by our retrieval, including the surface wind speed and profiles of temperature, pressure, and specific humidity, comes from ECMWF-AUX, i.e., interpolated forecast model fields from the European Center for Medium Range Weather Forecasts.

We compare retrieved rain rates from our algorithm with retrieved rain rates reported from the GPM\_2BCMB radar/radiometer algorithm (Greco et al. 2016) and the CloudSat 2C-RAIN-PROFILE algorithm (Lebsock and L’Ecuyer 2011). These values also come from the CloudSat-GPM coincidence files (and thus are V4 and R05, respectively). In our analysis, we consider CloudSat rain rates at two levels: at the surface and at CPR range bin 5, which we will refer to as GPM-base because it corresponds approximately to the lowest DPR range bin (~1000m above the surface). The surface values are taken directly from the CloudSat-GPM coincidence files. The CloudSat algorithm assumes that evaporation occurs between cloud base and the surface according to the parameterization given in Kalmus and Lebsock (2017). For a better apples-to-apples comparison with the GPM combined algorithm, which does not include sub-cloud evaporation, we also consider GPM-base rain rates from 2C-RAIN-PROFILE. While these are not reported directly in the CloudSat-GPM coincidence files, the rain water content (RWC) retrieved at each range bin is reported, and from this we calculate the rain rate assuming

the DSD parameterization given by Abel and Boutle (2012), which is the same parameterization assumed by the 2C-RAIN-PROFILE algorithm.

### 4.3 Methods

To retrieve rain rates from the GPM and CloudSat measurements, we use a retrieval algorithm based upon the method of optimal estimation (Rodgers 2000). Simpler versions of the algorithm meant for non-precipitating scenes are described in Duncan and Kummerow (2016) and Schulte et al. (2020). While the mathematical backbone of the algorithm used in this study is the same as in those, the current algorithm has several key differences. While earlier versions were designed to be used only with passive microwave (PMW) brightness temperature ( $T_B$ ) observations, the version described here also incorporates (and indeed emphasizes)  $Z$  as well as PIA estimates. As in the earlier studies, we retrieve the cloud liquid water path (CLWP), but rather than trying to retrieve the water vapor profile, we use the profile from ECMWF as given in the CloudSat-GPM coincidence files and instead retrieve the rain water content (RWC) at each radar range gate.

Like other OE algorithms, ours is a Bayesian algorithm that searches for the atmospheric state vector ( $\mathbf{x}$ ) that, when processed through a forward model  $\mathbf{f}$  along with assumed ancillary information (represented by the vector  $\mathbf{b}$ ), leads to simulated observations that are most consistent with the actual satellite observations  $\mathbf{y}$ , subject to measurement and forward model uncertainties described by the error covariance matrix  $\mathbf{S}_y$ . At the same time,  $\mathbf{x}$  is constrained by the *a priori* state vector,  $\mathbf{x}_a$ , and its assumed uncertainties, described by the error covariance matrix  $\mathbf{S}_a$ . The algorithm tries to find the state vector that maximizes the conditional probability

$P(\mathbf{x}|\mathbf{y})$ , that is, the probability of that state being the correct state given the observed satellite measurements, which by Bayes' Theorem is given by

$$P(\mathbf{x}|\mathbf{y}) = \frac{P(\mathbf{y}|\mathbf{x})P(\mathbf{x})}{P(\mathbf{y})}. \quad (4.1)$$

Rodgers (2000) showed that, if one assumes Gaussian measurement errors, Gaussian forward model errors, and Gaussian errors in  $\mathbf{x}_a$ , maximizing  $P(\mathbf{x}|\mathbf{y})$  amounts to minimizing the cost function  $\Phi$ , given by

$$\Phi = (\mathbf{x} - \mathbf{x}_a)^T \mathbf{S}_a^{-1} (\mathbf{x} - \mathbf{x}_a) + [\mathbf{y} - \mathbf{f}(\mathbf{x}, \mathbf{b})]^T \mathbf{S}_y^{-1} [\mathbf{y} - \mathbf{f}(\mathbf{x}, \mathbf{b})]. \quad (4.2)$$

The first term will be smaller the closer a potential solution vector  $\mathbf{x}$  is to the assumed a priori state  $\mathbf{x}_a$ , while the second term will be smaller the closer the forward model output  $\mathbf{f}(\mathbf{x}, \mathbf{b})$  is to the actual satellite measurements. We use the Gauss-Newton method to iteratively solve for the value of  $\mathbf{x}$  at which the gradient of the cost function,  $\nabla_{\mathbf{x}}\Phi$ , is equal to zero. In our case, we assume we know very little about the a priori state and proscribe  $\mathbf{S}_y$  and  $\mathbf{S}_a$  such that the second term (the agreement with satellite observations) becomes dominant in determining the value of  $\Phi$ . The a priori assumptions are still helpful, however, in that the covariances assumed between vertical levels help the algorithm converge to a physically realistic solution.

#### 4.3.1 State and Observation Vectors

The state vector  $\mathbf{x}$  is made up of the column-integrated CLWP plus the RWC at each vertical level in the column at which at least one radar frequency has a reflectivity above -20 dBZ. Specifically, we retrieve  $\log_{10}(\text{CLWP})$  and  $\log_{10}(\text{RWC})$  because the OE framework assumes Gaussian distributions and these variables are closer to Gaussian when translated into logarithmic space. In the normalized gamma drop size distribution experiments (NG\_DSD, see Section 4.3.3), the state vector also contains two additional parameters, both of which are retrieved as column-averaged values. These are the mass-weighted mean rain drop diameter ( $D_m$ )

and the normalized gamma shape parameter ( $\mu$ ), as explained in Chapter 3. The size of  $\mathbf{x}$  thus depends both upon the depth of the raining column as well as the DSD model being used. The values used for the a priori state vector  $\mathbf{x}_a$  are given in Table 4.1.

Table 4.1. Values used in the a priori state vector  $\mathbf{x}_a$ , along with their assumed uncertainties included in the  $\mathbf{S}_a$  matrix.

State Variable	A priori Value	Std. Deviation $\sigma$ ( $\mathbf{S}_a$ uses $\sigma^2$ )	Comments
$\log_{10}(\text{CLWP})$	2.25 (178 g/m <sup>2</sup> )	0.25	2C-RAIN-PROFILE assumes $\log_{10}(\text{CLWP}) = 2.24 + 0.09\log_{10}(\text{RR}_{\text{surf}})$ ; we choose an apriori value that is close to their minimum and set $\sigma$ high enough that any possible 2C-RAIN-PROFILE value is within 1 std. deviation
$\log_{10}(\text{RWC})$	-1.12 (0.076 g/m <sup>3</sup> )	3.0	A priori value is equal to mean from 2C-RAIN-PROFILE; variance is set very high so that the full range of possible RWCs are within 1 $\sigma$
$\log_{10}(\text{D}_m)$	-0.3 (0.50 mm)	0.55	Only used in NG_DSD experiments
$\mu$	4.33	5.6	Only used in NG_DSD experiments

The makeup of the  $\mathbf{y}$  vector, on the other hand, depends on whether the observations being considered come from CloudSat, GPM, or both combined. For the CloudSat-only retrievals,  $\mathbf{y}$  consists of the W-band PIA plus the W-band reflectivities from CPR-base up to the highest range gate with  $Z > -20$  dBZ. For GPM-only retrievals,  $\mathbf{y}$  contains  $T_b$  from the 13 channels of GMI, Ku- and Ka- band PIA, and all valid DPR reflectivities reported in the CloudSat-GPM coincidence file for that pixel (that is, measurements that are both above the surface clutter and above DPR detection limits). For combined retrievals,  $\mathbf{y}$  includes all of these observations. We acknowledge that the GMI field of view is much larger than that of the DPR, especially for the lower frequency channels, and for this reason the forward model errors associated with the GMI observations are assumed to be quite high in the  $\mathbf{S}_y$  matrix (see Section

4.3.4 and Table 4.2). The GMI measurements weakly constrain the total amount of liquid water in the column but are much less important to the retrieval than the radar reflectivities or PIA.

#### 4.3.2 *Forward Model*

For a given state vector, we use a forward model to simulate PMW brightness temperatures, radar reflectivities, and radar two-way path integrated attenuation to compare with satellite observations from GPM and CloudSat. For simulating  $T_B$ , we use the MonoRTM radiative transfer model (Clough et al. 2005) to calculate gaseous absorption and the FASTEM6 model to estimate sea surface emissivity (Kazumori and English 2015). We assume spherical cloud and rain drops and use Mie theory (Mie 1908) to calculate the absorption and scattering from these hydrometeors. For more details on the PMW part of the forward model refer to Schulte and Kummerow (2019). For simulating Z and PIA, we use effective reflectivities calculated by the QuickBeam radar simulator (Haynes et al. 2007). Both gaseous and hydrometeor attenuation is included for calculating Z but only hydrometeor attenuation is included in the calculation of PIA, to match the way that PIA is reported in the CloudSat-GPM coincidence dataset. Because our aim is to study the impact of DSD assumptions on RR, rather than to retrieve perfect RRs, we have neglected multiple scattering in order to simplify the radiative transfer calculations. This choice is further justified by the fact that we are mostly focused on light rain. However, we note that multiple scattering can be significant at W-band radar frequencies (e.g. Battaglia et al. 2008).

The forward model requires information about the atmospheric state that is not explicitly solved for as part of  $\mathbf{x}$ . For example, profiles of temperature, pressure, and specific humidity are taken from ECMWF-AUX. The FASTEM6 model requires surface wind speed, wind direction, and sea surface temperature, which also come from ECMWF-AUX. We assume that cloud water

is uniformly distributed through the depth of the cloud, an assumption that is shared by the CloudSat 2C-RAIN-PROFILE algorithm (Lebsock 2018). We assume an inverse exponential size distribution of cloud droplets of the form

$$n(d) = n_0 e^{-\lambda d}, \quad (4.3)$$

where  $n_0$  is the intercept parameter and  $\lambda$  is the slope parameter.  $\lambda$  can be related to the effective radius  $r_e$  by

$$\lambda = \frac{3}{2r_e}. \quad (4.4)$$

We assume a constant  $r_e$  throughout the cloud of 11  $\mu\text{m}$ , a value that is broadly in line with studies such as Witte et al. (2018) and Sinclair et al. (2021) that sampled stratocumulus clouds.  $n_0$  is then calculated to give a size distribution that integrates to give the correct CLWP for a given state. This representation of cloud water is simplified, and in the absence of precipitation a more sophisticated model could be used to retrieve a profile of cloud water and droplet sizes more accurately. However, our focus in this chapter is on precipitating scenes, where radar reflectivity is dominated by the rain and/or drizzle drops and the cloud water mostly affects the attenuation and  $T_B$ . For these measurements, the total amount of cloud water in the column is much more important than the precise vertical distribution or size distribution of the cloud droplets. Sensitivity tests assuming a larger or smaller  $r_e$ , a lognormal distribution instead of an inverse exponential, or a cloud water profile that linearly increased from cloud base to cloud top did not significantly change the results of our experiments.

### 4.3.3 DSD Models

One of the most important assumptions made in the OE forward model is that of the rain DSD. We perform experiments assuming three different DSD models. The first (CS\_DSD) uses

the DSD model assumed by the CloudSat 2C-RAIN-PROFILE algorithm. For the CS\_DSD experiments, we begin with a DSD that is modeled by a gamma distribution of the form

$$N(D) = N_0 D^\mu e^{-\Lambda D}, \quad (4.5)$$

where  $N(D)$  is the number concentration of drops with diameter  $D$ ,  $N_0$  is the intercept parameter,  $\mu$  is the shape parameter, and  $\Lambda$  is the slope parameter. Following Abel and Boutle (2012), this 3-parameter formulation is reduced to a single free parameter by assuming  $\mu = 0$  and that  $N_0$  and  $\Lambda$  are related by the equation

$$N_0 = x_1 \Lambda^{x_2}, \quad (4.6)$$

with  $x_1 = 0.22$  and  $x_2 = 2.2$ . In this way any given RWC is uniquely tied to a given distribution of rain drops, and thus to a unique RR. The CS\_DSD model yields a very high concentration of small drops at low RWC, but at higher RWC  $N_0$  and  $\Lambda$  both decrease, yielding a broader distribution that is more heavily weighted towards large drops.

In another set of experiments (NG\_DSD), we use a three parameter normalized gamma model (Testud et al. 2001). The normalized gamma distribution is an alternate formulation of a gamma distribution given by

$$N(D) = N_w f(\mu) \left(\frac{D}{D_m}\right)^\mu \exp\left[-(4 + \mu)\frac{D}{D_m}\right], \quad (4.7)$$

where

$$f(\mu) = \frac{6(4+\mu)^{4+\mu}}{4^4 \Gamma(4+\mu)}. \quad (4.8)$$

This formulation retains the shape parameter  $\mu$ , but replaces  $N_0$  with  $N_w$ , the “normalized” intercept parameter, and  $\Lambda$  with  $D_m$ , the mass spectrum mean diameter. An advantage of the normalized gamma distribution is that  $D_m$  is a physical quantity that can be directly measured, while  $\Lambda$  has no meaning outside of its mathematical construct. Nonetheless, any combination of

$N_w$ ,  $D_m$ , and  $\mu$  can be expressed by a combination of  $N_0$ ,  $\Lambda$ , and  $\mu$  that yields the exact same size distribution. In the NG\_DSD experiments, we place no restrictions on  $N_w$ ,  $D_m$ , and  $\mu$ .

However, in the third set of experiments (GPM\_DSD),  $\mu$  is prescribed to be equal to 2. This mimics the assumption in the GPM\_2BCMB algorithm (Greco et al. 2016). Furthermore, in GPM\_2BCMB,  $D_m$  and  $N_w$  are retrieved in separate steps.  $D_m$  is analytically diagnosed from the Ku radar reflectivity profile, making assumptions about  $N_w$  as described in Greco et al. (2011), and then  $N_w$  is retrieved at 9 vertical locations in the raining column, assuming the profile of  $D_m$  already diagnosed. Rather than try to copy this process, in the GPM\_DSD experiments we fix  $D_m$  at each level to be equal to the value reported in the CloudSat-GPM coincidence files, leaving  $N_w$  as the only free parameter left to be retrieved.

Finally, it should be noted that the RWC of a DSD can be obtained from the following integral:

$$RWC = \frac{\pi}{6} \rho_w \int_0^\infty N(D) D^3 dD, \quad (4.9)$$

where  $\rho_w$  is the density of liquid water. This can also be expressed as

$$RWC = \pi \rho_w N_w \left( \frac{D_m}{4} \right)^4. \quad (4.10)$$

Thus, it is possible to express any given normalized gamma curve as a function of RWC,  $D_m$ , and  $\mu$ . In our testing, we found that the retrieval algorithm performed slightly better when RWC was retrieved (and  $N_w$  then calculated) than when  $N_w$  was one of the retrieved parameters. RWC also has the advantage over  $N_w$  of being a directly measurable quantity from a disdrometer.

To summarize, in the CS\_DSD experiments we retrieve a profile of RWC only while assuming  $\mu = 0$  and that Eqn. 6 is valid. In the NG\_DSD experiments, we retrieve a profile of RWC, as well as column-averaged values of  $D_m$  and  $\mu$ . And in the GPM\_DSD experiments, we

retrieve the RWC profile, prescribe  $D_m$  at each level to be equal to the  $D_m$  reported by GPM\_2BCMB, and set  $\mu = 2$ .

#### 4.3.4 Covariance Matrices

The diagonal of the  $\mathbf{S}_a$  matrix consists of the assumed variance/error in the a priori estimates of  $\log_{10}(\text{CLWP})$ ,  $\log_{10}(\text{RWC})$ , and (for NG\_DSD)  $\log_{10}(D_m)$  and  $\mu$ . Table 4.1 lists the values used. The assumed variances are designed to be especially broad so that the retrieval can capture the full range of rain rates, weighting the observations much more heavily than the a priori assumptions. Also included in the  $\mathbf{S}_a$  matrix are assumed covariances between the RWC at different vertical levels, as one would expect the amount of rain falling through one level of the atmospheric column to be correlated to the amount of rain in the adjacent levels. As noted by Haynes et al. (2009) and Lebsock and L'Ecuyer (2011), the correlation length scale should increase with RR, and thus with PIA. In a manner similar to 2C-RAIN-PROFILE, we use the following equation to define the correlation between any two levels  $i$  and  $j$ :

$$\rho_{ij} = \exp\left(\frac{-|i-j|}{1+PIA_W}\right), \quad (4.11)$$

where  $PIA_W$  is the W-band PIA measured by CloudSat for the pixel in question. For consistency, we use this correlation equation even for the GPM retrievals, although for operational retrievals without a coincident CloudSat overpass a different method would have to be used.

The uncertainties that make up the  $\mathbf{S}_y$  matrix are a combination of measurement uncertainties, which are well-known, and forward model uncertainties, which are unfortunately both larger and harder to define. To estimate these uncertainties, we first used our forward model to compute simulated observations using atmospheric profiles that combined the ECMWF-AUX information in the CloudSat-GPM coincidence profiles with the cloud and rain profiles retrieved by 2C-RAIN-PROFILE. We compared these simulated observations to the actual measurements

Table 4.2. Uncertainties assumed in the  $\mathbf{S}_y$  error covariance matrix, grouped by observation type.

Observation Type	Std. Deviation $\sigma$ ( $\mathbf{S}_y$ uses $\sigma^2$ )	Comments
GMI $T_B$	10.7/18.7/36.6 GHz h-pol: 30 K 10.7/18.7/36.6 GHz v-pol: 20 K 23.8 GHz v-pol: 15 K 89 GHz and up: 7 K	Higher frequencies have smaller footprints and thus smaller uncertainties due to footprint heterogeneity
Z	GPM Ku- and Ka-band: 4.5 dBZ CloudSat W-band: $\sigma = \sqrt{5.0 + \left[0.5 \left(1 - \frac{i-t}{t-b}\right) PIA_W\right]^2}$	CloudSat forward model uncertainty increases with increasing attenuation
PIA	2.0 dB (all frequencies)	Best estimate of forward model uncertainty

reported from CloudSat and GPM and calculated the variance in the error for each type of measurement. While this was our starting point, we also did some light tuning of the values to make the distributions of retrieved RR look more realistic. The resulting values are reported in Table 4.2. All of the diagonal values of  $\mathbf{S}_y$  are constant except for the variances corresponding to the W-band reflectivity uncertainties. Because attenuation is strong at this frequency, uncertainties grow larger the closer one is to the surface. We approximate this increase in uncertainty using the following equation:

$$\mathbf{S}_{y,ii} = 5.0 + \left[0.5 \left(1 - \frac{i-t}{t-b}\right) PIA_W\right]^2. \quad (4.12)$$

Here  $i$  is the level being considered,  $t$  is the level of the top of the raining column, and  $b$  is the level of the bottom of the raining column. Following Lebsock and L'Ecuyer (2011), the off-diagonal W-band reflectivity covariances are set to  $\mathbf{S}_{y,ij} = \min(\mathbf{S}_{y,ii}, \mathbf{S}_{y,jj})$ . This is done because forward model errors in the calculation of simulated reflectivity (including attenuation effects) are likely to be highly correlated. All other off-diagonal elements of  $\mathbf{S}_y$  (i.e., those including measurements other than W-band Z) are assumed to be zero.

The  $\mathbf{S}_a$  and  $\mathbf{S}_y$  covariance matrices are very important in the OE framework, and changes to their values can have non-trivial effects on retrieved values. In addition, determining the

proper covariances to assume is a difficult task given the many potential sources of forward model and observational uncertainties and the rather small number of CloudSat-GPM coincident observations of oceanic warm rain that we are considering. We have done our best to make error assumptions that are physically plausible, consistent with other observational algorithms (particularly 2C-RAIN-PROFILE), and that yield reasonable retrieved rain rates. Admittedly, in some cases one could make an equally justifiable but different error assumption and retrieve a different rain rate. However, our goal in this chapter is not to validate the retrieved RRs themselves but to look at differences that arise when different DSD models are assumed. We are confident that the differences we report between DSD experiments are robust, because all of the experiments make use of a consistent set of error assumptions.

## **4.4 Results**

### *4.4.1 Comparison Between Operational Products*

Our analysis of the CloudSat-GPM coincidence dataset confirms previous findings that CloudSat retrievals include a much higher frequency of occurrence of rain rates below 0.5 mm/h than GPM retrievals, and that CloudSat retrieves more accumulated oceanic warm rain than GPM. Figure 4.1 shows the frequency of occurrence of various surface rain rates for all oceanic warm rain cases in the CloudSat-GPM coincident dataset. For a pixel to be included it must meet all of the following criteria: (1) be within the DPR matched swath and over ocean; (2) have a cloud-top altitude as indicated by CloudSat that is below the altitude of the 273 K isotherm given by ECMWF-AUX; (3) have a non-zero rain rate as reported by at least one of the four satellite products considered in our analysis. These products include GPM\_2BCMB (Greco et al. 2016), GPROF (Kummerow et al. 2015), the attenuation-based CloudSat 2C-RAIN-COLUMN

algorithm (Haynes et al. 2009), and CloudSat 2C-RAIN-PROFILE (Lebsock and L'Ecuyer 2011).

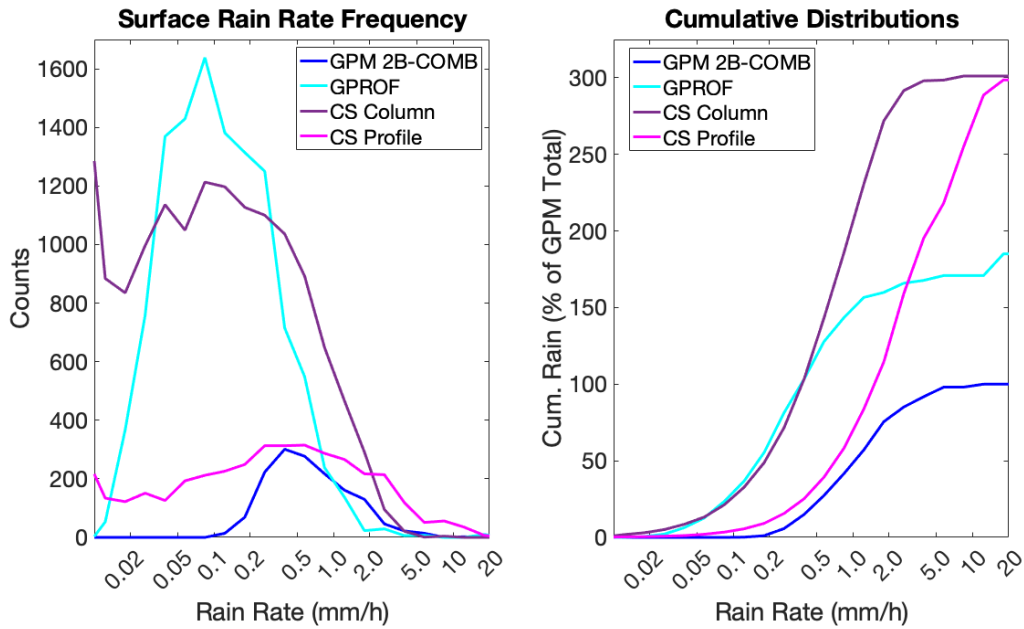


FIG. 4.1. (Left) Frequency distribution of surface rain rates from pixels seen by both GPM and CloudSat from the GPM\_2BCMB, GPROF, CloudSat 2C-RAIN-COLUMN, and CloudSat 2C-RAIN-PROFILE algorithms. (Right) Cumulative distributions of rain rates, scaled so that each curve represents that precipitation up to a given rain rate as a percentage of the total amount of rain reported by GPM\_2BCMB.

It should also be noted that precipitation frequencies depend on the spatial scale being considered. Using a coarser resolution will yield a higher frequency of precipitation overall but a lower average precipitation rate per pixel. This complicates comparisons between GPM and CloudSat as their radar footprint sizes are different. In theory, the number of consecutive CPR pixels that should be averaged together for comparison with a DPR pixel should be somewhere between 3 and 11 (Behrangi et al. 2012). The lower limit represents the number of CPR pixels it takes to completely cross a single DPR pixel. The upper limit represents the number of CPR pixels whose combined area is equal to a single DPR pixel. In Figure 4.1 and in the analysis that follows we choose to use an averaging bin of 7 CloudSat pixels when comparing to GPM

estimates, as this falls halfway between these two limits. The choice of averaging bin does not affect total accumulated precipitation.

Figure 4.1 shows that the GPM combined algorithm retrieves precipitation overall less frequently than any of the other products, and that retrieved precipitation rates from GPM of below 0.2 mm/h are very rare. GPROF includes many more pixels that have a non-zero RR, with a distribution that peaks at around 0.1 mm/h but with very few pixels above 2.0 mm/h. 2C-RAIN-COLUMN yields a similarly high concentration of RRs between 0.02 and 0.5 mm/h; however, there are more pixels with RRs between 0.5 and 5.0 mm/h which leads to much more accumulated precipitation overall. The distribution from 2C-RAIN-PROFILE includes a greater number of high RR pixels than any of the other estimates, but there are far fewer low RR pixels than seen by GPROF or 2C-RAIN-COLUMN. Many of these pixels have 2C-RAIN-COLUMN rain rates that are above zero at GPM-base, but no surface RR because the evaporation model predicts the rain will evaporate before it reaches the ground.

For the rest of this chapter we will focus on GPM\_2BCMB and 2C-RAIN-PROFILE estimates, as these are the algorithms that make the most use of the DPR and CPR radars, respectively. As can be seen on the righthand side of Figure 4.1, GPM\_2BCMB retrieves only about 33% of the total surface rain retrieved by 2C-RAIN-PROFILE. In Figure 4.2, we show how this gap is greatly reduced by accounting for surface clutter and radar sensitivity differences. The red dashed line shows the frequency of RRs from 2C-RAIN-PROFILE at GPM-base instead of the surface. This greatly reduces the number of high-RR pixels, putting the frequency much more in line with GPM\_2BCMB estimates. This implies either that GPM misses a lot of heavier, near-surface warm rain that is masked by its surface clutter, or that there is something about the CloudSat 2C-RAIN-PROFILE algorithm that causes it to overestimate RRs

in the lowest levels of the atmosphere. On the other hand, 2C-RAIN-PROFILE includes many more RRs below 0.5 mm/h at GPM-base than at the surface. This is presumably because the rain is so light that it evaporates before it reaches the surface. All told, using GPM-base estimates reduces the total accumulated warm rain from 2C-RAIN-PROFILE to about 175% of the total from GPM\_2BCMB, instead of about 300% if surface estimates are used.

Next we attempt to account for radar detection limits. Because the GPM and CloudSat observations are only near-coincident, and because whether or not a particular RR is able to be seen by DPR is dependent upon the DSD, we do this by forcing the frequency of warm rain occurrence from 2C-RAIN-PROFILE at GPM-base to be equal to the frequency of occurrence from GPM\_2BCMB. That is, since only 5.1% of GPM pixels in our dataset included measurable precipitation, we set all but the top 5.1% of RRs from 2C-RAIN-PROFILE to be equal to 0. The results are shown by the solid red line in Figure 4.2. This further reduces the discrepancy between CloudSat and GPM RRs, such that total accumulated 2C-RAIN-PROFILE warm rain is only 25% higher than GPM\_2BCMB. From the accumulation graph, it is clear that most of this difference comes at high RRs (above 2.0 mm/h), which are not frequent but that contribute significantly to total accumulation.

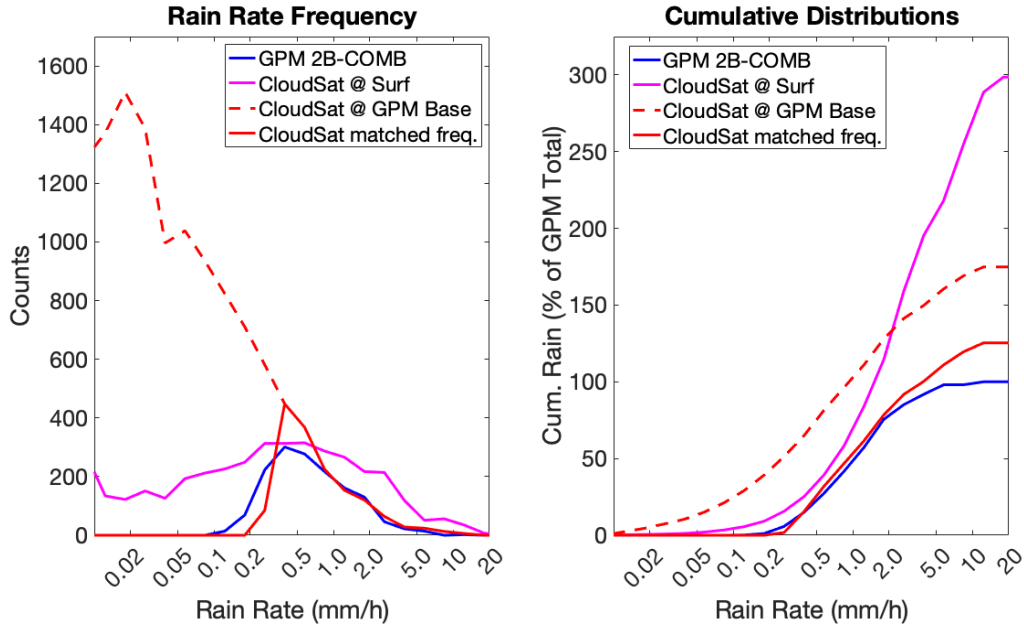


FIG. 4.2. As in Fig. 4.1, but including 2C-RAIN-PROFILE rain rates at GPM-base (dashed red) and at GPM-base with the lowest rain rates excluded such that the total rain frequency matches GPM\_2BCMB (solid red).

#### 4.4.2 CloudSat-only and GPM-only Retrievals

In our next experiment, we perform OE retrievals on either CloudSat-only or GPM-only observations, assuming DSDs models that are consistent with the 2C-RAIN-PROFILE and GPM\_2BCMB algorithms, respectively. Figure 4.3 shows scatterplots of retrieved RR compared to the operational algorithms, and Figure 4.4 shows histograms of retrieved RR frequency and the total cumulative distributions. Once again, CloudSat estimates have been averaged with a boxcar window of 7 pixels and low RRs have been eliminated to force the total rain frequency to match GPM. The retrieved rain rates do not track perfectly with the operational algorithms, which is expected given that the operational algorithms have years of development underpinning them and make assumptions in their forward models (apart from DSD assumptions) that are different than the ones made in our OE algorithm. Specifically, our retrieved rain rates are biased

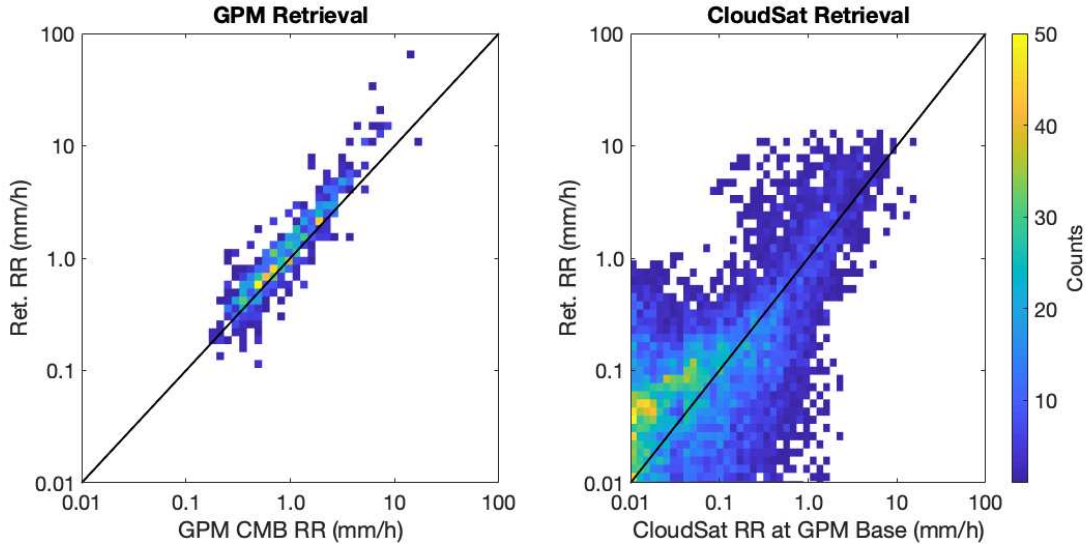


FIG. 4.3. Density plots comparing OE retrieved rain rates from GPM-only (left) or CloudSat-only observations (right) to values from the operational algorithms GPM\_2BCMB and Cloudsat 2C-RAIN-PROFILE, respectively. The GPM-only retrieval only includes cases where there exists a valid DPR reflectivity value somewhere in the column, and thus includes far fewer cases than the CloudSat-only retrieval. Both OE retrievals assume identical DSD models to the operational algorithms to which they are compared.

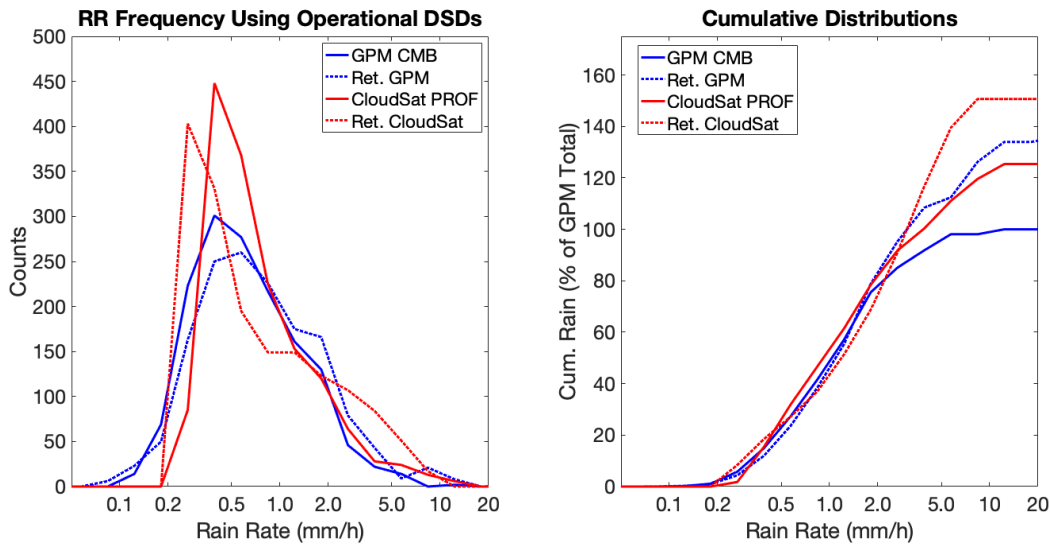


FIG. 4.4. As in Fig. 4.1, but with distributions included from GPM-only (assuming GPM\_DSD) and CloudSat-only (assuming CS\_DSD) OE retrievals, and with the CloudSat rain frequency forced to match that of GPM.

high compared to the operational algorithms. Importantly, however, we obtain a similar result to what is shown in Figures 4.1 and 4.2 in that more total rain is retrieved from CloudSat than from GPM. The gap between CloudSat and GPM estimates is about 17%, similar in magnitude to the 25% gap seen between 2C-RAIN-PROFILE and GPM\_2BCMB.

#### *4.4.3 GPM Retrievals with Adjusted DSD Assumptions*

To test the theory that gaps between CloudSat and GPM retrieved rain rates are at least partially attributable to differing DSD assumptions, we retrieve rain rates from GPM-only observations assuming the NG\_DSD and CS\_DSD models in addition to the GPM\_DSD results presented above. Results are shown in Figure 4.5. Assuming the Able and Boutle (2012) DSD of CS\_DSD shifts the entire population of retrieved rain rates higher. This results in 28% more total precipitation being retrieved in the CS\_DSD experiment compared to the GPM\_DSD experiment, a value that is quite similar to the 25% gap between 2C-RAIN-PROFILE and GPM\_2BCMB. Using NG\_DSD, the retrieved rain rates tend to be between the GPM\_DSD and CS\_DSD experiments, with total accumulation about 12% higher than in GPM\_DSD.

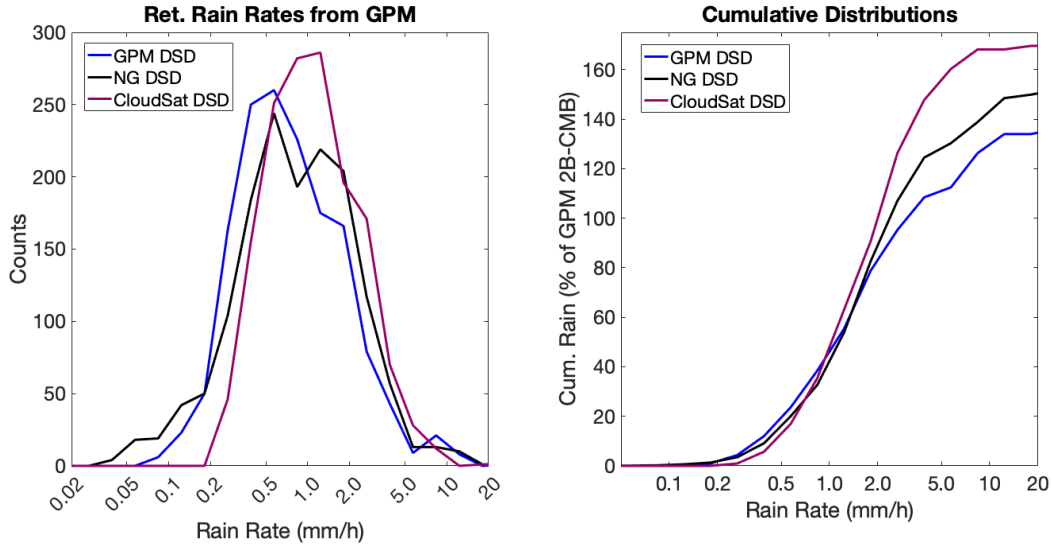


FIG. 4.5. Frequency distributions (left) and cumulative distributions (right) of GPM-only retrieved RRs assuming either the GPM\_DSD, NG\_DSD, or CS\_DSD drop size distribution models. The cumulative distributions are scaled relative to the total amount of rain accumulation from GPM\_2BCMB at GPM-base.

#### 4.4.4 Combined Retrievals

In our last set of experiments, we perform retrievals that incorporate observations from both GPM and CloudSat. This can be thought of as a proxy for what a theoretical triple-frequency spaceborne radar would retrieve, though we caution that the observations in the CloudSat-GPM coincidence dataset are not perfectly matched in space and time. Still, using both sets of observations gives a sense for how much of the CloudSat/GPM rain rate differences are due to the different sensitivities of the satellite instruments, and how much are due to DSD assumptions. We perform these combined retrievals using either the CS\_DSD or NG\_DSD assumptions (we cannot use GPM\_DSD because no  $D_m$  is reported for levels at which DPR reflectivities are below the detection thresholds).

An example of one combined retrieval is shown in Figure 4.6. This particular profile illustrates several noteworthy principles. From the radar reflectivity profiles, we see that CPR has a greater sensitivity to rain near the surface than DPR, and that CPR measures light rain that

reaches much higher than what DPR is able to see. The W-band Z also decreases below 2000 m, even as the Ku- and Ka- band Z are increasing, an indication that significant W-band attenuation is occurring. The profile of RWC from CloudSat 2C-RAIN-PROFILE is much higher than that from GPM\_2BCMB, a result that we also see in our own GPM-only and CloudSat-only retrievals. This is in large part explained by the fact that GPM\_2BCMB assumes much higher  $D_m$  values than 2C-RAIN-PROFILE. With a greater concentration of large drops assumed, less overall rain water is required in order for the simulated DPR reflectivities to reach the levels observed (note that Z scales as  $D^6$ ). In the combined NG\_DSD retrieval, which settles on a column-averaged value for  $D_m$  that is somewhat between the CloudSat and GPM results, the RWC profile similarly falls in the middle.

Rain rate distributions from the combined OE retrievals are compared against GPM-only and CloudSat-only retrievals in Figure 4.7. The combined retrievals have a greater frequency of retrieved RRs landing between 0.5 and 2.0 mm/h. In some cases where the CloudSat observations indicate light rain, GPM observations pull the solution towards higher rain rates, and vice versa. This could be for either “good” reasons (having more observables reduces the overall measurement noise) or unphysical ones (e.g. space and time mismatches). Overall, the effect of combining observations is to increase the total amount of retrieved warm rain accumulation. Another noteworthy result is that the NG\_DSD version of the combined retrieval retrieves 11% less total accumulated rain than the CS\_DSD version. This is consistent with the GPM-only results shown in Fig. 4.5 and points once again to the important role that DSD assumptions play in satellite warm rain retrievals.

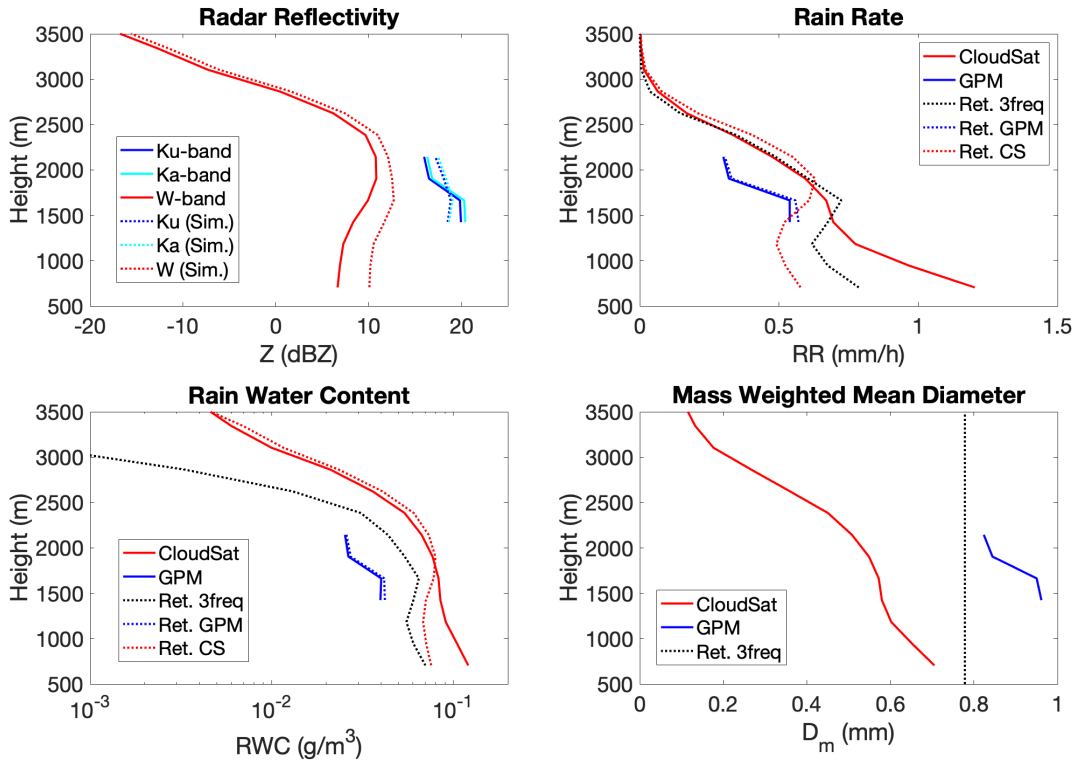


FIG. 4.6. Example of the combined (3-frequency) retrieval assuming the NG\_DSD model. *Top Left*: Profiles of observed (solid) and simulated (dotted) reflectivity at each DPR or CPR radar frequency. *Top Right*: The profile of retrieved RR is the dotted black line. For comparison, blue lines show RR profiles from GPM-only retrievals from either GPM\_2BCMB or our OE assuming GPM\_DSD, while red lines show Cloudsat-only retrievals from 2C-RAIN-COLUMN or our OE assuming CS\_DSD. *Bottom Left*: As in the previous plot, but for retrieved RWC. *Bottom Right*: Profile of  $D_m$  from 2C-RAIN-PROFILE, GPM\_2BCMB, and our combined retrieval assuming NG\_DSD. Note that our retrieval produces only a column-averaged value.

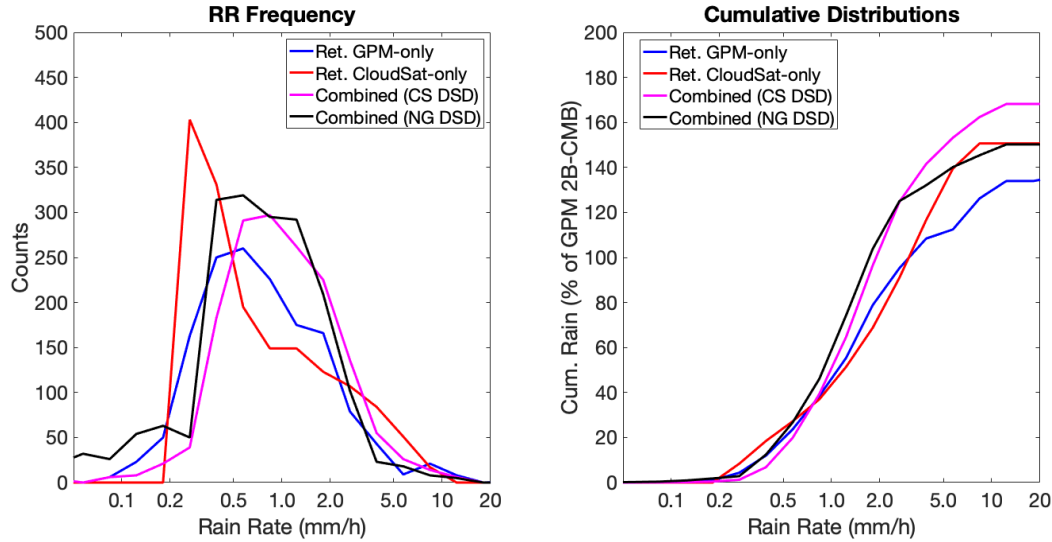


FIG. 4.7. As in Fig. 4.5, but with retrieved rain rates from GPM-only (GPM\_DSD assumed), CloudSat-only (CS\_DSD assumed), combined retrieval with CS\_DSD assumed, and combined retrieval with NG\_DSD assumed.

#### 4.5 Discussion and Conclusions

Our analysis suggests that a non-trivial portion of the difference in warm RRs retrieved by GPM and CloudSat stems from differing DSD assumptions. We can, in fact, use our results to roughly partition the GPM/CloudSat discrepancy into three categories: differences in surface clutter, differences in sensitivity, and differences in DSD assumptions. The gap between the total warm rain estimated from CloudSat 2C-RAIN-PROFILE and from GPM\_2BCMB reduces from nearly 200% of the GPM\_2BCMB total to about 75% when evaluating rain rates at 1000 m above the surface instead of using surface estimates (thus eliminating surface clutter differences). The gap is further reduced to 25% when accounting for radar sensitivity differences by forcing the rain frequencies from the two estimates to match. When using our own OE algorithm, making mostly identical algorithm assumptions but retaining differences in DSD models, total CloudSat warm rain accumulation is about 17% larger than GPM accumulation. This gap is

similar in magnitude to the 25% gap seen in the operational products, but disappears completely when we retrieve rain rates from GPM assuming the CloudSat DSD model.

The fact that the GPM\_DSD and NG\_DSD experiments resulted in lower retrieved RRs than the CS\_DSD experiments is explained by the fact that the CS\_DSD model assumes a much higher concentration of small rain drops for a given RWC. At first glance, one might think that this would result in lower RRs, since small drops fall more slowly than large drops. For a purely attenuation-based retrieval, such as 2C-RAIN-COLUMN, this would likely be the result. However, when reflectivities are considered, which (in the Rayleigh regime) scale to the power of  $D^6$ , the slower fall speed of small drops is outweighed by the fact that, if smaller drops are assumed, a much higher RWC is required in order to give the same  $Z$ . These competing effects are illustrated nicely in Figure 4.6, where the retrieved RWC at GPM-base from 2C-RAIN-COLUMN is about twice as high as the retrieved RWC from GPM\_2BCMB, but the retrieved CloudSat RR at the same level is only about 40% higher than the GPM RR.

Which DSD model is the “correct” one to assume in satellite precipitation retrievals? That is beyond the scope of this chapter, although in Chapter 2 it was found that the Abel and Boutle (2012) DSD relationship did not closely match observed DSDs from the Azores or the relationships found in other recent studies looking at disdrometer observations (Protat et al. 2019b; Liao et al. 2020). Our combined NG\_DSD retrievals tend to result in  $D_m$  values that are somewhere between the CloudSat and GPM value but that track slightly more closely to CloudSat. Still, this is somewhat dependent on the a priori value for  $D_m$  that is used in the retrieval, and we have looked only at warm rain. Results in other types of precipitation could be very different. More global observations of oceanic DSDs are needed in order to better understand how DSDs vary in different environments. Encouragingly, much progress has been

made on this front in recent years. The ORACLES (ObseRvations of Aerosols above Clouds and their intEractionS; Redemann et al. 2021) field campaign of 2016-2017 made many aircraft flights observing stratocumulus cloud structure, precipitation frequency, and precipitation intensity over the southeast Atlantic Ocean (Dzambo et al. 2019). In addition, a series of coordinated projects between 2016-2018 used in situ probes, radar, lidar, and other instruments to measure precipitation properties, including DSDs, over the Southern Ocean (McFarquhar et al. 2021). Dolan et al. (2018) identify six dominant modes of DSDs globally, using a network of ground-based disdrometer observations. Finally, the Ocean Rainfall And Ice-phase precipitation measurement Network (OceanRAIN; Klepp et al. 2018) is a recently compiled in situ ship-based ocean precipitation database that is helping to characterize the variability of global DSDs. The OceanRAIN dataset exhibits different DSD characteristics at high latitudes compared to other parts of the globe and these characteristics translate into different relationships between radar observables and RR (Protat et al. 2019a, Protat et al. 2019b, Duncan et al. 2019).

At any rate, our contention is not that either the GPM\_DSD or CS\_DSD model is definitively more appropriate but rather that they make significantly different assumptions about the shape of the rain DSD and that these differences are important for explaining retrieved RR differences. If warm rain satellite retrieval uncertainties are to be narrowed, we must not only design radars that are better able to sample light rain near the surface, but also work to better incorporate our understating of global DSD variability into retrieval algorithms.

## CHAPTER 5: CONCLUSIONS

As documented in Chapter 1, there exists significant disagreement between satellite-based retrieval algorithms in terms of the intensity and frequency of oceanic precipitation. The problem is particularly acute over the high latitudes but large discrepancies are also found in other regimes where warm rain is common. The goal of this dissertation was firstly to better understand the uncertainties affecting different types of satellite measurements, and secondly to see if retrieval differences could be resolved if a more consistent set of assumptions was made across different satellite sensors. Along the way, we also explored how future satellite precipitation missions might be constructed so as to minimize uncertainties in the retrieval of warm rain.

Critical to all 3 papers presented in this dissertation was the development of an optimal estimation retrieval algorithm that is flexible enough to be used to retrieve CLWP and DSD parameters from any combination of  $Z$ , PIA, and/or  $T_B$  measurements. With this algorithm it is possible to retrieve rain rates from GPM observations, CloudSat observations, or observations from any future satellite that makes use of radars and/or radiometers. While OE algorithms are not new to geoscience, they have more often in the past been applied to non-precipitating scenes or have used either active or passive measurements alone, rather than in combination (e.g., Boukabara et al. 2010; Duncan and Kummerow 2016). In the context of this dissertation, the algorithm allowed for better comparisons between satellites because it allowed algorithm assumptions to be ruled out as the source of discrepancies in retrieved rain rates. Even though the algorithm might not be perfectly tuned, comparisons between OE results from different satellite architectures are helpful for understanding the differences that exist in operational algorithms.

Chapter 2 focused on DSD-related retrieval uncertainties. Retrievals were run on synthetic satellite observations based on surface disdrometer observations. A 3-parameter normalized gamma model was able to adequately describe the variability seen in these real-world observations. In an idealistic scenario that featured a uniform column of rain, the relevant DSD parameters were able to be retrieved from all of the satellite architectures considered, but especially well when observations at 3 radar frequencies were available. However, assuming simpler DSD models (such as the AB12 model assumed by the CloudSat 2C-RAIN-PROFILE algorithm) led to large biases in retrieved RR. This finding led to the hypothesis that differing DSD assumptions could plausibly explain a significant portion of the disagreement in satellite precipitation estimates, a hypothesis that was tested on real data from CloudSat and GPM in Chapter 4.

Chapter 3 examined other important sources of retrieval uncertainty. High-resolution simulations from RAMS were used to study the effects of heterogeneity within the atmospheric column. Nonuniform beam filling has a large effect on retrieval accuracy, with uncorrected NUBF leading to an underestimation of RR in almost all cases. This is consistent with previous studies, but shows that the effect is significant even for non-convective cases. In the simulations, NUBF effects were larger for a GPM-like collection of measurements than a CloudSat-like collection, and also became more severe as resolution become more coarse. Increasing surface clutter also led to negative biases in retrieved RR, which were more severe for the GPM-like satellite. Taken in combination, and given GPM's reduced resolution and greater surface clutter compared to CloudSat, these results suggest roles for NUBF and surface clutter in explaining the difference in retrieved RR from the two satellites.

In Chapter 4, near-coincident observations from CloudSat and GPM were examined to show that the operational GPM\_2BCMB product misses about 43% of the total rain volume at 1000 m above the surface compared to the CloudSat 2C-RAIN-PROFILE product. The difference is even larger at the surface, and only slightly more than half of the missing rain can be attributed to rain that does not meet GPM's detection threshold. When the OE algorithm was run on either the CloudSat observations or GPM observations alone, using the DSD assumptions of each operational algorithm, a similar gap in retrieved rain rate was found. The gap became smaller when DSD assumptions were made consistent, however. GPM-retrieved RRs grew larger when the AB12 DSD scheme was assumed, while CloudSat-retrieved RRs were reduced when a normalized gamma DSD shape was assumed. The results suggest that about 25% of the total gap in accumulation between GPM and CloudSat is attributable to DSD assumption differences. The remaining gap is likely due to a combination of detection limits, NUBF, surface clutter, and non-DSD algorithm assumptions. While this dissertation falls short of definitively explaining or resolving the high latitude precipitation gap, it has diagnosed several factors that contribute.

There are many opportunities for future work that arise from the studies presented here. It would be interesting to run the CloudSat 2C-RAIN-PROFILE algorithm assuming an alternative DSD relationship. One good candidate might be the RR- $D_m$  relationship proposed by Protat et al. (2019b), since it is based on globally collected data. One might expect, given the results of this study, that doing so would reduce retrieved RRs from CloudSat. Of course, energy budget considerations (e.g., Stephens et al. 2012) suggest that the higher RRs retrieved from CloudSat are likely closer to the truth. It could be that there are compensating errors at play, with DSD assumptions inflating retrieved RRs but (for example) NUBF compensating for this bias.

The OE algorithm that has been developed also offers many avenues for exploration. While this analysis has focused on measurement types and frequencies that are already well-established, one could use the same framework to search for the combination of measurements and frequencies that would offer the most useful information for retrieving warm rain. Several useful metrics for this sort of analysis fall out of the OE methodology, including the so-called “gain matrix” or a value called the “degrees of freedom of signal”, or DFS (Rodgers 2000). There are many improvements that could be made to the algorithm forward model, including accounting for multiple scattering (Battaglia et al. 2008), the presence of frozen hydrometeors, or NUBF. In any case, the algorithm should prove a useful tool for studying the potential of future satellite missions such as the Atmosphere Observing System to reduce uncertainties in the estimation of warm rain.

## REFERENCES

- Abel, S. J., and I. A. Boutle, 2012: An improved representation of the raindrop size distribution for single-moment microphysics schemes. *Q. J. R. Meteorol. Soc.*, **138**, 2151-2162, <https://doi.org/10.1002/qj.1949>.
- Adirosi, E., E. Gorgucci, L. Baldini, and A. Tokay, 2014: Evaluation of gamma raindrop size distribution assumption through comparison of rain rates of measured and radar-equivalent gamma DSD. *J. Appl. Meteor. Climatol.*, **53**, 1618-1635, <https://doi.org/10.1175/JAMC-D-13-0150.1>.
- Adler, R. F., and Coauthors, 2003: The version-2 Global Precipitation Climatology Product (GPCP) monthly precipitation analysis (1979-present). *J. Hydrometeor.*, **4**, 1147-1167, [https://doi.org/10.1175/1525-7541\(2003\)004<1147:TVGPCP>2.0.CO;2](https://doi.org/10.1175/1525-7541(2003)004<1147:TVGPCP>2.0.CO;2).
- Adler, R. and Coauthors, 2018: The Global Precipitation Climatology Project (GPCP) monthly analysis (new version 2.3) and a review of 2017 global precipitation. *Atmosphere*, **9**, 138, <https://doi.org/10.3390/atmos9040138>.
- Albrecht, B., and Coauthors, 2019: Cloud System Evolution in the Trades (CSET): Following the evolution of boundary layer cloud systems with the NSF-NCAR GV. *Bull. Amer. Meteor. Soc.*, **100(1)**, 93-121, <https://doi.org/10.1175/BAMS-D-17-0180.1>.
- Andersson, A., C. Klepp, K. Fennig, S. Bakan, H. Grassl, and J. Schulz, 2011: Evaluation of HOAPS-3 ocean surface freshwater flux components. *J. Appl. Meteor. Climatol.*, **50**, 379-398, <https://doi.org/10.1175/2010JAMC2341.1>.
- Andrews, T., P. M. Forster, and J. M. Gregory, 2009: A surface energy perspective on climate change. *J. Clim.*, **22(10)**, 2557-2570, <https://doi.org/10.1175/2008JCLI2759.1>.
- Atlas, D., R. C. Srivastava, and R. S. Sekhon, 1973: Doppler radar characteristics of precipitation at vertical incidence. *Rev. Geophys.*, **11(1)**, 1-35, <https://doi.org/10.1029/RG011i001p00001>.
- Augstein, E., H. Riehl, F. Ostapoff, and V. Wagner, 1973: Mass and energy transports in an undisturbed Atlantic trade-wind flow. *Mon. Wea. Rev.*, **101**, 101-111, [https://doi.org/10.1175/1520-0493\(1973\)101<0101:MAETIA>2.3.CO;2](https://doi.org/10.1175/1520-0493(1973)101<0101:MAETIA>2.3.CO;2).
- Augstein, E., H. Schmidt, and F. Ostapoff, 1974: The vertical structure of the atmospheric planetary boundary layer in undisturbed trade winds over the Atlantic Ocean. *Bound. Layer Meteor.*, **6**, 129-150, <https://doi.org/10.1007/BF00232480>.

- Bartholomew, M. J., 2020: Two-dimensional video disdrometer (VDIS) instrument handbook. Ed. By Robert Stafford, ARM user facility, [https://www.arm.gov/publications/tech\\_reports/handbooks/vdis\\_handbook.pdf](https://www.arm.gov/publications/tech_reports/handbooks/vdis_handbook.pdf)
- Battaglia, A., J. M. Haynes, T. L'Ecuyer, and C. Simmer, 2008: Identifying multiple-scattering-affected profiles in CloudSat observations over the oceans. *J. Geophys. Res.*, **113**, D00A17, <https://doi.org/10.1029/2008JD009960>.
- Behrangi, A., M. Lebsock, S. Wong, and B. Lambriksen, 2012: On the quantification of oceanic rainfall using spaceborne sensors. *J. Geophys. Res. Atmos.*, **117**, D20105, <https://doi.org/10.1029/2012JD017979>.
- Behrangi, A., G. Stephens, R. F. Adler, G. J. Huffman, B. Lambriksen, and M. Lebsock, 2014: An update on the oceanic precipitation rate and its zonal distribution in light of advanced observations from space. *J. Climate*, **27**(11), 3957-3965, <https://doi.org/10.1175/JCLI-D-13-00679.1>.
- Behrangi, A., and Coauthors, 2016: Status of high-latitude precipitation estimates from observations and reanalyses. *J. Geophys. Res. Atmos.*, **121**, 4468-4486, <https://doi.org/10.1002/2015JD024546>.
- Behrangi, A., and Y. Song, 2020: A new estimate for oceanic precipitation amount and distribution using complementary precipitation observations from space and comparison with GPCP. *Environ. Res. Lett.*, **15**, 124042, <https://doi.org/10.1088/1748-9326/abc6d1>.
- Berg, W., T. L'Ecuyer, and J. M. Haynes, 2010: The distribution of rainfall over oceans from spaceborne radars. *J. Appl. Meteor. Climatol.*, **49**, 535-543, <https://doi.org/10.1175/2009JAMC2330.1>.
- Beusch, L., L. Foresti, M. Gabella, and U. Hamann, 2018: Satellite-based rainfall retrieval: From generalized linear models to artificial neural networks. *Remote Sens.*, **10**, 939, <https://doi.org/10.3390/rs10060939>.
- Bodas-Salcedo, A., K. D. Williams, M. A. Ringer, I. Beau, J. N. S. Cole, J.-L. Dufresne, T. Koshiro, B. Stevens, Z. Wang, 2014: Origins of the solar radiation biases over the Southern Ocean in CFMIP2 models. *J. Climate*, **27** (1), 41-56, <https://doi.org/10.1175/JCLI-D-13-00169.1>.
- Boukabara, S.-A., K. Garrett, and W. Chen, 2010: Global coverage of total precipitable water using a microwave variational algorithm. *IEEE Trans. Geosci. Rem. Sens.*, **48**(10), 3608-3621, <https://doi.org/10.1109/TGRS.2010.2048035>.

- Bringi, V. N., G.-J. Huang, V. Chandrasekar, and E. Gorgucci, 2002: A methodology for estimating the parameters of a gamma raindrop size distribution model from polarimetric radar data: Application to a squall-line event from the TRMM/Brazil campaign. *J. Atmospheric Ocean. Technol.*, **19**(5), 633-645, [https://doi.org/10.1175/1520-0426\(2002\)019<0633:AMFETP>2.0.CO;2](https://doi.org/10.1175/1520-0426(2002)019<0633:AMFETP>2.0.CO;2).
- Bringi, V., M. Grecu, A. Protat, M. Thurai, and C. Klepp, 2021: Measurements of rainfall rate, drop size distribution, and variability at middle and higher latitudes: Application to the combined DPR-GMI algorithm. *Remote Sens.*, **13**(12), 2412, <https://doi.org/10.3390/rs13122412>.
- Brümmer, B., E. Augstein, and H. Riehl, 1974: On the low-level wind structure in the Atlantic trade. *Quart. J. Roy. Meteor. Soc.*, **100**, 109–121, <https://doi.org/10.1002/qj.49710042310>.
- Bumke, K., G. König-Langlo, J. Kinzel, and M. Schröder, 2016: HOAPS and ERA-interim precipitation over the sea: validation against shipboard in situ measurements. *Atm. Meas. Tech.*, **9**(5), 2409–2423, <https://doi.org/10.5194/amt-9-2409-2016>.
- Burdanowitz, J., C. Klepp, and S. Bakan, 2016: An automatic precipitation-phase distinction algorithm for optical disdrometer data over the global ocean. *Atmos. Meas. Tech.*, **9**, 1637-1652, <https://doi.org/10.5194/amt-9-1637-2016>.
- Burdanowitz, J., C. Klepp, S. Bakan, and S. A. Buehler, 2018: Towards an along-track validation of HOAPS precipitation using OceanRAIN optical disdrometer data over the Atlantic Ocean. *Quart. J. Royal Meteorol. Soc.*, **144**, 235-254, <http://doi.org/10.1002/qj.3248>.
- Chen, H., V. Chandrasekar, H. Tan, R. Cifelli, 2019: Rainfall estimation from ground radar and TRMM precipitation radar using hybrid deep neural networks. *Geophys. Res. Lett.*, **46**, 10669-10678, <https://doi.org/10.1029/2019FL084771>.
- Clough, S. A., and Coauthors, 2005: Atmospheric radiative transfer modeling: A summary of the AER codes. *J. Quant. Spectrosc. Radiat. Transfer*, **91**, 233-244, <https://doi.org/10.1016/j.jqrst.2004.05.058>.
- Cotton, W. R., and Coauthors, 2003: RAMS 2001: Current status and future directions. *Meteor. Atmos. Phys.*, **82**, 5–29, <https://doi.org/10.1007/s00703-001-0584-9>.
- Dolan, B., B. Fuchs, S. A. Rutledge, E. A. Barnes, and E. J. Thompson, 2018: Primary modes of global drop size distributions. *J. Atmos. Sci.*, **75**, 1453-1476, <https://doi.org/10.1175/JAS-D-17-0242.1>.
- Duncan, D. I., and C. D. Kummerow, 2016: A 1DVAR retrieval applied to GMI: algorithm description, validation, and sensitivities. *J. Geophys. Res. Atmos.*, **121**, 7415–47429, <https://doi.org/10.1029/2016JD024808>.

- Duncan, D. I., C. D. Kummerow, and V. Petkovic, 2018: Towards variational retrieval of warm rain from passive microwave observations. *Atmos. Meas. Tech.*, **11**, 4389-4411, <https://doi.org/10.5194/amt-11-4389-2018>.
- Durden, S. L., Z. S. Haddad, A. Kitiyakara, and F. K. Li, 1998: Effects of nonuniform beam filling on rain retrieval for the TRMM precipitation radar. *J. Atmospheric Ocean. Technol.*, **15**(3), 635-646, [https://doi.org/10.1175/1520-0426\(1998\)015<0635:EONBFO>2.0.CO;2](https://doi.org/10.1175/1520-0426(1998)015<0635:EONBFO>2.0.CO;2).
- Durden, S. L., E. Im, F. K. Li, R. Girard, and K. S. Pak, 2001: Surface clutter due to antenna sidelobes for spaceborne atmospheric radar. *IEEE Trans. Geosci. Remote Sens.*, **39**, 1916-1921, <https://doi.org/10.1109/36.951082>.
- Dzambo, A. M., T. L'Ecuyer, O. O. Sy, and S. Tanelli, 2019: The observed structure and precipitation characteristics of southeast Atlantic stratocumulus from airborne radar during ORACLES 2016-17. *J. Appl. Meteor. Climatol.*, **58**, 2197-2215, <https://doi.org/10.1175/JAMC-D-19-0032.1>.
- Dzambo, A. M., and Coauthors, 2021: Joint cloud water path and rain water path retrievals from ORACLES observations. *Atmos. Chem. Phys.*, **21**, 5513-5532, <https://doi.org/10.5194/acp-21-5513-2021>.
- Elsaesser, G. S., C. W. O'Dell, M. D. Lebsock, R. Bennartz, T. J. Greenwald, and F. J. Wentz, 2017: The Multisensor Advanced Climatology of Liquid Water Path (MAC-LWP). *J. Climate*, **30**, 10193-10210, <https://doi.org/10.1175/JCLI-D-16-0902.1>.
- Giangrande, S. E., D. Wang, M. J. Bartholomew, M. P. Jensen, D. B. Mechem, J. C. Hardin, and R. Wood, 2019: Midlatitude oceanic cloud and precipitation properties as sampled by the ARM Eastern North Atlantic Observatory. *J. Geophys. Res. Atmos.*, **124**, 4741–4760, <https://doi.org/10.1029/2018JD029667>.
- Graves, C. E., 1993: A model for the beam-filling effect associated with the microwave retrieval of rain. *J. Atmospheric Ocean. Technol.*, **10**, 5-14, [https://doi.org/10.1175/1520-0426\(1993\)010<0005:AMFTBF>2.0.CO;2](https://doi.org/10.1175/1520-0426(1993)010<0005:AMFTBF>2.0.CO;2).
- Greco, M., L. Tian, W. S. Olsen, and S. Tanelli, 2011: A robust dual-frequency radar profiling algorithm. *J. Appl. Meteor. Climatol.*, **50**, 1543-1557, <https://doi.org/10.1175/2011JAMC2655.1>.
- Greco, M., W. S. Olson, S. J. Munchak, S. Ringerud, L. Liao, Z. Haddad, B. L. Kelley, and S. F. Mclaughlin, 2016: The GPM Combined Algorithm. *J. Atmospheric Ocean. Technol.*, **33**, 2225-2245, <https://doi.org/10.1175/JTECH-D-16-0019.1>.
- Greenwald, T. L., R. Bennartz, M. Lebsock, and J. Teixeira, 2018: An uncertainty data set for passive microwave satellite observations of warm cloud liquid water path. *J. Geophys. Res. Atmos.*, **123**, 3668-3687, <https://doi.org/10.1002/2017JD027638>.

- Grossklaus, M., K. Uhlig, and L. Hasse, 1998: An optical disdrometer for use in high wind speeds. *J. Atmos. Ocean. Technol.*, **15**, 1051–1059, [https://doi.org/10.1175/1520-0426\(1998\)015<1051:AODFUI>2.0.CO;2](https://doi.org/10.1175/1520-0426(1998)015<1051:AODFUI>2.0.CO;2).
- Harrington, J. Y., 1997: The effects of radiative and microphysical processes on simulated warm and transition season Arctic stratus. Ph.D. dissertation, Colorado State University, Atmospheric Science Paper 637, 289 pp. [Available online at <http://www.meteo.psu.edu/~jyh10/pubs/dis.pdf>.]
- Hayden, L., and C. Liu, 2018: A multiyear analysis of global precipitation combining CloudSat and GPM precipitation retrievals. *J. Hydrometeorol.*, **19(12)**, 1935–1952, <https://doi.org/10.1175/JHM-D-18-0053.1>
- Haynes, J. M., R. T. Marchand, Z. Lou, A. Bodas-Salcedo, and G. L. Stephens, 2007: A multipurpose radar simulation package: QuickBeam. *Bull. Amer. Meteor. Soc.*, **88(11)**, 1723–1728, <https://doi.org/10.1175/BAMS-88-11-1723>.
- Haynes, J. M., T. S. L'Ecuyer, G. L. Stephens, S. D. Miller, C. Mitrescu, N. B. Wood, and S. Tanelli, 2009: Rainfall retrieval over the ocean with spaceborne W-band radar. *J. Geophys. Res.*, **114**, D00A22, <https://doi.org/10.1029/2008JD009973>.
- Hilburn, K. A., and F. J. Wentz, 2008: Intercalibrated passive microwave rain products from the Unified Microwave Ocean Retrieval Algorithm (UMORA). *J. Appl. Meteor. Climatol.*, **47(3)**, 778–794, <https://doi.org/10.1175/2007JAMC1635.1>.
- Hou, A. Y., and Coauthors, 2014: The Global Precipitation Measurement mission. *Bull. Amer. Meteor. Soc.*, **95(5)**, 701–722, <https://doi.org/10.1175/BAMS-D-13-00164.1>.
- Hyder, P., and Coauthors, 2018: Critical Southern Ocean climate model biases traced to atmospheric model cloud errors. *Nature Communications*, **9**, 3625, <https://doi.org/10.1038/s41467-018-05634-2>.
- Igel, A., S. C. van den Heever, C. Naud, S. M. Saleeby, and D. Posselt, 2013: Sensitivity of warm frontal processes to cloud-nucleating aerosol concentrations. *J. Atmos. Sci.*, **70**, 1768–1783, <https://doi.org/10.1175/JAS-D-12-0170.1>.
- Iguchi, T., T. Kozu, J. Kwiatkowski, R. Meneghini, J. Awaka, and K. Okamoto, 2009: Uncertainties in the rain profiling algorithm for the TRMM precipitation radar. *J. Meteorol. Soc. Japan*, **87A**, 1–30, <https://doi.org/10.2151/jmsj.87A.1>.
- Illingworth, A. J., and Coauthors, 2015: The EarthCARE satellite: The next step forward in global measurements of clouds, aerosols, precipitation, and radiation. *Bull. Amer. Meteor. Soc.*, **96(8)**, 1311–1332, <https://doi.org/10.1175/BAMS-D-12-00227.1>.

- Jiang, H., and G. Feingold, 2006: Effect of aerosol on warm convective clouds: Aerosol-cloud-surface flux feedbacks in a new coupled large eddy model. *J. Geophys. Res.*, **111**, D01202, <https://doi.org/10.1029/2005JD006138>.
- Jing, X., and K. Suzuki, 2018: The impact of process-based warm rain constraints on the aerosol indirect effect. *Geophys. Res. Lett.*, **45**, 10729-10737, <https://doi.org/10.1029/2018GL079956>.
- Kalmus, P., and M. Lebsock, 2017: Correcting biased evaporation in CloudSat warm rain.. *IEEE Trans. Geosci. Remote Sens.*, **55(11)**, 6207-6217, <https://doi.org/10.1109/TGRS.2017.2722469>.
- Kay, J. E., C. Wall, V. Yettella, B. Medeiros, C. Hannay, P. Caldwell, and C. Bitz, 2016: Global climate impacts of fixing the Southern Ocean shortwave radiation bias in the Community Earth System Model (CESM). *J. Climate*, **29** (12), 4617-4636, <https://doi.org/10.1175/JCLI-D-15-0358.1>.
- Kazumori, M., and S. J. English, 2015: Use of the ocean surface wind direction signal in microwave radiance assimilation. *Quart. J. Roy. Meteor. Soc.*, **141**, 1354-1375, <https://doi.org/10.1002/qj.2445>.
- Kidd, C., and P. Joe, 2007: Importance, identification and measurement of light precipitation at mid- to high-latitudes. *Proc. Joint EUMETSAT Meteorological Satellite Conf. and 15th Satellite Meteorology and Oceanography Conf.*, Amsterdam, Netherlands, EUMETSAT and Amer. Meteor. Soc., 6 pp. [Available online at [http://www.eumetsat.int/home/Main/AboutEUMETSAT/Publications/ConferenceandWorkshopProceedings/2007/groups/cps/-documents/document/pdf\\_conf\\_p50\\_s8\\_04\\_kidd\\_p.pdf](http://www.eumetsat.int/home/Main/AboutEUMETSAT/Publications/ConferenceandWorkshopProceedings/2007/groups/cps/-documents/document/pdf_conf_p50_s8_04_kidd_p.pdf).]
- Kidd, C., A. Becker, G. J. Huffman, C. L. Muller, P. Joe, G. Skofronick-Jackson, D. B. Kirschbaum, 2017: So, how much of the Earth's surface is covered by rain gauges? *Bull. Amer. Meteor. Soc.*, **98**, 69-78, <https://doi.org/10.1175/BAMS-D-14-00283.1>.
- Kidd, C., E. Graham, T. Smyth, and M. Gill, 2021: Assessing the impact of light/shallow precipitation retrievals from satellite-based observations using surface radar and micro rain radar observations. *Remote Sens.*, **13(9)**, 1708, <https://doi.org/10.3390/rs13091708>.
- Klepp, C., K. Bumke, S. Bakan, and P. Bauer, 2010: Ground validation of oceanic snowfall detection in satellite climatologies during LOFZY. *Tellus A*, **62**, 469-480, <http://doi.org/10.1111/j.1600-0870.2010.00459.x>.
- Klepp, C., 2015: The Oceanic Shipboard Precipitation Measurement Network for Surface Validation – OceanRAIN. *Atmos. Res.*, **163**, 74-90, <http://doi.org/10.1016/j.atmosres.2014.12.014>.

- Klepp, C., and Coauthors, 2018: OceanRAIN, a new in-situ shipboard global ocean surface-reference dataset of all water cycle components. *Sci. Data*, **5**, 180122, <https://doi.org/10.1038/sdata.2018.122>.
- Koistinen, J., and E. Saltikoff, 1998: Experience of customer products of accumulated snow, sleet and rain. *COST75 Advanced Weather Radar Systems*, **397**, 406.
- Kubar, T. L., D. L. Hartmann, and R. Wood, 2009: Understanding the importance of microphysics and macrophysics for warm rain in marine low clouds. Part I: satellite observations. *J. Atmos. Sci.*, **66(10)**, 2953-2972, <https://doi.org/10.1175/2009JAS3071.1>.
- Kubota, T., T. Iguchi, M. Kojima, L. Liao, T. Masaki, H. Hanado, R. Meneghini, and R. Oki, 2016: A statistical method for reducing sidelobe clutter for the Ku- band precipitation radar on board the GPM Core Observatory. *J. Atmos. Ocean. Technol.*, **33**, 1413-1428, <https://doi.org/10.1175/JTECH-D-15-0202.1>.
- Kummerow, C. D., and Coauthors, 2000: The status of the Tropical Rainfall Measuring Mission (TRMM) after two years in orbit. *J. Appl. Meteor. Climatol.*, **39**, 1965-1982, [https://doi.org/10.1175/1520-0450\(2001\)040<1965:TSOTTR>2.0.CO;2](https://doi.org/10.1175/1520-0450(2001)040<1965:TSOTTR>2.0.CO;2).
- Kummerow, C. D., D. Randel, M. Kulie, N.-Y. Wang, R. Ferraro, S. J. Munchak, and V. Petkovic, 2015: The evolution of the Goddard profiling algorithm to a fully parametric scheme. *J. Atmos. Oceanic Technol.*, **32**, 2265-2280, <https://doi.org/10.1175/JTECH-D-15-0039.1>.
- Lebsock, M. D., and T. S. L'Ecuyer, 2011: The retrieval of warm rain from CloudSat. *J. Geophys. Res.*, **116**, D20209, <https://doi.org/10.1029/2011JD016076>.
- Lebsock, M. D., and K. Suzuki, 2016: Uncertainty characteristics of total water path retrievals in shallow cumulus derived from spaceborne radar/radiometer integral constraints. *J. Atmos. Ocean. Technol.*, **33**, 1597-1609, <https://doi.org/10.1175/JTECH-D-16-0023.1>.
- Lebsock, M. D., 2018: Level 2C RAIN-PROFILE Product Process Description and Interface Control Document, Tech. Rep. D-20308, Jet Propulsion Laboratory, California Institute of Technology, Pasadena, California, USA.
- Lee, G. W., and I. Zawadzki, 2005: Variability of drop size distributions: Time-scale dependence of the variability and its effects on rain estimation. *J. Appl. Meteor. Climatol.*, **44** (2), 241-255, <https://doi.org/10.1175/JAM2183.1>.
- Leinonen, J., M. D. Lebsock, S. Tanelli, K. Suzuki, H. Yashiro, and Y. Miyamoto, 2015: Performance assessment of a triple-frequency spaceborne cloud-precipitation radar concept using a global cloud-resolving model. *Atmos. Meas. Tech.*, **8**, 3493-3517, <https://doi.org/10.5194/amt-8-3493-2015>.

- Liao, L., R. Meneghini, and A. Tokay, 2014: Uncertainties of GPM DPR rain estimates caused by DSD parameterizations. *J. Appl. Meteor. Climatol.*, **53**, 2524-2537, <https://doi.org/10.1175/JAMC-D-14-0003.1>.
- Liao, L., R. Meneghini, T. Iguchi, and A. Tokay, 2020: Characteristics of DSD bulk parameters: Implication for radar rain retrieval. *Atmosphere*, **11(6)**, 670, <https://doi.org/10.3390/atmos11060670>.
- Lin, X., and A. Y. Hou, 2012: Estimation of rain intensity spectra over the continental United States using ground radar-gauge measurements. *J. Climate*, **25(6)**, 1901-1915, <https://doi.org/10.1175/JCLI-D-11-00151.1>.
- Mace, G. G., S. Avey, S. Cooper, M. Lebsock, S. Tanelli, and G. Dobrowalski, 2016: Retrieving co-occurring cloud and precipitation properties of warm marine boundary layer clouds with A-Train data. *J. Geophys. Res.*, **121**, 4008-4033, <https://doi.org/10.1002/2015JD023681>.
- Marchand, R., G. G. Mace, T. Ackerman, and G. Stephens, 2008: Hydrometeor detection using CloudSat – An Earth-orbiting 94-GHz cloud radar. *J. Atmos. Ocean. Technol.*, **25**, 519-533, <https://doi.org/10.1175/2007JTECHA1006.1>.
- Marshall, J., and W. M. Palmer, 1948: The distribution of raindrops with size. *J. Meteor.*, **5**, 165-166, [https://doi.org/10.1175/1520-0469\(1948\)005<0165:TDORWS>2.0.CO;2](https://doi.org/10.1175/1520-0469(1948)005<0165:TDORWS>2.0.CO;2).
- Masaki, T., T. Iguchi, K. Kanemaru, K. Furukawa, N. Yoshida, T. Kaubota, and R. Oki, 2021: Calibration of the Dual-frequency Precipitation Radar onboard the Global Precipitation Measurement Core Observatory. *IEEE Trans. Geosci. Remote Sens.*, <https://doi.org/10.1109/TGRS.2020.3039978>.
- McFarquhar, G. M., and Coauthors, 2021: Observations of clouds, aerosols, precipitation, and surface radiation over the southern ocean: An overview of CAPRICORN, MARCUS, MICRE, and SOCRATES. *Bull. Amer. Meteor. Soc.*, **102(4)**, E894-E928, <https://doi.org/10.1175/BAMS-D-20-0132.1>.
- Meneghini, R., T. Iguchi, T. Kozu, L. Liao, K. Okamoto, J. A. Jones, and J. Kwiatkowski, 2000: Use of the surface reference technique for path attenuation estimates from the TRMM precipitation radar. *J. Appl. Meteor. Climatol.*, **39**, 2053-2070, [https://doi.org/10.1175/1520-0450\(2001\)040<2053:UOTSRT>2.0.CO;2](https://doi.org/10.1175/1520-0450(2001)040<2053:UOTSRT>2.0.CO;2).
- Meyers, M. P., R. L. Walko, J. Y. Harrington, and W. R. Cotton, 1997: New RAMS cloud microphysics parameterization. Part II. The two-moment scheme. *Atmos. Res.*, **45**, 3-39, [https://doi.org/10.1016/S0169-8095\(97\)00018-5](https://doi.org/10.1016/S0169-8095(97)00018-5).
- Mie, G., 1908: Beiträge zur Optik trüber Medien, speziell kolloidaler Metallösungen. *Ann. Phys.*, **330**, 377-445, <https://doi.org/10.1002/ANDP.19083300302>.

- Miller, D. J., Z. Zhang, A. S. Ackerman, S. Platnick, B. A. Baum, 2016: The impact of cloud vertical profile on liquid water path retrieval based on the bispectral method: A theoretical study based on large-eddy simulations of shallow marine boundary layer clouds. *J. Geophys. Res. Atmos.*, **121**(8), 4122-4141, <https://doi.org/10.1002/2015JD024322>.
- Minzner, R., A., 1977: The 1976 Standard Atmosphere and its relationship to earlier standards. *Rev. Geophys.*, **15**(3), 375-384, <https://doi.org/10.1029/RG015i003p00375>.
- Mülmenstädt, J., O. Sourdeval, J. Delanoë, and J. Quaas, 2015: Frequency of occurrence of rain from liquid-, mixed-, and ice-phase clouds derived from A-Train satellite retrievals. *Geophys. Res. Lett.*, **42**(15), 6502-6509, <https://doi.org/10.1002/2015GL064604>.
- Mülmenstädt, J., and Coauthors, 2021: An underestimated negative cloud feedback from cloud lifetime changes. *Nat. Clim. Change*, 11, 508-513, <https://doi.org/10.1038/s41558-021-01038-1>.
- Nakamura, K., 1991: Biases of rain retrieval algorithms for space-borne radar caused by nonuniformity of rain. *J. Atmos. Oceanic Technol.*, **8**, 363–373, [https://doi.org/10.1175/1520-0426\(1991\)008<0363:BORRAF>2.0.CO;2](https://doi.org/10.1175/1520-0426(1991)008<0363:BORRAF>2.0.CO;2).
- National Academies of Science, Engineering, and Medicine, 2018: *Thriving on our Changing Planet: A Decadal Strategy for Earth Observation from Space*. Washington, D.C.: The National Academies Press, <https://doi.org/10.17226/24938>.
- Nelson, E. S., and T. S. L'Ecuyer, 2018: Global character of latent heat release in oceanic warm rain systems. *J. Geophys. Res. Atmos.*, **123**, 4797-4817, <https://doi.org/10.1002/2017JD027844>.
- Nuijens, L., K. Emanuel, H. Masunaga, and T. L'Ecuyer, 2017: Implications of warm rain in shallow cumulus and congestus clouds for large-scale circulations. *Surv. Geophys.* **38**, 1257-1282, <https://doi.org/10.1007/s10712-017-9429-z>.
- Ojo, J. S., D. B. Akoma, and E. O. Olurotimi, 2021: Dynamical evolution of vertical profile of rain structures observed using ground-based radar over a tropical station. *Heliyon*, 7(4), e06888, <https://doi.org/10.1016/j.heliyon.2021.e06888>.
- Porcaccia, L., P.-E. Kirstetter, V. Maggioni, and S. Tanelli, 2019: Investigating the GPM Dual-frequency Precipitation Radar signatures of low-level precipitation enhancement. *Q. J. R. Meteorol. Soc.*, **145**, 3161–3174, <https://doi.org/10.1002/qj.3611>.
- Posselt, D. J., J. Kessler, and G. G. Mace, 2017: Bayesian retrievals of vertically resolved cloud particle size distribution properties. *J. Appl. Meteor. Climatol.*, **56**, 745-765, <https://doi.org/10.1175/JAMC-D-16-0276.1>.

- Protat, A., C. Klepp, V. Louf, W. A. Petersen, S. P. Alexander, A. Barros, J. Leinonen, and G. G. Mace, 2019a: The latitudinal variability of oceanic rainfall properties and its implication for satellite retrievals: 1. Drop size distribution properties. *J. Geophys. Res. Atmos.*, **124**, 13291-13311, <https://doi.org/10.1029/2019JD031010>.
- Protat, A., C. Klepp, V. Louf, W. A. Petersen, S. P. Alexander, A. Barros, J. Leinonen, and G. G. Mace, 2019b: The latitudinal variability of oceanic rainfall properties and its implication for satellite retrievals: 2. The relationships between radar observables and drop size distribution parameters. *J. Geophys. Res. Atmos.*, **124**, 13312-13324, <https://doi.org/10.1029/2019JD031011>.
- Rapp, A. D., M. Lebsock, and T. L'Ecuyer, 2013: Low cloud precipitation climatology in the southeastern Pacific marine stratocumulus region using CloudSat. *Environ. Res. Lett.*, **8**, 014027, <https://doi.org/10.1088/1748-9326/8/1/014027>.
- Rauber, R. M., and Coauthors, 2007: Rain in shallow cumulus over the ocean: The RICO campaign. *Bull. Amer. Meteor. Soc.*, **88(12)**, 1912-1928, <https://doi.org/10.1175/BAMS-88-12-1912>.
- Redemann, J., and Coauthors, 2021: An overview of the ORACLES (ObseRvations of Aerosols above CLouds and their intEractionS) project: aerosol–cloud–radiation interactions in the southeast Atlantic basin. *Atmos. Chem. Phys.*, **21**, 1507-1563, <https://doi.org/10.5194/acp-21-1507-2021>.
- Rodell, M., and Coauthors, 2015: The observed state of the water cycle in the early twenty-first century. *J. Clim.*, **28(21)**, 8289-8318, <https://doi.org/10.1175/JCLI-D-14-00555.1>.
- Rodgers, C. D., 2000: *Inverse Methods for Atmospheric Sounding: Theory and Practice*. World Science, 240 pp.
- Saleeby, S. M., and W. R. Cotton, 2004: A large droplet mode and prognostic number concentration of cloud droplets in the Colorado State University Regional Atmospheric Modeling System (RAMS). Part I: Module descriptions and supercell test simulations. *J. Appl. Meteor.*, **43**, 182–195, [https://doi.org/10.1175/1520-0450\(2004\)043<0182:ALMAPN>2.0.CO;2](https://doi.org/10.1175/1520-0450(2004)043<0182:ALMAPN>2.0.CO;2).
- Saleeby, S. M., W. R. Cotton, D. Lowenthal, R. D. Borys, and M. A. Wetzel, 2009: Influence of cloud condensation nuclei on orographic snowfall. *J. Appl. Meteor. Climatol.*, **48**, 903–922, <https://doi.org/10.1175/2008JAMC1989.1>.
- Saleeby, S. M., and S. C. van den Heever, 2013: Developments in the CSU-RAMS aerosol model: Emissions, nucleation, regeneration, deposition, and radiation. *J. Appl. Meteor. Climatol.*, **52**, 2601–2622, <https://doi.org/10.1175/JAMC-D-12-0312.1>.

- Saleeby, S. M., S. R. Herbener, S. C. van den Heever, and T. L'Ecuyer, 2015: Impacts of cloud droplet-nucleating aerosols on shallow tropical convection. *J. Atmos. Sci.*, **72**, 1369-1385, <https://doi.org/10.1175/JAS-D-14-0153.1>.
- Sarkar, M., P. Zuidema, B. Albrecht, V. Ghate, J. Jensen, J. Mohrmann, and R. Wood, 2020: Observations pertaining to precipitation within the northeast Pacific stratocumulus-to-cumulus transition. *Mon. Wea. Rev.*, **148**, 1251–1273, <https://doi.org/10.1175/MWR-D-19-0235.1>.
- Sarkar, M., P. Zuidema, and V. Ghate, 2021: Clarifying Remotely Retrieved Precipitation of Shallow Marine Clouds from the NSF/NCAR Gulfstream V. *J. Atmos. Ocean. Technol.*, **38(9)**, 1657-1670. <https://doi.org/10.1175/JTECH-D-20-0166.1>.
- Schulte, R. M., and C. D. Kummerow, 2019: An optimal estimation retrieval algorithm for microwave humidity sounding channels with minimal scan position bias. *J. Atmospheric Ocean. Technol.*, **36**, 409-425, <https://doi.org/10.1175/JTECH-D-18-0133.1>.
- Schulte, R. M., C. D. Kummerow, W. Berg, S. C. Reising, S. T. Brown, T. C. Gaier, B. H. Lim, and S. Padmanabhan, 2020: A passive microwave retrieval algorithm with minimal view-angle bias: Application to the TEMPEST-D CubeSat Mission. *J. Atmospheric Ocean. Technol.*, **37(2)**, 197-210, <https://doi.org/10.1175/JTECH-D-19-0163.1>.
- Schulte, R. M., C. D. Kummerow, C. Klepp, and G. G. Mace, 2022: How accurately can warm rain realistically be retrieved with satellite sensors? Part 1: DSD Uncertainties. *J. Appl. Meteor. Climatol.*, under review.
- Seto, S., and T. Iguchi, 2015: Intercomparison of attenuation correction methods for the GPM dual-frequency precipitation radar. *J. Atmospheric Ocean. Technol.*, **32**, 915-926, <https://doi.org/10.1175/JTECH-D-14-00065.1>.
- Seto, S., T. Iguchi, R. Meneghini, J. Awaka, T. Kubota, T. Masaki, and N. Takahashi, 2021: The precipitation rate retrieval algorithms for the GPM Dual-frequency Precipitation Radar. *J. Meteorol. Soc. Japan. Ser. II.*, **99**, 205-237, <https://doi.org/10.2151/jmsj.2021-011>.
- Short, D. A., R. Meneghini, A. E. Emory, and M. R. Schwaller, 2015: Reduction of nonuniform beamfilling effects by multiple constraints: A simulation study. *J. Atmos. Ocean. Technol.*, **32**, 2114-2124, <https://doi.org/10.1175/JTECH-D-15-00021.1>.
- Sinclair, K., B. van Diedenhoven, B. Cairns, M. Alexandrov, A. M. Dzambo, and T. L'Ecuyer, 2021: Inference of precipitation in warm stratiform clouds using remotely sensed observations of cloud top droplet size distribution. *Geophys. Res. Lett.*, **48**, e2021GL092547, <https://doi.org/10.1029/2021GL092547>.
- Skofronick-Jackson, G., and Coauthors, 2017: The Global Precipitation Measurement (GPM) mission for science and society. *Bull. Amer. Meteor. Soc.*, **98(8)**, 1679-1695, <https://doi.org/10.1175/BAMS-D-15-00306.1>.

- Smagorinsky, J., 1963: General circulation experiments with the primitive equations. *Mon. Wea. Rev.*, **91**, 99–164, [https://doi.org/10.1175/1520-0493\(1963\)091<0099:GCEWTP>2.3.CO;2](https://doi.org/10.1175/1520-0493(1963)091<0099:GCEWTP>2.3.CO;2).
- Stavros, E. N., and Coauthors, 2021: *ESO Mission Data Processing Study – Summary of NASA Program Offices and ESO Missions Requirements, Constraints, Recommendations, and Opportunities*. Pasadena, CA: Jet Propulsion Laboratory, National Aeronautics and Space Administration, 2021.
- Stephens, G. L., and Coauthors, 2002: The CloudSat mission and the A-Train. *Bull. Amer. Meteor. Soc.*, **83(12)**, 1771-1790, <https://doi.org/10.1175/BAMS-83-12-1771>.
- Stephens, G. L., and C. D. Kummerow, 2007: The remote sensing of clouds and precipitation from space: A review. *J. Atmos. Sci.*, **64**, 3742-3765, <https://doi.org/10.1175/2006JAS2375.1>.
- Stephens, G. L., and Coauthors, 2012: An update on Earth’s energy balance in light of the latest global observations. *Nature Geoscience*, **5**, 691-696, <https://doi.org/10.1038/NGEO1580>.
- Stevens, B., and Coauthors, 2001: Simulations of trade wind cumuli under a strong inversion. *J. Atmos. Sci.*, **58**, 1870–1891, [https://doi.org/10.1175/1520-0469\(2001\)058<1870:SOTWCU>2.0.CO;2](https://doi.org/10.1175/1520-0469(2001)058<1870:SOTWCU>2.0.CO;2).
- Stubenrauch, C. J., and Coauthors, 2013: Assessment of global cloud datasets from satellites: Project and database initiated by the GEWEX radiation panel. *Bull. Amer. Meteor. Soc.*, **94(7)**, 1031-1049, <https://doi.org/10.1175/BAMS-D-12-00117.1>.
- Takahashi, N., H. Hanado, and T. Iguchi, 2006: Estimation of path-integrated attenuation and its nonuniformity from TRMM/PR range profile data. *IEEE Trans. Geosci. Remote Sens.*, **44(11)**, 3276-3283, <https://doi.org/10.1109/TGRS.2006.876295>.
- Tanelli, S., S. Durden, E. Im, K. Pak, D. G. Reinke, P. Partain, and J. M. Haynes, 2008: CloudSat’s cloud profiling radar after two years in orbit: performance, calibration, and processing. *IEEE Trans. Geosci. Remote Sens.*, **46(11)**, 3560-3573, <https://doi.org/10.1109/TGRS.2008.2002030>.
- Tang, G., D. Long, A. Behrangi, C. Wang, Y. Hong, 2018: Exploring deep neural networks to retrieve rain and snow in high latitudes using multisensory and reanalysis data. *Water Resour. Res.*, **54**, 8253-8278, <https://doi.org/10.1029/2018WR023830>.
- Testud, J., S. Oury, R. A. Black, P. Amayenc, and X. Dou, 2001: The concept of “normalized distribution to describe raindrop spectra: A tool for cloud physics and cloud remote sensing. *J. Appl. Meteor. Climatol.*, **40**, 1118-1140, [https://doi.org/10.1175/1520-0450\(2001\)040<1118:TCONDNT>2.0.CO;2](https://doi.org/10.1175/1520-0450(2001)040<1118:TCONDNT>2.0.CO;2).

- Thurai, M., and V. N. Bringi, 2018: Application of the generalized gamma model to represent the full rain drop size distribution spectra. *J. Appl. Meteor. Climatol.*, **57**, 1197-1210, <https://doi.org/10.1175/jamc-d-17-0235.1>.
- Tokay, A., and P. G. Bashor, 2010: An experimental study of small-scale variability of raindrop size distribution. *J. Appl. Meteor. Climatol.*, **49**, 2348-2365, <https://doi.org/10.1175/2010JAMC2269.1>.
- Trenberth, K. E., and J. T. Fasullo, 2010: Simulation of present-day and twenty-first-century energy budgets of the Southern Oceans. *Journal of Climate*, **23**, 440-454, <https://doi.org/10.1175/2009JCLI3152.1>.
- Turk, F. J., and Coauthors, 2021: Applications of a CloudSat-TRMM and CloudSat-GPM satellite coincidence dataset. *Remote Sens.*, **13**, 2264, <https://doi.org/10.3390/rs13122264>.
- van de Beek, C. Z., H. Leijnse, P. Hazenberg, and R. Uijlenjoet, 2016: Close-range radar rainfall estimation and error analysis. *Atmos. Meas. Tech.*, **9**, 3837-3850, <https://doi.org/10.5194/amt-9-3837-2016>.
- van den Heever, S. C., G. G. Carrio, W. R. Cotton, P. J. DeMott, and A. J. Prenni, 2006: Impacts of nucleating aerosol on Florida storms. Part I: Mesoscale simulations. *J. Atmos. Sci.*, **63**, 1752–1775, <https://doi.org/10.1175/JAS3713.1>.
- Walko, R. L., and Coauthors, 2000: Coupled atmosphere–biophysics–hydrology models for environmental modeling. *J. Appl. Meteor.*, **39**, 931–944, [https://doi.org/10.1175/1520-0450\(2000\)039<0931:CABHMF>2.0.CO;2](https://doi.org/10.1175/1520-0450(2000)039<0931:CABHMF>2.0.CO;2).
- Witte, M. K., T. Yuan, P. Y. Chuang, S. Platnick, K. G. Meyer, G. Wind, and H. H. Jonsson, 2018: MODIS retrievals of cloud effective radius in marine stratocumulus exhibit no significant bias. *Geophys. Res. Lett.*, **45**, 10656–10664, <https://doi.org/10.1029/2018GL079325>.
- Wood, R., 2005: Drizzle in stratiform boundary layer clouds. Part II: Microphysical aspects, *J. Atmos. Sci.*, **62(9)**, 3034-3050, <https://doi.org/10.1175/JAS3530.1>.
- Xie, P., and P. A. Arkin, 1997: Global precipitation: A 17-year monthly analysis based on gauge observations, satellite estimates, and numerical model outputs. *Bull. Amer. Meteor. Soc.*, **78**, 2539-2558, <https://doi.org/10.1175/JHM-392.1>.
- Xu, Z., G. G. Mace, and D. J. Posselt, 2019: A method for assessing relative skill in retrieving cloud and precipitation properties in next-generation cloud radar and radiometer orbiting observatories. *J. Atmos. Oceanic Technol.*, **36**, 2283-2306, <https://doi.org/10.1175/JTECH-D-18-0204.1>.

- Xue, H., G. Feingold, and B. Stevens, 2008: Aerosol effects on clouds, precipitation, and the organization of shallow cumulus convection. *J. Atmos. Sci.*, **65**, 392–406, <https://doi.org/10.1175/2007JAS2428.1>.
- Yang, F., E. P. Luke, P. Kollias, A. B. Kostinski, and A. M. Vogelmann, 2018: Scaling of drizzle virga depth with cloud thickness for marine stratocumulus clouds. *Geophys. Res. Lett.*, **45**, 3746–3753, <https://doi.org/10.1029/2018GL077145>.
- Zelinka, M. D., T. A. Myers, D. T. McCoy, S. Po-Chedley, P. M. Caldwell, P. Ceppi, S. A. Klein, and K. E. Taylor, 2020: Causes of higher climate sensitivity in CMIP6 models. *Geophys. Res. Lett.*, **47**, e2019GL085782, <https://doi.org/10.1029/2019GL085782>.
- Zhang, L., D. Lu, S. Duan, and J. Liu, 2004: Small-scale rain nonuniformity and its effect on evaluation of nonuniform beam-filling error for spaceborne radar rain measurement. *J. Atmos. Oceanic Technol.*, **21**, 1190–1197, [https://doi.org/10.1175/1520-0426\(2004\)021<1190:SRNAIE>2.0.CO;2](https://doi.org/10.1175/1520-0426(2004)021<1190:SRNAIE>2.0.CO;2).